Lattice models for photosynthetic membrane stacks

By

Andreana Marie Rosnik

A dissertation submitted in partial satisfaction of the

requirements for the degree of

Doctor of Philosophy

in

Chemistry

in the

Graduate Division

of the

University of California, Berkeley

Committee in charge:

Professor Phillip L. Geissler, Chair
Professor Naomi S. Ginsberg
Professor Krishna K. Niyogi

Summer 2019

Lattice models for photosynthetic membrane stacks

Abstract

Lattice models for photosynthetic membrane stacks

by

Andreana Marie Rosnik

Doctor of Philosophy in Chemistry

University of California, Berkeley

Professor Phillip L. Geissler, Chair

Proteins in photosynthetic membranes can organize into patterned arrays that span the membrane's lateral size. Attractions between proteins in different layers of a membrane stack play a key role in this ordering, as has been demonstrated by both empirical and computational methods. The architecture of thylakoid membranes, depending on physiological conditions, also may create circumstances for inter-layer interactions that instead disfavor the high protein densities of ordered arrangements. This dissertation introduces several statistical mechanical models for exploring the interplay between these opposing forces and for characterizing phases that reflect the periodic geometry of stacked thylakoid membrane discs. First, we propose a lattice model that roughly accounts for proteins' attraction within a layer and across the stromal gap, steric repulsion across the lumenal gap, and regulation of protein density by exchange with the stroma lamellae. Mean field analysis and computer simulation reveal a broken-symmetry striped phase disrupted at both high and low extremes of density. We expect that the widely varying light and stress conditions in higher plants explore the space of protein density and interaction strength broadly. The phase transitions we identify should thus lie within or near the range of naturally occurring conditions. Second, we expand upon this lattice description, allowing the thickness of each thylakoid's lumenal gap to fluctuate. This fluctuating-gap model introduces the possibility of mechanical control of photosynthetic function. We monitor how changing gap thickness affects mean protein occupation on both sides of the discs. Via mean field analysis and computer simulation we find

even richer phase behavior for this model, featuring transitions that originate in long-ranged protein interactions mediated by lumenal gap fluctuations. These results suggest that compression or expansion of lumenal gaps could lead to sudden and dramatic changes in the population and spatial patterning of photosynthetic proteins. Taken together, the lattice models we have constructed and explored provide a framework for minimalistic modeling of the physics underlying structure and function of photosynthetic membranes.

To my parents; to all my teachers throughout the years, inside and outside the classroom; to my past selves who have awaited this dissertation for so long.

Contents

Acknowledgements

Graduate school has been quite the ride. I moved to Berkeley after having been back in the United States for not even two weeks, still in culture shock from having lived a vibrant almost-year in Barcelona. I write my dissertation with much of my professional future wide open, with no definite next steps, for the first time in my twenty-seven years. The juggling of past and present, science and art, certainty and doubt, was happening then and has never stopped. Given how I started grad school, I should've seen that coming. But I suppose that's just how science – and life – operate.

My graduate school journey has been as much about science as it has been about personal growth, and consequently I would like to take this time to express gratitude for what and whom has shaped me in both aspects in these past five years.

I would be remiss to not thank my parents Andy and Philomena first, for not only bringing me into this world, but also for nurturing all of the many interests and curiosities throughout my life. While the mere usage of words like "molecular vibrations" make you shiver, you never told me I couldn't pursue science...or anything, really. Thank you for always believing in me more than I ever could believe in myself.

The person most immediately responsible for my success in grad school is my partner Josh. No human being has understood me as much as you do – and remained committed to believing in me and convincing me to believe in myself. My love, thank you for reminding me of my strengths over and over again, and for all our adventures, silly and serious.

If anyone could pull me out of an existential melancholy, it was Jeremy. Jeremy, thank you for being not just a housemate for all but the last three months of grad school, but a steadfast friend, an educator in all things film and sports, and a true believer that anything can be made into a sitcom. I couldn't have made it through the rough patches – and the fun moments –

without you by my side.

Next I recognize my godmother Barbara and my aunt Mary Jane. I have greatly enjoyed our regular conversations over the years, and I appreciate your wisdom in helping me make decisions and understand the broader context of the situations that have come my way.

To Will Polik, Brent Krueger, and Carles Curutchet: thank you for your foundational guidance in research prior to graduate school. You each gave me unique opportunities to contribute to different aspects of physical chemistry.

To my advisor, Phill Geissler: thank you for teaching me not just the mechanics but also the elegance in statistical mechanics, and advising me as I planted the seeds of my statistical mechanics story at Berkeley.

Thank you to all the non-Geissler group scientists I have worked with in some capacity, especially Drew Ringsmuth and Helmut Kirchhoff. I'm grateful for all the very interdisciplinary discussions in the SISGR community, especially those spearheaded by Dan Fletcher, Eva Schmid, and Kris Niyogi.

Many, many thanks to Leslie Dietterick and the late Lisa Littlejohn for swooping in to save the day, be it helping with paycheck paperwork or listening to rants about a bad day.

To Rebecca Wolkoff: Thank you for giving me the opportunity to try new things in a totally different sector during my internship on the optimization team at Enel X.

Here is a short list of people who made my stay at Berkeley all the better (last names included for clarity):

- Pitzer Center folks: Pratima Satish, Layne Frechette, Jaffar Hasnain, Lyran Kidon, Julia Rogers, Nathan Odendahl, Lucie Liu, Georg Menzl, Katie Klymko, Rian Kormos, Steve Cox, Paul Glenn. Thank you for putting up with each of my opinionated monologues, and for your insightful help in all things stat mech.

- Friends in the Bay: Julia Lazzari-Dean, Matt Heid, Thomas Mittiga, Marie Hepfer, Chris Mogni, Emily Hartman Guthrie, Ben Horst Guthrie, Laura Nocka, Joe Menke, Maggie Payne, Christie Dierk, Rebecca Siegelman, Chrissy Stachl, Katie Deeg. Friends outside the Bay: Emily Armbruster, Alba Soler, Félix Alfonso, Pat Komoda, Elix Colón. Thank you for enriching my life, going on adventures with me, and supporting me in science and art endeavors alike.

To the San Francisco Bay Area art community: Thank you for welcoming

a twenty-something scientist into your world with open arms. I hope that over the next however-many years I earn my keep in your company and contribute to the art scene here in a meaningful way. Thank you for creating conversation in a world that is increasingly isolating.

Lastly, I would like to do something a bit unconventional. All these folks and more have helped me immeasurably in grad school, but they are not the only ones that have helped. As an artist, I can't help but thank all the art that has resonated with me in these past five years. What follows are some of the most prominent helpers:

- Music: Vetusta Morla, The Beatles, The Killers, El Cuarteto de Nos, *Jo competeixo* (by Manel), Cat Empire, Alice Cooper, Weird Al, *Dirty computer* (by Janelle Monáe), Alicia Keys, *Physical graffiti* (by Led Zeppelin), Jeff Wayne's musical version of *War of the worlds*, Rodrigo y Gabriela. This dissertation is brought to you by Lady Gaga, The Killers, The Beatles, and Franz Ferdinand, but especially by Queen.

- Writing: short fiction by Quim Monzó, *Speaker for the dead* (Orson Scott Card), David Sedaris, *Here* (Richard McGuire), graphic novels in general, and Neil Gaiman all around, but especially in the form of the masterful postmodern epic, *The Sandman*.

- TV/film: *The Good Place*, *Steven Universe*, *Adventure time*, *Man seeking woman*, *Russian doll*, and *Blade runner* (both movies).

- Visual artists and cartoonists: Laurie Lipton, Aminder Dhaliwal, Junji Ito, Marco Mazzoni, Miles Johnston, Sana Takeda, and Raquel Córcoles (Moderna del pueblo).

- Photography: all photographs of unharmed, happy rabbits, hares, and bunnies.

Chapter 1

Introduction

This dissertation is largely comprised of two manuscripts, with each presenting a distinct class of models.

The models presented here are based on traditional lattice models widely known in the statistical mechanics community, but applied to the intricacies of photosynthetic membrane protein self-organization. The first set of models characterizes regimes for protein density ordering within a stack of membranes; its salient feature is a competition between steric repulsion and protein-protein attraction. The second set of models builds on the first, permitting variation in membrane gap distances in addition to protein density fluctuations.

This introduction will provide motivation for both works in language suitable to a slightly wider audience.

For those already overwhelmed by jargon, a breakfast-based analogy may be helpful to appreciate the kinds of organization we aim to understand at a microscopic level. The basic architecture of the photosynthetic apparatus we study is a stack of disc-shaped objects, populated by numerous smaller constituents – in essence an exotic dish of pancakes. Here, proteins (chocolate chips or blueberries) may coalesce in thylakoids (green pancakes) within chloroplasts of cells (the breakfast nook), influenced by incident light (stress of the frying pan), material input from connected structures (spoonfuls of baking soda or gobs of syrup), and other delicious factors. Whenever things become difficult to visualize, I encourage you to think of stacks of green, photosynthesizing pancakes.

Figure 1.1: This illustration of thylakoids (by me) is not perfectly scientifically accurate, but it assists the imagination.

1.1 Motivation of work

Photosynthesis is a complex process spanning multiple length and time scales. As such, most research on photosynthetic organisms tends to focus on one set of spatial or temporal scales. For example, much effort has been invested in characterizing the smallest scales of electronic energy transfer. [1, 2] On the opposite end of the spectrum, plants and other organisms have been genetically modified to change efficiencies in water use or light responses. [3] Much of this work is of an empirical nature. Theoretical work traditionally serves as a means of probing the extremes of parameter space while using purely computers and, ideally, decreased time effort. Another strength of theoretical work is its ability to explore phenotypes and behaviors difficult to produce with *in vivo* systems.

Reasons to tinker with photosynthetic systems are myriad, from design of artificial photosynthesis mechanisms [4, 5] to modifying crops for a changing climate. [3] Photoautotrophs have developed the means to harness solar energy over billions of years, and these processes are incredibly sensitive to

external and internal conditions of the organism. Photosynthesis research attempts to demystify the many levels of photosynthesis across an array of photoautotrophs.

With the scope of ideologies introduced, we will consider the more immediate context in which this dissertation resides. The vast majority of photosynthetic activity occurs in the chloroplast, and as such we focus our attention to chloroplasts and their analogues. (For those seeking visual representations of the innards of chloroplasts, Refs. [6, 7] are quite helpful.) We further center ourselves on the infrastructure involved in light-harvesting and electron transport – the thylakoid membranes. Previous theoretical studies of photosynthesis have focused on lateral self-organization within thylakoid membranes, [8, 9, 10] electronic energy transfer in thylakoid membranes, [11] and optical properties of thylakoid membrane collections. [12] Most of these studies focus on interactions among proteins *in the plane* of a thylakoid membrane layer, with the exception of Ref. [12].

However, thylakoid membranes can exist in stacks, [6, 13] creating opportunities for ordering *out of the plane* of thylakoid membranes. This dissertation is an exploration of regimes for vertical ordering in thylakoid membrane stacks (grana; singular, granum), primarily in higher plants. We specify higher plants, as these are the organisms with the greatest propensity to develop grana.

1.2 Brief note on techniques

This dissertation utilizes methodologies common to the discipline of statistical mechanics, namely Monte Carlo simulations and mean field theory. The specifics of these techniques needed to understand the results presented here are detailed in the chapters devoted to the two manuscripts, as well as the appendices.

1.3 Soft constraint model

The first manuscript relates my exploration of what I will call the *soft constraint model*, or the *fixed-gap model*, a lattice model whose main feature is the competition between attractive and repulsive forces in the vertical direction of a granum. In Chapter 2, I develop the method from physical and

mathematical perspectives, then describe the possible phases of order and disorder that arise from it. Helpful explanatory cartoons are displayed, and these remain relevant for the second model. I outline the mean field calculations and Monte Carlo simulations. The resulting phase diagrams and their implications are discussed at length.

1.4 Fluctuating-gap model

The second manuscript, described in Chapter 3, follows the development of the second class of models, the *fluctuating-gap model*. Here another set of fluctuating quantities is added: in addition to variations in protein density, this model accounts for fluctuations in thylakoid disc thickness (or lumenal gap thickness). This extension enriches the phase space significantly. In Chapter 3, I explain the difference between this model and the soft constraint model, including new, additional means of describing order and disorder. Then I proceed to outline a mean field approach and the resulting phase diagrams, as well as sketch simulation data.

Chapter 2

Lattice models for protein organization throughout thylakoid membrane stacks

2.1 Preface

The text of this chapter is the manuscript, *Lattice models for protein organization throughout thylakoid membrane stacks*, submitted in early July 2019, whose preprint is Ref. [14]. For the sake of completion I include the Abstract and Statement of Significance here. The Supplemental Information is given in Appendix 5.1.

2.2 Abstract

Proteins in photosynthetic membranes can organize into patterned arrays that span the membrane's lateral size. Attractions between proteins in different layers of a membrane stack can play a key role in this ordering, as was suggested by microscopy and fluorescence spectroscopy and demonstrated by computer simulations of a coarse-grained model. The architecture of thylakoid membranes, however, also provides opportunities for inter-layer interactions that instead disfavor the high protein densities of ordered arrangements. Here we explore the interplay between these opposing driving forces, and in particular the phase transitions that emerge in the periodic geometry of stacked thylakoid membrane discs. We propose a lattice model

that roughly accounts for proteins' attraction within a layer and across the stromal gap, steric repulsion across the lumenal gap, and regulation of protein density by exchange with the stroma lamellae. Mean field analysis and computer simulation reveal rich phase behavior for this simple model, featuring a broken-symmetry striped phase that is disrupted at both high and low extremes of chemical potential. The resulting sensitivity of microscopic protein arrangement to the thylakoid's mesoscale vertical structure raises intriguing possibilities for regulation of photosynthetic function.

2.3 Statement of significance

This work develops the first theoretical model for grana-spanning spatial organization of photosynthetic membrane proteins. Based on the stacked-disc structure of thylakoids in chloroplasts, it focuses on a competition between interactions that dominate in different parts of the granum. Analysis and computer simulations of the model reveal striped patterns of high protein density as a basic consequence of this competition, patterns that acquire long-range order for a broad range of physical conditions. Because natural changes in light and stress conditions can substantially alter the strengths of these competing interactions, we expect that an ordered phase with periodically modulated protein density is thermodynamically stable at or near some physiological conditions.

2.4 Introduction

Photosynthetic membranes are dense in proteins that cooperate to execute the complicated chemistry fundamental to light-harvesting and other components of photosynthesis. Membrane functionality depends not only on these proteins, but also supramolecular spatial arrangements thereof. Both the architecture of the membranes and the interactions of the protein components influence protein organization. Both levels of complexity are further influenced by light and physiological conditions.

In higher plants, photosynthetic membranes are arranged as stacks (called grana) of discs (called thylakoids). Each thylakoid, measuring roughly 300-600 nm in diameter and 10-15 nm thick, is bounded above and below by a lipid bilayer densely populated with photosynthetic proteins (See Fig. 2.1).

[6, 15, 7] A typical granum is composed of 10-100 thylakoid discs, spaced vertically by 2-4 nm. Grana do not exist in isolation in chloroplasts; rather, they are connected by unstacked membranes called stroma lamellae, which tend to be longer and have different protein composition. See Refs. [6, 7] for visual representations of the membrane architecture.

This intricate geometry provides diverse opportunities for association among transmembrane proteins. We focus on interactions and arrangements involving two particular proteins, photosystem II (PSII) and light-harvesting complex II (LHCII), which abound in the central, mostly flat portion of thylakoid discs. [6, 16, 17, 18] "Super-complexes" comprising a handful of these proteins can form with a variety of ratios PSII:LHCII. [6, 19] Super-complexes are situated within a single lipid bilayer, but their stability may be influenced by interactions across the gap separating distinct thylakoid discs. [8, 20, 21] These interactions are net attractive due to solvent mediation of interactions between polar, protruding domains of LHCII proteins. Such attractive "stacking" interactions may also drive larger scale organization of these proteins within the plane of the bilayer, forming laterally into extended periodic arrays that have been observed. [20, 22, 23, 24, 25] Computational work has suggested that these lateral arrays signal a phase transition to a crystalline state that would exhibit truly long-range two-dimensional order in the absence of constraints on protein population and disc size. [8, 9, 10, 11] Small changes in protein composition, density, and interaction strength could thus trigger sudden large-scale reorganization. Diminished stacking during state transitions and non-photochemical quenching processes, processes of thylakoid restructuring to shift electronic excitations or to minimize photo-oxidative damage, respectively, may reflect control mechanisms that exploit this sensitivity. [26]

Vertical interactions in a stack of thylakoids can also be repulsive in character. Due to narrow spacing between apposed membranes, and the significant protrusion of certain proteins into the region between stacked membranes, steric repulsion is likely to influence spatial organization in some circumstances. PSII in particular extends large domains towards the interior of thylakoid discs (called the lumen), a space that contracts under low light conditions. With sufficient contraction of the lumen, PSII molecules inhabiting a disc's opposing membranes would be unable to share the same lateral position. [20, 27, 28, 29] The consequences of such a constraint on protein organization, *e.g.*, its implications for the stability of stacked protein arrays, have not been directly explored in either experiment or simulation. However,

the implications of these spatial constraints on the diffusion of molecules in the lumen has been addressed in Refs. [27, 28].

Our work addresses the interplay between attractive and repulsive protein-protein forces within grana stacks. To date only one study has attempted to quantify the competition between attractive and repulsive protein-protein forces within grana stacks, including how this competition is affected by changing physiological conditions. [30] Different interactions likely prevail in different parts of the stack, due to proteins' well-defined orientation relative to the lumen. We therefore focus on the possibility of spatially modulated order, patterns of protein density that alternate along the direction of stacking. To date such patterns have not been observed in experiment, but potential impacts of related kinds of granum-scale order on photosynthetic function have recently been discussed. [12]

There is empirical evidence for vertically extended order within a stack of membranes, though in a much simpler context. Specifically, synthetic membrane systems, devoid of proteins, have been constructed to examine compositional ordering in an array of phospholipid bilayers with multiple lipid constituents. [31, 32] Spatial modulations in lipid composition were observed to align and extend throughout the entire membrane stack, establishing a basic plausibility for the ordered phases discussed in this work.

In order to examine the basic physical requirements for protein correlations spanning an entire stack of thylakoids, we develop minimal models that account for locally fluctuating protein populations in a granum-like geometry. As described in Sec. 2.5, these fluctuations are biased by protein-dependent attractions between discs, and by steric repulsion between proteins that reside in the same disc. The strengths of these interactions are determined by parameters that roughly represent light conditions and protein phosphorylation states. Using methods of Monte Carlo simulation detailed in Sec. 2.6, as well as mean field theories presented in Sec. 2.7, we find that strongly cooperative behavior emerges over a wide range of conditions. As parameter values are changed, the model system can cross phase boundaries where intrinsic symmetries are spontaneously broken or restored. The correspondingly sudden changes in the microscopic arrangement of photosynthetic proteins suggest a mechanism for switching sharply between distinct states of light harvesting activity, as discussed in Sec. 2.8. In Sec. 2.9 we conclude.

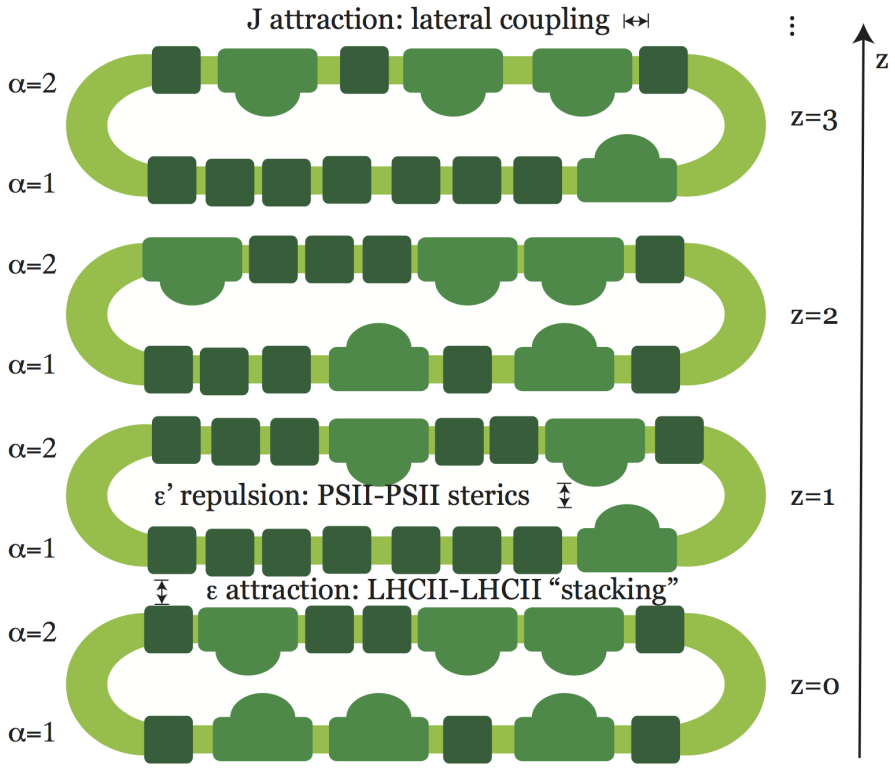

Figure 2.1: Schematic cross-section of a short stack of thylakoids discs. Dark green squares represent LHCII molecules, lighter green domed shapes represent PSII, and yellow-green bands represent lipid bilayers. Each disc (indexed by an integer z) comprises two layers (indexed $\alpha = 1$ and $\alpha = 2$). Protein attraction within each layer is assigned an energy scale J in our lattice model. Aligned LHCIIs in subsequent layers can engage in favorable stacking interactions, which is assigned an energy ϵ in the model. Protrusion of PSII into the lumen spaces (*i.e.*, the interior of each disc) may lead to steric repulsion between the two layers of each disc. Mediated by thylakoid gap and membrane fluctuations, the effective steric energy scale is denoted ϵ'.

2.5 Model

2.5.1 Physical description

Our model of stacked thylakoid discs elaborates the familiar lattice gas model of liquid-vapor phase transitions. We represent the microscopic arrangement of proteins on a cubic lattice, resolving their transiently high number density in some parts of the membrane and low density in others. Proteins' specific identities and internal structures are not resolved here; in discretizing space at the scale of a protein diameter, we have notionally averaged out such details. Our fluctuating degrees of freedom are thus binary variables n for each lattice site, indicating the local scarcity ($n = 0$) or abundance ($n = 1$) of protein. We refer to the local states $n = 0$ and $n = 1$ as unoccupied and occupied, respectively, although they do not strictly indicate the presence of an individual molecule.

The net protein density in our model membranes may fluctuate according to a chemical potential μ. Such variations generally represent exchange of material with a reservoir. In our case the stroma lamellae – unstacked regions of photosynthetic membrane – could play the role of reservoir. Alternatively, μ could be regarded as a tool of mathematical convenience (a Lagrange multiplier) for manipulating the total density in calculations.

Interaction energies are assigned wherever adjacent sites on the lattice are occupied. The sign and strength of such an interaction depends on the locations of the two lattice sites involved, as depicted in Fig. 2.1. Within a planar layer of the stack (a disc comprises two layers), neighboring occupied sites contribute an attractive energy $-J$, representing lateral forces of protein association. Stacking interactions occur between laterally aligned sites on the facing layers of sequential discs in the granum; each pair of occupied stacked sites contributes an attractive energy $-\epsilon$.

Laterally aligned sites within the same disc are subject to a repulsive energy ϵ', representing steric forces between transmembrane proteins protruding into the lumen. The harshly repulsive nature of steric interactions suggests that ϵ' should be very large, effectively enforcing a constraint of volume exclusion. For this reason, we will consider $\epsilon' = \infty$ as a special case. Termed the *hard constraint limit*, this case offers mathematical simplification as well as transparent connections to a related class of spin models. Smaller values of ϵ', however, may be more appropriate in situations where steric overlap can be avoided through modest deformation of the membrane layers. Un-

der high light conditions, when thylakoid discs swell in the vertical direction, very slight membrane deformation (or perhaps none at all) could be sufficient to allow simultaneous occupation of laterally aligned sites, corresponding to very small ϵ'.

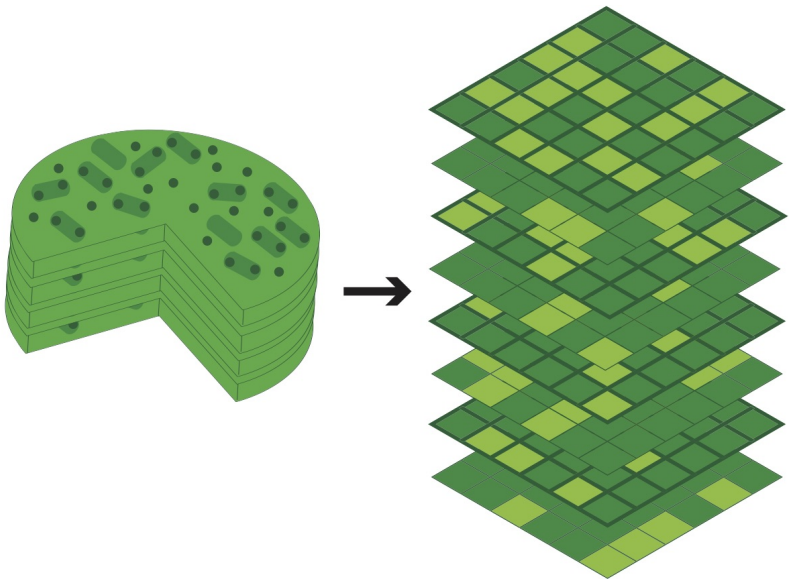

Figure 2.2: Depictions of a granum state with high protein density. In the left illustration, yellow-green indicates membrane that is not inhabited by protein; small dark circles are LHCII trimers; and oblong green shapes with small circles are PSII-LHCII supercomplexes. The right illustration shows a lattice representation of a similarly dense microstate. Here, yellow-green indicates a local sparsity of proteins, and dark green represents a region that is densely populated by either protein. These colors and shapes are used consistently throughout the chapter.

The ground state of this model depends on values of the energetic parameters μ, ϵ, J, and ϵ'. Large, positive μ encourages occupation and thus favors a high average value $\bar{n}$ of the local occupation variable. In the limit $\mu \to +\infty$, a state of complete occupation is thus energetically minimum. At high μ we generally expect thermodynamic states that are densely populated, as depicted in Fig. 2.2. Conversely, at very negative values of μ we expect very sparse equilibrium states, as depicted in Fig. 2.3.

Equilibrium states at modest μ are characterized by competition among

steric repulsion and the favorable energies of stacking and in-plane association. Large ϵ' harshly penalizes lattice states that are more than half full – states which must feature simultaneous occupation of laterally aligned sites within the same disc. In order to realize in-plane attraction at half filling, one layer of each thylakoid must be depleted of protein. The stack then comprises a series of sparse and dense layers. Extensive stacking interaction between discs requires a coherent sequence of these layers, yielding ground states that are striped with a period of four layers. This pattern is illustrated in Fig. 2.4 and quantified by an order parameter Δn that compares protein density in the two layers of each thylakoid. More specifically, Δn is a linear combination of layer densities, whose coefficients change sign with the same periodicity as the stripe pattern described. Macroscopically ordered stripes of protein density may be an unlikely extreme in real grana. Slow ordering kinetics, imperfect grana architecture, or insufficiently strong interactions could all prevent long-range coherence in practice. The tendency towards ordering for dark to low light conditions can still be of importance, *e.g.*, in the form of transient striping over substantial length scales or a steep decline in the population of vertically adjacent PSIIs as the transition is approached.

The two layers of each disc are completely equivalent in our model energy function. Stripe patterns, which populate the two layers differently with a persistent periodicity, do not possess this symmetry. Equilibrium states with $\Delta n \neq 0$ therefore require a spontaneous symmetry breaking and a macroscopic correlation length, and they must be separated from symmetric states by a phase boundary. The computational and theoretical work reported in the following sections aims to determine what, if any, thermodynamic conditions allow for such symmetry-broken, coherently striped states at equilibrium. Possible physiological consequences of this organization will be discussed in Sec. 2.8.

2.5.2 Mathematical definition

In order to describe quantitatively the energetics and ordering we have described, it is useful to index lattice sites according to (a) the thylakoid disc to which they belong, specified by a vertical coordinate z ranging from 1 to L_z, (b) which layer of the disc they inhabit, $\alpha = 1$ (bottom) or $\alpha = 2$ (top), and (c) the lateral position, specified by an integer i ranging from 1 to $L_x L_y$.

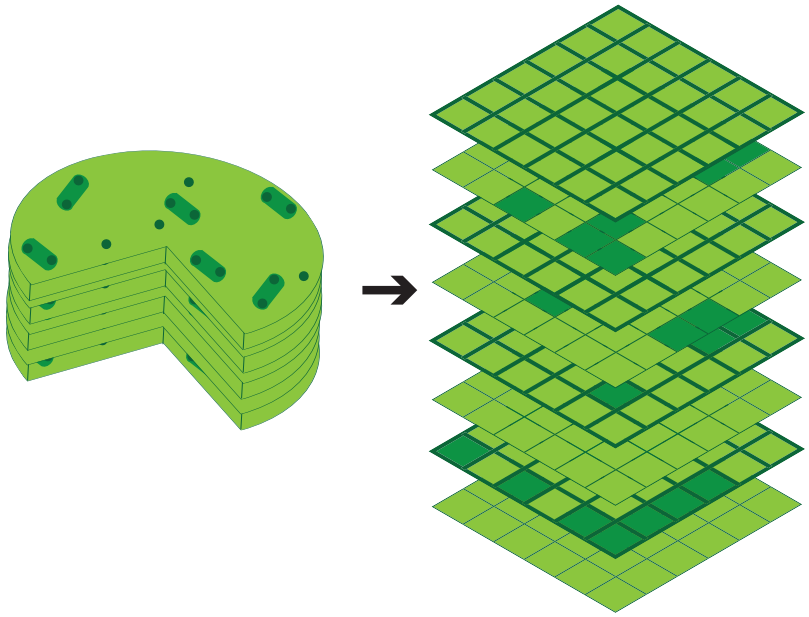

Figure 2.3: Depictions of a granum state with low protein density. Colors and shapes have the same meaning as in Fig. 2.2.

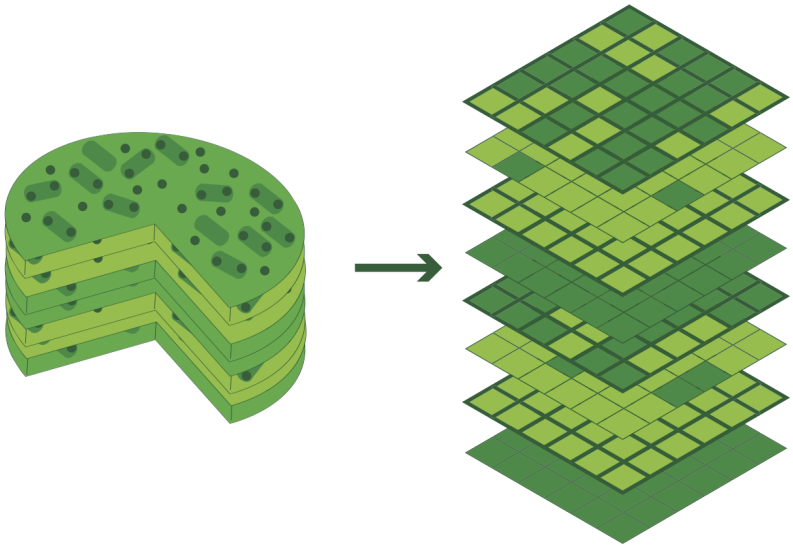

Figure 2.4: Depictions of a granum state with striped order. Layers of high and low protein density alternate vertically with a period of two discs. Specifically, each disc includes one high-density layer and one low-density layer; and each high-density layer is vertically adjacent to a dense layer on an adjacent disc. Colors and shapes have the same meaning as in Fig. 2.2.

(See Fig. 2.1). Density and striping order parameters are then defined as

$$\bar{n} \equiv (2L_xL_yL_z)^{-1} \sum_{z,i,\alpha} n_{\alpha,i}^{(z)} \tag{2.1}$$

and

$$\Delta n \equiv (2L_xL_yL_z)^{-1} \sum_{z,i} (-1)^z (n_{1,i}^{(z)} - n_{2,i}^{(z)}), \tag{2.2}$$

and the total energy of a configuration $\{n_{\alpha,i}^{(z)}\}$ is written

$$\begin{aligned} H[\{n_{\alpha,i}^{(z)}\}] \quad &= -\mu \sum_{z,\alpha} \sum_{i} n_{\alpha,i}^{(z)} - J \sum_{z,\alpha} \sum_{i,j}{}' n_{\alpha,i}^{(z)} n_{\alpha,j}^{(z)} \\ &\quad -\epsilon \sum_{z} \sum_{i} n_{2,i}^{(z)} n_{1,i}^{(z+1)} + \epsilon' \sum_{z} \sum_{i} n_{1,i}^{(z)} n_{2,i}^{(z)}, \end{aligned} \tag{2.3}$$

where the primed summation extends over distinct pairs of lateral nearest neighbors. As described above, each occupation variable $n_{\alpha,i}^{(z)}$ adopts values 1 (occupied) or 0 (unoccupied). The energetic parameters ϵ (in-plane attraction), J (stacking attraction), and ϵ' (steric repulsion) are all positive constants. At temperature T, the equilibrium probability distribution of $\{n_{\alpha,i}^{(z)}\}$ is proportional to the Boltzmann weight $e^{-\beta H}$, where $\beta \equiv 1/k_BT$.

In addition to transparent spatial symmetries, this model possesses a symmetry with respect to inverting occupation variables. Applying the transformation $\hat{n}_{\alpha,i}^{(z)} = 1 - n_{\alpha,i}^{(z)}$ to all lattice sites generates from any configuration $\{n_{\alpha,i}^{(z)}\}$ a dual configuration $\{\hat{n}_{\alpha,i}^{(z)}\}$ whose probability is also generally different from the original. As in the lattice gas, a certain choice of parameters renders the Boltzmann weight invariant under this transformation. In our case this statistical invariance occurs when $-2\mu - 4J - \epsilon + \epsilon' = 0$, establishing a line of symmetry in parameter space. More usefully for our purposes, the duality establishes pairs of equilibrium states with related thermodynamic properties. Specifically, the states $(\mu, \epsilon, J, \epsilon', T)$ and $(\hat{\mu}, \epsilon, J, \epsilon', T)$ have identical statistics of Δn for the choice

$$\hat{\mu} = -\mu - 4J - \epsilon + \epsilon' \tag{2.4}$$

Viewing density rather than chemical potential as a control parameter, distributions of Δn are identical in pairs of thermodynamic states $(\bar{n}, \epsilon, J, \epsilon', T)$ and $(\hat{\bar{n}}, \epsilon, J, \epsilon', T)$ related by $\hat{\bar{n}} = 1 - \bar{n}$; in other words, $\bar{n} = 1/2$ is also a line of symmetry due to duality.

For the phase transitions of interest here, these arguments guarantee that any phase boundary at chemical potential μ (or density $\bar{n}$) is mirrored by a dual transition at $\hat{\mu}$ (or $\hat{\bar{n}}$), for any consistent choice of ϵ, J, ϵ', and T. More physically, any phase change induced by controlling protein density must exhibit reentrance (or else occur exactly at the line of symmetry, which we do not observe).

In simpler terms, imagine an initial equilibrium state with very low protein density and negligible spatial correlation. Increasing protein occupancy towards half filling could (and often does) drive the model system into a striped state with long range order. The inversion symmetry we have described dictates that a further increase in density must eventually destroy striped order. The latter transition may be more easily envisioned as a consequence of loading thylakoid discs beyond half filling – once steric energies have been overcome, the competition underlying striped order becomes imbalanced, and an unmodulated state of high density is thermodynamically optimal. Mathematically, the loss of modulated order at high protein density is simply the dual transition of its appearance.

Like the lattice gas, our thylakoid stack model can be mapped exactly onto a spin model with binary variables $\sigma = 2n - 1 = \pm 1$. Among the expansive set of spin models that have been explored numerically and/or analytically, we are not aware of one that maps precisely onto this variant of the lattice gas. Many, however, share similar ordering motifs and spin coupling patterns. [33, 34, 35] Alternating attraction and repulsion in Eq. (2.3) correspond to mixed ferromagnetic and antiferromagnetic couplings in a spin model, *e.g.*, in axial next-nearest neighbor Ising (ANNNI) models, which can also support modulated order. [36] A different class of spin models seems better suited to the hard constraint limit of Eq. (2.3). For $\epsilon' = \infty$ each lateral position on a thylakoid disc can adopt three possible states (both layers empty, and one or the other layer filled), two of which are statistically equivalent. The similarity to a three-state Potts model in an external field is more than superficial. Much of the phase behavior we identify echoes what is known for that model in three dimensions, [37] even for finite steric repulsion strengths (ϵ').

The spirit of our approach echoes many previous efforts to understand basic physical mechanisms of collective behavior in membrane systems, from lipid domain formation to correlations among sites pinned by proteins or substrates. [38, 39, 40, 41, 42, 43, 44, 45, 46, 47, 48] By stripping away most molecular details, simplified descriptions of phase transitions, such as

spin models and field theories, focus attention on the emergence of dramatic macroscopic response from a few microscopic ingredients. They also greatly reduce the computational cost of sampling pertinent fluctuations, which are simply inaccessible for biomolecular systems near phase boundaries when considered in full atomistic detail. This perspective has even been applied to stacks of membrane layers, but not in a photosynthetic context. [31, 32, 49, 50]

Here we examine equilibrium structure fluctuations of the lattice model defined by Eq. (2.3), using both computer simulations and approximate analytical theory. We first describe results of Monte Carlo sampling, which confirm the stability of a striped phase over a broad range of temperature and density. We then present mean field analysis that sheds light on the nature of symmetry breaking and relationships with previously studied models.

2.6 Methods: Monte Carlo simulations

We used standard Monte Carlo methods to explore the phase behavior of our thylakoid lattice model. Specifically, we sampled the grand canonical probability distribution $e^{-\beta H}$ for a periodically replicated system with $L_x = L_y = 10$ and $L_z = 24$, over broad ranges of temperature and chemical potential. This geometry can accommodate $L_z/2 = 12$ copies of the striped motif in the central simulation cell.

Within mean field approximations presented in the next section, the attractive energy scales J and ϵ are most important in the combination $4J + \epsilon$. We therefore define a parameter

$$K \equiv (4J + \epsilon)/k_B T \tag{2.5}$$

and focus on $\beta\mu$, K, and ϵ' as essential control variables for this model. The ratio J/ϵ can also be varied; but for values of J/ϵ that are not extreme, this ratio is not expected to affect qualitative behavior. For simplicity, we limit attention to results exclusively for values of J/ϵ very close to $1/4$, for which we have systematically varied $\beta\mu$, K, and ϵ'. A limited set of simulations with $J/\epsilon = 0.5$ and 1 support the ratio J/ϵ as inessential within the range studied.

These simulations confirm the symmetry-breaking scenario described above, in which the average value $\langle \Delta n \rangle$ of the striping order parameter can become

nonzero in an intermediate range of $\beta\mu$. In other words, a phase with macroscopically coherent stripes can be thermodynamically stable at intermediate density. We identify and characterize transitions between this striped phase and the "disordered" phase with $\langle \Delta n \rangle = 0$ by computing probability distributions $P(\Delta n)$. Fig. 2.5 shows corresponding free energy profiles $F(\Delta n) = -k_{\mathrm{B}}T \ln P(\Delta n)$ determined by umbrella sampling (see Appendix). The progression from convexity to bistability of $F(\Delta n)$ as $\beta\mu$ increases at fixed K and ϵ' is suggestive of Ising-like symmetry breaking. Quantitative features of $F(\Delta n)$ support this connection. In particular, near the transition Binder cumulants approach values characteristic of 3-dimensional Ising universality (see Appendix). However, we find evidence that the nature of the transitions becomes discontinuous between $K = 6$ and $K = 7$ (see Appendix).

Loading of proteins into the model thylakoid is thus accompanied by continuous transitions in $\langle \Delta n \rangle$, critical fluctuations, and correspondingly dramatic susceptibility. We locate this transition through the shape of the free energy profile. The striped phase is stable wherever $F(\Delta n)$ possesses global minima away from $\Delta n = 0$. Elsewhere, the thylakoid is macroscopically disordered, though stripe patterns may be prominent on microscopic scales.

Fig. 2.6 shows the phase diagram in the $(K, \beta\mu)$ plane. An equivalent but more intuitive representation in the plane of K and $\bar{n}$ is given in Fig. 2.7. Results are included for a broad range of ϵ' values. In all cases, computed phase boundaries are curves of Ising-like critical points. All boundaries are mirrored across the lines of inversion symmetry of Eq. (2.4), or $\bar{n} = 1/2$ in the $\bar{n}$ vs. K plane, respectively. As described in Sec. 2.5.2, striping transitions at finite ϵ' are re-entrant as a consequence for all finite steric repulsion strengths ϵ'. Modulated order requires sufficient filling of the lattice but is inevitably destroyed by high density.

The shapes of these phase diagrams clearly reflect the origin of modulated order in an interplay between proteins' attraction and steric repulsion. The domain of stability of the striped phase is largest where attraction and repulsion are both potent (*i.e.*, $\beta\epsilon'$ and K are both much greater than unity). Small values of either $\beta\epsilon'$ or K greatly compromise this stability, or eliminate it entirely.

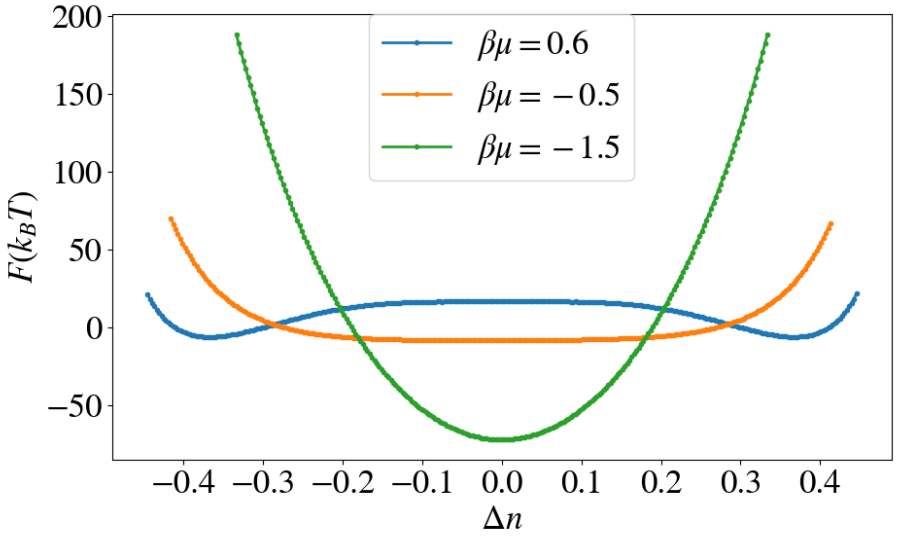

Figure 2.5: Statistics of the striping order parameter Δn at three different thermodynamic states. In all cases Monte Carlo simulations were performed with $\epsilon' = 20k_BT$, $J = 0.4k_BT$, $\epsilon = 1.65k_BT$ (corresponding to $K = 3.25$), $L_z = 24$, and $L_x = L_y = 10$. The free energy relative to thermal energy, $\beta F = -\ln P(\Delta n)$, is shown for $\beta\mu = -1.5$, $\beta\mu = -0.5$, and $\beta\mu = 0.6$. For the highest value of $\beta\mu$, macroscopic bistability indicates a striped state with long-ranged order and broken symmetry. For the lowest value of $\beta\mu$, Gaussian fluctuations in Δn typify the sparse disordered state. For the intermediate value of $\beta\mu$, the quartically flat shape of βF near $\Delta n = 0$ indicates proximity to a continuous ordering transition.

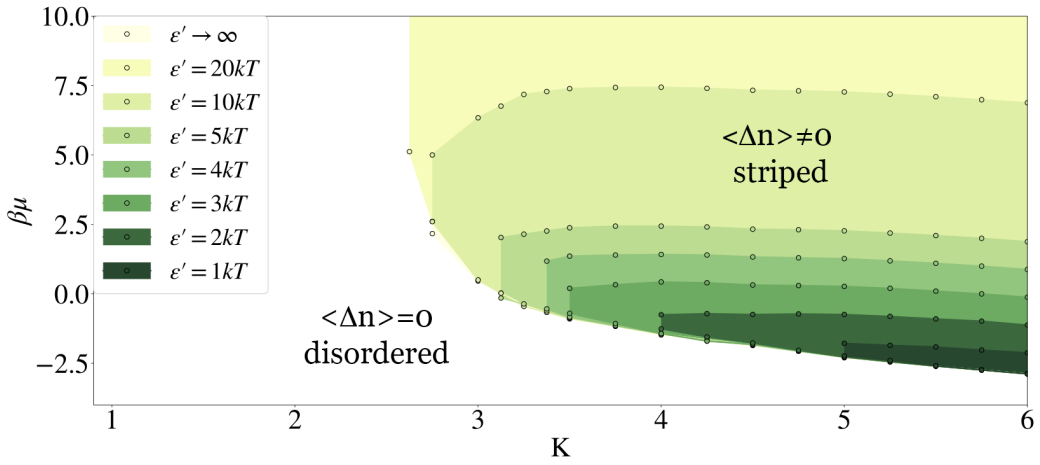

Figure 2.6: Phase diagrams of the thylakoid lattice model constructed from Monte Carlo simulation results, shown in the plane of attraction strength and chemical potential. Results are shown for several values of repulsion strength ϵ'. In the white region, the disordered phase is stable for all ϵ'. The region with darkest shading shows the range of $\beta\mu$ and K over which the ordered phase is stable for $\beta\epsilon' = 1$. The next darkest region shows the *additional* range of ordered phase stability at $\beta\epsilon' = 2$, and so on. All phase boundaries, which are assumed to follow straight lines between explicitly determined points (circles), mark continuous striping transitions. Results for the hard constraint limit, $\epsilon' = \infty$, are indistinguishable from those with $\beta\epsilon' = 20$.

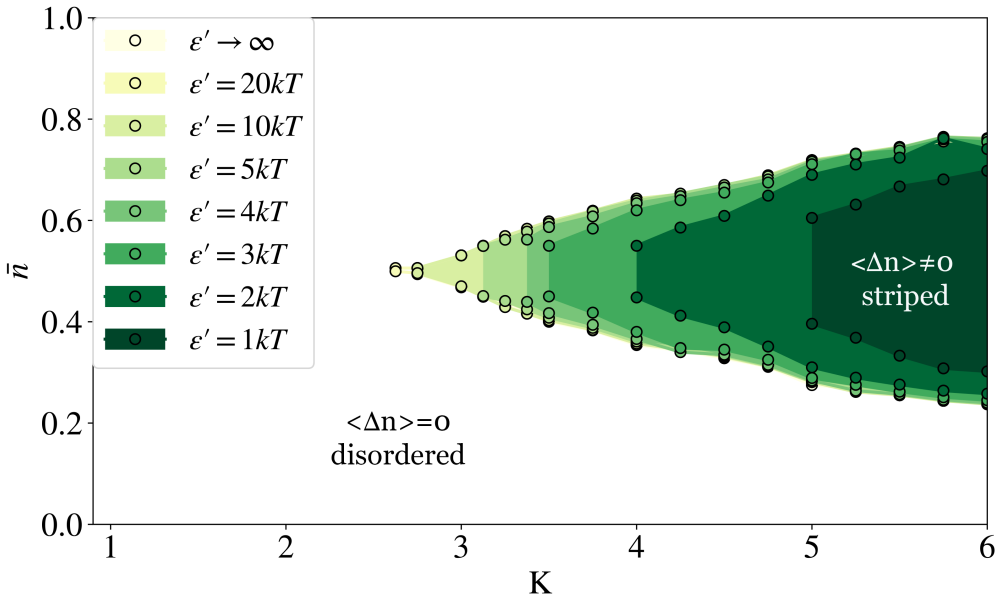

Figure 2.7: Phase diagrams of the thylakoid lattice model constructed from Monte Carlo simulation results, shown in the plane of attraction strength and density. Points and shading have the same meaning as in Fig. 2.6. Results for the hard constraint limit, $\epsilon' = \infty$, are indistinguishable from those with $\beta\epsilon' = 20$. For the latter case, $\beta\epsilon' = 20$, we did not impose high enough chemical potential in simulations to obtain results for $\bar{n} > 1/2$. In the hard constraint limit, the regime $\bar{n} > 1/2$ is strictly forbidden.

2.7 Methods: Mean field theory

As with most critical phenomena, the long-ranged correlation of protein density fluctuations implied by these phase transitions greatly hinders accurate analytical treatment. Here we employ the most straightforward of traditional approaches for predicting phase behavior, namely mean field (MF) approximations, to further explore and explain the ordering behavior revealed by Monte Carlo simulations of the thylakoid model. Though quantitatively unreliable in general, mean field methods provide a simple accounting for the collective consequences of local interactions, and thus a transparent view of phase transitions that result.

Mean field theories generically treat the fluctuations of select degrees of freedom explicitly, regarding all others as a static, averaged environment. We first consider a pair of fluctuating lattice sites in a self-consistent field, whose continuous transitions can be easily inferred. We then analyze an extended subsystem of 12 tagged lattice sites, whose qualitative predictions align with the simpler treatment. This consistency suggests a robustness of mean field predictions for the thylakoid model.

2.7.1 Two-site clusters

In order to describe modulated order of the striped phase, a subsystem for mean field analysis should include representatives from both layers of a thylakoid disc. Our simplest approximations therefore focus on a pair of tagged occupation variables, $n^{(1)}_{1,1}$ and $n^{(1)}_{2,1}$, describing density fluctuations at vertically neighboring lattice sites that interact directly through steric repulsion. We will describe mean field analysis for this two-site cluster first in the simplifying case $\epsilon' \to \infty$, *i.e.*, the hard constraint limit. We then consider the more general case of finite repulsion strength.

Hard constraint limit

In the limit $\epsilon' \to \infty$, the microstate $n^{(1)}_{1,1} = n^{(1)}_{2,1} = 1$ of our two-site cluster is prohibited. As a result, the mean field free energy F_{MF} can be written very compactly. We construct F_{MF} from (a) the Gibbs entropy associated with probabilities of the cluster's three allowed microstates and (b) the average energy of interaction with a static environment. In terms of the order

parameters $\bar{n}$ and Δn, we obtain

$$\begin{aligned}\frac{2\beta F_{\mathrm{MF}}}{N} &= -2\beta\mu\bar{n} + (\bar{n}+\Delta n)\log(\bar{n}+\Delta n) \\ &+(\bar{n}-\Delta n)\log(\bar{n}-\Delta n) \\ &+(1-2\bar{n})\log(1-2\bar{n}) - K(\bar{n}^2+\Delta n^2), \end{aligned} \tag{2.6}$$

where N is the total number of lattice sites. Eq. (2.6) suggests a close relationship between our thylakoid model and the well-studied 3-state Potts model of interacting spins. Applying the Curie-Weiss MF approach to that Potts model yields a free energy of identical form to Eq. 2.6 for the case of an external field that couples symmetrically to two of the spin states. [37] The MF phase behavior of the two models is therefore isomorphic, involving both first-order and continuous symmetry-breaking transitions. The continuous transitions are qualitatively consistent with results of our Monte Carlo sampling. The discontinuous transitions were not observed in thylakoid model simulations for $K < 6$; evidence for them emerges only for larger values of K, where sampling becomes challenging.

Continuous transitions may be identified by expanding Eq. (2.6) for small Δn. This expansion indicates a local instability to symmetry-breaking fluctuations that first appears at $\bar{n} = K^{-1}$. A corresponding phase boundary in the $(K, \beta\mu)$ plane can then be found by minimizing F_{MF} with respect to $\bar{n}$, yielding $\beta\mu = -1 - \ln(K-2)$. This result, plotted as the black curve in Fig. 2.8, captures the most basic features of our simulation results at large $\beta\epsilon'$. As is typically true, the maximum temperature at which ordering occurs is overestimated by MF theory (*i.e.*, the minimum value of K is underestimated).

For sufficiently large K, numerical minimization of F_{MF} reveals transitions that are instead discontinuous, as shown in the red curve in Fig. 2.8. Here, the disordered state remains locally stable while global minima emerge at nonzero Δn. The onset of such transitions at $K^* = 10/3$ can be determined by careful Taylor expansion of F_{MF} in powers of $\bar{n}$ and Δn (see Appendix). Both of these order parameters suffer discontinuities at the first-order phase boundary. For $K < K^*$, no discontinuous transitions are observed; in terms of Fig. 2.8, the red curve begins at K^*.

The absence of first-order transitions in computer simulations could signal a failure of this simple mean field theory. Alternatively, such transitions may occur only at temperatures lower than the range examined. This low-temperature regime is challenging to explore with our Monte Carlo sampling

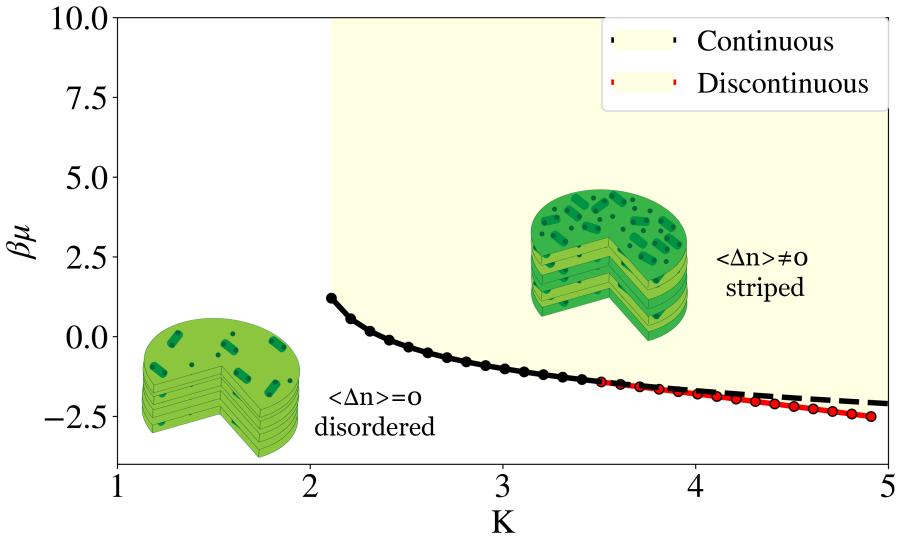

Figure 2.8: Phase diagram of the thylakoid lattice model determined from mean field theory in the hard constraint limit $\epsilon' = \infty$, shown in the plane of attraction strength and chemical potential. In the white region, Eq. 2.6 has a single minimum, at $\Delta n = 0$, indicating a lack of striped order. In the shaded region, global minima at nonzero Δn indicate symmetry breaking, *i.e.*, striping with long-range coherence. The extremum of F_{MF} at $\Delta n = 0$ changes stability at the black curve, allowing for continuous ordering. At large K this continuous change is preempted by a first-order transition (red curve).

methods. Below we will show that discontinuous transitions survive in more sophisticated MF treatments, suggesting they are a real feature of the model that is difficult to access with simulations.

Both simulations and MF theory indicate that the striping transition is not re-entrant in the hard constraint limit. High-density disordered states are prohibited by steric repulsion at $\epsilon' = \infty$.

Soft steric repulsion

The same basic MF approach can be followed for finite ϵ'. In this case, however, F_{MF} is written most naturally not as a function of $\bar{n}$ and Δn, but

instead in terms of probabilities $p_{n_1 n_2}$ for the four possible cluster microstates:

$$\begin{aligned}\frac{2\beta F_{\mathrm{MF}}}{N} &= p_{00}\ln p_{00} + p_{10}\ln p_{10} + p_{01}\ln p_{01} + p_{11}\ln p_{11} \\ &\quad - \frac{K}{2}[(p_{11}+p_{10})^2 + (p_{11}+p_{01})^2] \\ &\quad + \beta\epsilon' p_{11} - \beta\mu(p_{10}+p_{01}+2p_{11}) \end{aligned} \tag{2.7}$$

Recognizing that $\Delta n = (p_{10} - p_{01})/2$ and $\bar{n} = (p_{10} + p_{01} + 2p_{11})/2$, expansion and minimization of Eq. (2.7) yields continuous transitions in the (K, n) plane along

$$\bar{n} = \frac{1}{2} \pm \frac{1}{2K}\sqrt{(K-2)^2 - 4\delta} \tag{2.8}$$

where $\delta = e^{-\beta\epsilon'}$. The two values of $\bar{n}$ for each $K > 2(1+\sqrt{\delta})$ mark transitions to the low- and high-density disordered phases, reflecting the occupation inversion symmetry discussed in Sec. 2.5.2. In the $(K, \beta\mu)$ plane these transitions occur at

$$\beta\mu = \beta\epsilon' - K\bar{n} + \ln(K\bar{n} - 1) \tag{2.9}$$

where $\bar{n}$ refers to either solution of Eq. 2.8. Viewed as functions of K at given ϵ', the two branches of $\beta\mu$ in Eq. 2.9 have the peculiar feature of crossing at a certain attraction strength $K = K_{\mathrm{cross}}(\epsilon')$ (see Appendix). For $K > K_{\mathrm{cross}}$ these solutions violate fundamental stability criteria of thermodynamic equilibrium (see Appendix) and therefore cannot be global minima of the free energy. Lower-lying minima indeed appear at $K^* < K_{\mathrm{cross}}$, preempting the continuous ordering transition before the two solutions cross.

The development of nonzero $\langle \Delta n \rangle$ with increasing density is thus predicted to become discontinuous at sufficiently low temperature, as in the hard constraint case. The onset of this first-order transition,

$$K^* = \frac{10}{3} + \frac{2}{3}\delta + \mathcal{O}(\delta^2), \tag{2.10}$$

can be determined by Taylor expansion of F_{MF} in the regime of strong repulsion, *i.e.*, large ϵ' and small δ. Figs. 2.9 and 2.10 show mean field phase diagrams for several values of ϵ', as determined by numerical minimization of Eq. 2.7. For this mean field method, it is unnecessary to assume a value for J/ϵ, as the mean field blurs distinctions between vertical and in-plane couplings for sites coupled via J or ϵ. As in the simulation results of Figs. 2.6

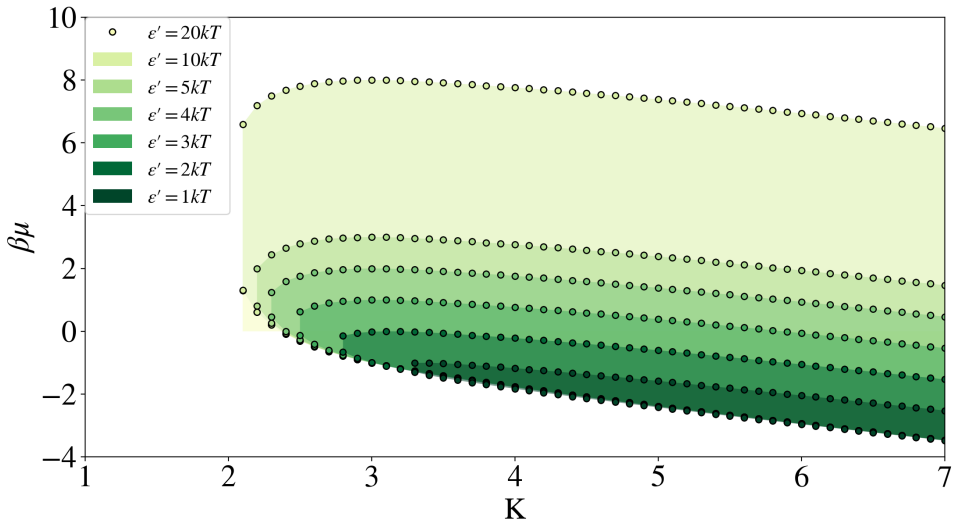

Figure 2.9: mean field phase diagram of the thylakoid lattice model at finite ϵ', shown in the $(K, \beta\mu)$ plane. Shading has the same meaning as in Fig. 2.6. Phase boundaries, determined by minimizing Eq. 2.7, are continuous at small K and discontinuous beyond a value K^* that is well approximated by Eq. 2.10.

and 2.7, the data in Figs. 2.9 and 2.10 exhibit the symmetry guaranteed by duality. Discontinuous changes in density upon striping imply regions of coexistence between ordered and disordered phases, spanning intermediate values of $\bar{n}$ as shown in Fig. 2.10.

The domain of stability of the striped phase in mean field theory evolves with ϵ' in the same basic way observed in Monte Carlo simulations. Relative to simulations, however, mean field results are consistently shifted to lower K (higher T), increasingly so as ϵ' decreases. The discontinuous nature of mean-field transitions at high K is not easily corroborated by simulations, as sampling becomes challenging for $K > 6$. Limited simulations of the system for $K > 6$ suggest first-order transitions appear between $K = 6$ and $K = 7$, rather than between $K = 3$ and $K = 4$; see Appendix for details. Consequently, the coexistence regions displayed in Fig. 2.10 do not appear in simulation for $K < 6$.

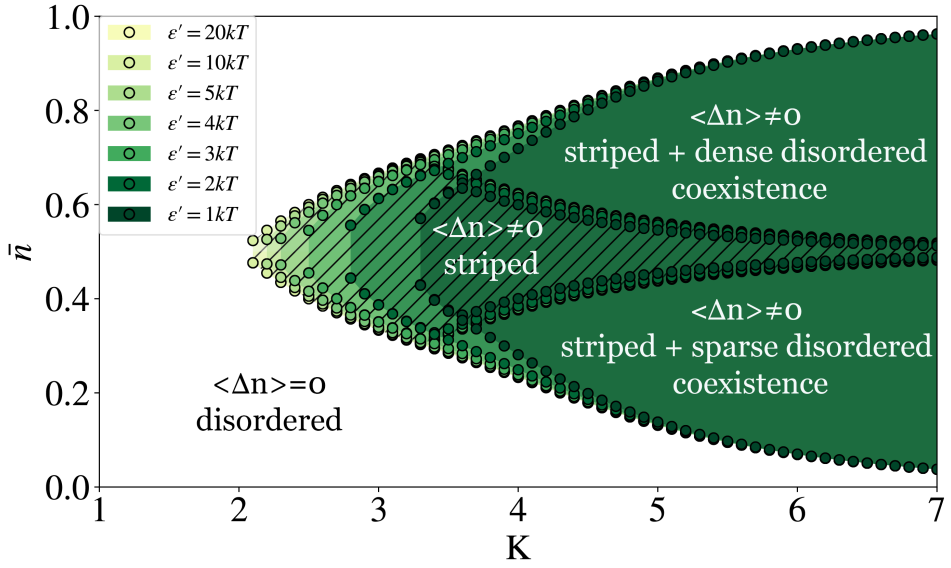

Figure 2.10: mean field phase diagram of the thylakoid lattice model at finite ϵ', shown in the $(K, \bar{n})$ plane. Hatched regions indicate the striped phase, and the coloration corresponds to that of Fig. 2.6. Shaded but un-hatched regions mark coexistence between striped and disordered phases. Phase boundaries, determined by minimizing Eq. 2.7, are continuous at small K and discontinuous beyond a value K^* that is well approximated by Eq. 2.10. The lines between coexistence regions and the striped phase merely mark the threshold densities between the striped phase and a coexistence region. The lines outlining the outer edges of the coexistence regions are the first-order transition lines obtained by minimizing Eq. 2.7.

2.7.2 Bethe-Peierls approximation

The accuracy of MF theory is generally improved by examining a larger set of fluctuating degrees of freedom. [51] In some cases, considering large clusters can even remove spurious transitions suggested by lower-level calculations. MF treatments of anisotropic Ising models, some of which incorrectly predict discontinuous transitions, are particularly interesting here. Neto *et al.* have surveyed an array of MF approaches for one such model in two dimensions, which supports modulated order at low temperature. The simplest MF calculations predict a crossover from continuous to discontinuous ordering. The Bethe-Peierls (BP) approximation, a more sophisticated MF approach, captures the strictly continuous ordering observed in computer simulations. [52]

We have performed BP analysis for the thylakoid model (in 3 dimensions), in order to test the robustness of phase behavior predicted by the two-site calculations described above. Here, we enumerate all microstates of a subsystem that includes $n_{1,1}^{(1)}$, $n_{2,1}^{(1)}$, *and* all of their remaining nearest neighbors, a total of 12 sites. The additional sites experience effective fields representing interactions that are not explicitly considered. For the specific case $J = \epsilon$, only two of these fields may be distinct, greatly simplifying the self-consistent procedure. We focus exclusively on this case. The calculation and phase diagrams that result are presented in Appendix.

Like simpler MF approaches, the BP approximation yields several solutions for the effective fields at low temperature. Some of these solutions correspond to continuous ordering transitions, which can also be identified by Taylor expansion of the self-consistent equations. Other solutions describe symmetry-broken states that do not appear continuously, resembling in many respects the first-order transitions predicted by two-site calculations. Demonstrating that these states are thermodynamic ground states would require formulating a free energy for this BP approach, which we have not pursued. Their local stability, however, is clearly preserved in the BP scheme.

The most pronounced difference between BP phase diagrams and those of simpler MF treatments is a shift of phase boundaries to lower temperature (higher K). Agreement with Monte Carlo simulations is therefore improved. With this shift, the onset of discontinuous transitions suggested by BP calculations occurs near $K = 6$, the highest value of K we studied by simulation. This result supports the notion that first-order transitions are a real feature

of the thylakoid model, occurring in a temperature range that is not easily accessed by simulation. Limited samplings of the system via simulation at $K > 6$ suggest first-order transitions occur in simulation between $K = 6$ and $K = 7$, further confirming the improved accuracy of BP over simpler MF methods; see Appendix.

2.8 Discussion

The model we have constructed to study vertical arrangement of proteins in grana stacks is sparse in microscopic detail. It does not distinguish among the associating protein species in photosynthetic membranes, nor does it account for shape fluctuations of lipid bilayers in which these proteins reside. But unless these unresolved features generate long-range correlations of their own, they are unlikely to alter the basic ordering scenario we have described. Such details are instead important in setting the parameters of a coarse-grained representation like Eq. (2.3). The finite size of grana stacks will round off sharp transitions and limit divergences, but natural photosynthetic membranes should be large enough to exhibit micron-scale cooperativity in protein rearrangements.

The biological relevance of these rearrangements depends on the effective physiological values of parameters like K, ϵ', and $\beta\mu$. Inherent weakness of attraction or repulsion, or else extreme values of protein density, could prevent thylakoids from adopting a striped phase. Photosynthetic membranes, however, visit states in the course of normal function that vary widely in protein density and in features that control interaction strength. We therefore expect significant excursions in the parameter space of Figs. 2.6 and 2.7. Since ordering transitions in our model require only modest density and interactions not much stronger than thermal energy, we expect proximity to phase boundaries to be likely in natural systems. Biological relevance depends also on the functional consequences of striped order. Photochemical kinetics and thermodynamics are determined by details of microscopic structure that we have made no attempt to represent, in particular, gradients in pH. If those aspects of intramolecular and supermolecular molecular structure are sensitive to local protein density or to the nanoscale spacing between dense regions, then striping transitions could provide a way to switch sharply between distinct functional states.

Given the limited availability of thermodynamic measurements on photo-

synthetic membranes, making quantitative estimates of the control variables K, ϵ', and $\beta\mu$ for real systems is very challenging. We will focus on the current qualitative knowledge of properties that are conjugate to these parameters, in order to explore which phases could be pertinent to which functional states.

The majority of precise measurements on grana have assessed the density of specific proteins, which is of course conjugate to their chemical potential. For this reason we have presented phase diagrams in terms of both $\beta\mu$ and $\bar{n}$.

The net attraction strength relative to temperature, K, is conjugate to the extent of protein association within each membrane layer and across the stromal gap. Because experiments suggest stacking interactions have an empirically measured, dramatic effect on protein association, [20, 22, 23, 24, 25] we will focus on the extent of stacking as a rough proxy for K. Previous computational work suggests that the range of K we have explored is physiologically reasonable. Focusing on lateral protein ordering in a pair of membrane layers, Refs. [8, 53] found that configurations consistent with atomic force microscopy images could be obtained for weak in-plane protein-protein attractions of energy $\leq 2k_BT$ and stacking energy $4k_BT$. Associating the energy scales of that particle model with the energies of our more coarse-grained lattice representation ($\beta J \lesssim 2$ and $\beta\epsilon \approx 4$) suggests values of K in the neighborhood of 5-10.

The strength of steric repulsion, ϵ', is strongly influenced by thylakoid geometry. For a very narrow lumen and very rigid phospholipid bilayers, PSII molecules on opposite sides of a thylakoid disc are essentially forbidden to occupy the same lateral position, a hard constraint that is mimicked by the limit $\epsilon' = \infty$ of Sec. 2.7.1. Greater luminal spacing, together with membrane flexibility, abates or possibly nullifies this repulsion. We therefore regard thylakoid thickness as a rough readout of ϵ'. Since thylakoid thickness changes significantly as light conditions change, we also view ϵ' as a control variable related to light intensity.

In high light conditions, the luminal gap of the thylakoid discs widens. [54, 55] This geometric change should ease steric repulsion, though lumen widening is less substantial at the center of the discs than at their edges. [56, 57] If the light intensity is particularly high, this expansion can be accompanied by the disassembly of PSII-LHCII mega-complexes (and, to a much lesser extent, super-complexes) en route to PSII repair. [26, 54, 55, 58, 59] Although this disassembly is primarily limited to the edges of the thylakoid, we infer an overall decrease in the extent of stacking. And because PSII is

subsequently shuttled to the stroma for repair, we also expect a concomitant decrease in protein density. The implied low to modest values of $\beta\mu$, ϵ', and K suggest that high light scenarios favor the sparse disordered phase of our model.

In low light conditions, thylakoid discs are thinner, and the stromal gaps between them decrease as well [6, 15], pointing to large values of ϵ' and K. The low-light physiological state thus appears to be the strongest candidate for the striped phase we have described.

During state transitions, a collection of changes causes the balance of electronic excitations to shift from PSII to photosystem I. [26, 56, 57, 60, 61] Among these changes, a diminution of stacking and a shift of LHCII density towards the stroma lamellae are closely related to the ordering behavior of our thylakoid model. Both result from phosphorylation of some fraction of the LHCII population, which weakens attraction between discs, prompts disassembly of a fraction of PSII-LHCII mega-complexes and super-complexes, and allows LHCII migration towards the thylakoid margins. The corresponding reduction of $\beta\mu$ and K is likely to be highly organism-dependent, since the extent of phosphorylation varies greatly from algae to higher plants. [57, 60, 61, 62, 63, 64] Lacking as well quantitative information about thylakoid thickness, it is especially difficult to correlate state transitions with the phase behavior of our model. In the case of very limited phosphorylation (as in higher plants), the ordered and sparse disordered phases both seem plausible. With extensive phosphorylation (as in algae), substantial reductions in stacking attraction and density make the ordered state unlikely.

The relationship among granum geometry, protein repulsion strength, and long-range stripe order suggests interesting opportunities for manipulating the structure and function of thylakoid membranes in vivo. By adjusting the luminal spacing, mechanical force applied to a stack of discs in the vertical direction (*i.e.*, the direction of stacking) should serve as a handle on the steric interaction energy ϵ'. The phase behavior of our model suggests that smooth changes in force can induce very sharp changes in density, protein patterning, and stack height. Ref. [56] demonstrates a capability to manipulate thylakoids in this way, and could serve as a platform for testing the realism of our lattice model. Complementary changes in attraction strength might be achieved by controlling salt concentration, a strategy used in Ref. [21] to examine the influence of stacking interactions on lateral ordering of proteins in a pair of thylakoid discs.

2.9 Conclusion

The computer simulations and analysis we have presented establish that ordered stripes of protein density, coherently modulated from the bottom to the top of a granum stack, can arise from a very basic and plausible set of ingredients. Most important is the alternation of attraction and repulsion in the vertical direction, a feature that is strongly suggested by the geometry of thylakoid membranes. Provided the scales of these competing interactions are both substantial, a striped state with long-range order will dominate at moderate density. Under conditions accessible by computer simulation, the striping transition is continuous, with critical scaling equivalent to an Ising model or standard lattice gas. Mean field analysis suggests that the transition becomes first-order for strong attraction, switching sharply between macroscopic states but lacking the macroscopic fluctuations of a system near criticality.

Simple mechanisms for highly cooperative switching have been proposed and exploited in many biophysical contexts, [45, 46] including the lateral arrangement of proteins in photosynthetic membranes. [7, 18, 21, 26, 54, 56, 58, 60, 61, 62, 64] We suggest that vertical ordering in stacks of such membranes can be a complementary mode of collective rearrangement with important functional consequences.

Chapter 3

Lattice models for mechanical responses of thylakoid membrane stacks to changes in illumination

3.1 Preface

The text of this chapter is a proto-manuscript that will eventually be submitted for publication. The Supplemental Information is given in Appendix 5.2.

3.2 Abstract

Proteins in photosynthetic membranes can form organized lateral structures under certain illumination criteria. Changes in illumination alter their ordering, as light conditions impact both protein-protein interactions and membrane morphology. Protein interactions include both attractive and repulsive forces, and their competition decides both the density and degree of order. Here we explore how the interplay between these opposing driving forces is influenced by membrane mechanics. We propose a lattice model that roughly accounts for fluctuation of lumenal gap thickness, in addition to proteins' attraction within a layer and across the stromal gap, steric repulsion across the varying lumenal gap, and regulation of protein density by exchange with the

stroma lamellae. Mean field analysis and computer simulation reveal rich phase behavior for this model, featuring a broken-symmetry striped phase that is disrupted at both high and low extremes of chemical potential, as well as unstructured phases that occur at extremes of chemical potential and for less rigid membranes. The resulting sensitivity of microscopic protein arrangement to the thylakoid's mesoscale vertical structure and membrane plasticity raises intriguing possibilities for regulation of photosynthetic function via mechanical forces.

3.3 Introduction

In the previous chapter we focused on the interplay between attractive and repulsive protein-protein forces within grana stacks, and we found that a model with those simple features may explain a significant range of physiological conditions. The preceding chapter showed how membrane geometry impacts ordering; it follows that mechanical forces coupled to this geometry can influence the stability of ordered phases. This chapter extends our previous study by permitting the inner gap thickness of individual thylakoid discs to vary along with proteins' spatial distributions. The inclusion of fluctuating gap thicknesses allows us to examine how external mechanical forces can influence large-scale protein organization.

Our extended model is inspired by the approach and results of Ref. [56], which measured membrane elasticity and lumenal gap thickness as a function of PSII-targeting illumination. In addition to wider gaps, Clausen *et al.* found increased elasticity upon higher illumination intensity. They also examined changes in the extent of stacking due to varied illumination, confirming previously measured trends. Their results recommend the use of techniques like atomic force microscopy (AFM) for uses other than imaging. For over a decade AFM has been used to manipulate membranes [65], though its applications to photosynthetic membranes were primarily for imaging purposes. [7, 23, 24, 66] We hope that complementing the work of Clausen *et al.* with theoretical studies could inspire further study of mechanical aspects of photosynthetic membranes. Varying the force strength under constant illumination, however, has not been explored. Our work suggests that external mechanical forces can influence thylakoid protein organization much like illumination does.

In order to examine the basic physical requirements for protein corre-

lations spanning an entire stack of thylakoids, we develop minimal models that account for locally fluctuating protein populations and per-disc fluctuating lumenal gaps in a granum-like geometry. As described in Sec. 3.4, population fluctuations are biased by protein-dependent attractions between discs, and by steric repulsion between proteins that reside in the same disc. Gap fluctuations influence this steric repulsion to a degree dictated by the inherent stiffness of the membrane. The strengths of these interactions are determined by parameters that roughly represent light conditions and protein phosphorylation states. Using methods of mean field theory presented in Sec. 3.6, as well as Monte Carlo simulation detailed in Sec. 3.7, we find that strongly cooperative behavior emerges over a wide range of conditions. As parameter values are changed, the model system can cross phase boundaries where intrinsic symmetries are spontaneously broken or restored. The correspondingly sudden changes in the microscopic arrangement of photosynthetic proteins suggest a mechanism for switching sharply between distinct states of light harvesting activity, as discussed in Sec. 3.8. In Sec. 3.9 we conclude.

3.4 Model

3.4.1 Physical description

Our model, like that of Chapter 2, describes stacked thylakoid discs by extending the familiar lattice gas model of liquid-vapor phase transitions. As before, we represent protein arrangements on a cubic lattice. Proteins' identities and internal structures are not resolved here; by discretizing space at the scale of a protein diameter, we have essentially averaged out such details.

The novel feature of this model is the lumenal gap thickness θ, which we permit to fluctuate subject to several forces. The presence of proteins that protrude into the lumen generates forces that tend to enlarge the gap. An external force $N_{xy} f_{\text{ext}}$, where N_{xy} is the number of lattice sites in a single membrane layer, could be compressive ($f_{\text{ext}} > 0$) or expansive ($f_{\text{ext}} < 0$) when applied vertically to the membrane stack. Finally, the extent of fluctuations in θ is governed by an intrinsic stiffness of the membrane structure, whose restoring force we take to be linear in θ, à la Hooke's Law with a spring constant $N_{xy}k$. A large k signifies a stiff membrane for which lumenal gaps hardly deviate from their average value. Conversely, a small k suggests a loose membrane, in which lumenal gaps may vary widely, enabling the ac-

commodation of more protein per layer. In our original model, θ was held implicitly fixed, corresponding to very large k but also implicitly requiring large forces to switch between gap thicknesses characterizing different light conditions.

The fluctuating degrees of freedom are thus binary variables n for each lattice site, indicating the local scarcity ($n = 0$) or abundance ($n = 1$) of protein, and continuous variables θ, indicating the lumenal gap size for each disc. We refer to the local states $n = 0$ and $n = 1$ as unoccupied and occupied, respectively, although they do not strictly indicate the presence of an individual molecule.

The net protein density in our model membranes may fluctuate according to a chemical potential μ. Such variations generally represent exchange of material with a reservoir. In our case the stroma lamellae – unstacked regions of photosynthetic membrane – could play the role of reservoir. Interaction energies are defined as in our previous model; see Fig. 2.1, as well as Figs. 3.1 and 3.2.

In the previous chapter, we noted that the steric repulsion strength may be significantly influenced by the average lumen thickness, which dictates the severity of deformations required to avoid steric overlap. Here we acknowledge this dependence explicitly, regarding ϵ' as a function of the fluctuating gap thickness θ. We expect $\epsilon'(\theta)$ to decrease monotonically with increasing θ, but there is little data to justify a specific mathematical form. We adopt the simplest choice,

$$\epsilon'(\theta) = \epsilon'(\theta_0) - (\theta - \theta_0)f, \tag{3.1}$$

a linear expansion about a reference gap thickness θ_0. An appropriate reference, and the repulsion strength $\epsilon'(\theta_0) > 0$ it implies, could vary with light conditions, as could the spring constant k for membrane fluctuations. We expect these parameters, however, to be largely dictated by features of the membrane, such as bilayer lipid lengths, that are not significantly affected by changing light conditions. The proportionality constant f in Eq. 3.1 is positive, ensuring that repulsion is alleviated by swelling of the lumen.

Introducing lumenal gap fluctuations to the thylakoid model modifies its phase behavior in several interesting ways, but the essential nature of its stable phases is unchanged. Ground states now depend on a larger set of parameters (μ, ϵ, J, k, θ_0, $\epsilon'(\theta_0)$, f, f_{ext}, and temperature), but only a few combinations of these quantities are essential to the phase transitions we will describe. As in the previous chapter, large, positive μ encourages occupation

and thus favors a high average value $\bar{n}$ of the local occupation variable. In the limit $\mu \to +\infty$, a state of complete occupation is thus energetically minimum.

At high μ we generally expect densely populated thermodynamic states, as depicted in Fig. 2.2. Conversely, at very negative values of μ we expect very sparse equilibrium states, as depicted in Fig. 2.3. The magnitude of chemical potential values required for these extremes is now sensitive to all of the mechanical properties described by k and $\epsilon'(\theta)$. More interestingly, transitions between sparse and dense phases are now more varied. Distinguishing among these transitions is aided by an order parameter $\bar{\omega}$ that measures the extent of "double occupation" – the fraction of lateral sites where protein is present in both layers of a thylakoid disc. Distinctions between single and double occupation are portrayed in Fig. 3.2. Double occupation goes hand-in-hand with high density, and given the high densities typical of photosynthetic membranes, double occupancy is exceedingly common in thylakoid systems.

At modest μ, equilibrium states are characterized by competition among steric repulsion and the favorable energies of stacking and in-plane association. Large $\epsilon'(\theta)$ harshly penalizes lattice states that are more than half full – states which must feature simultaneous occupation of laterally aligned sites within the same disc. In order to realize in-plane attraction at half filling, one layer of each thylakoid must be depleted of protein. The stack then comprises a series of sparse and dense layers. Extensive stacking interaction between discs requires a coherent sequence of these layers, yielding ground states that are striped with a period of four layers. This pattern is illustrated in Fig. 2.4 and quantified by an order parameter Δn that compares protein density in the two layers of each thylakoid. Fig. 3.1 is a schematic representation of the striped phase in a low γ system, and Fig. 3.2 for a high γ system. More specifically, Δn is a linear combination of layer densities, whose coefficients change sign with the same periodicity as the stripe pattern described.

As before, the two layers of each disc are completely equivalent in our model energy function. Stripe patterns, which populate the two layers differently with a persistent periodicity, do not possess this symmetry. Equilibrium states with $\Delta n \neq 0$ therefore require a spontaneous symmetry breaking, and they must be separated from symmetric states by a phase boundary. The theoretical work reported in the rest of this chapter aims to determine what, if any, thermodynamic conditions allow for such symmetry-broken, coherently striped states at equilibrium, and addresses how their stability is influenced

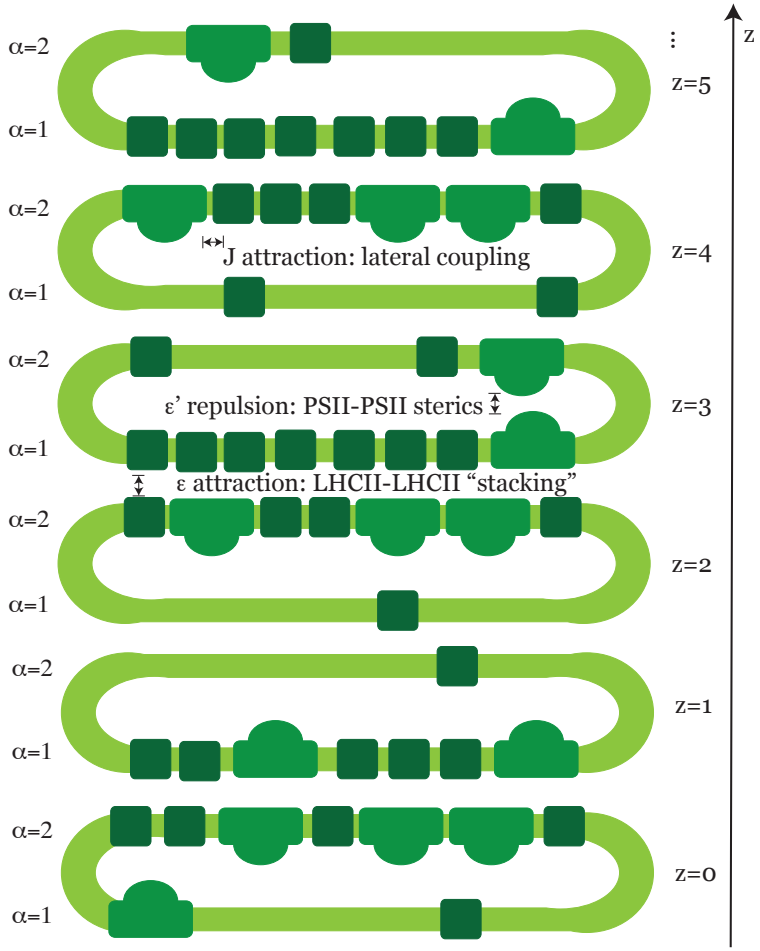

Figure 3.1: Schematic cross-section of a stack of thylakoids discs for low γ, which in the limit $\gamma \to 0$ becomes the model of the previous chapter. Dark green squares represent LHCII molecules, lighter green domed shapes represent PSII, and yellow-green bands represent lipid bilayers. Each disc (indexed by an integer z) comprises two layers (indexed $\alpha = 1$ and $\alpha = 2$). Protein attraction within each layer is assigned an energy scale J in our lattice model. Aligned LHCIIs in subsequent layers can engage in favorable stacking interactions, which is assigned an energy ϵ in the model. Protrusion of PSII into the lumen spaces (*i.e.*, the interior of each disc) may lead to steric repulsion between the two layers of each disc. Mediated by thylakoid thickness and membrane fluctuations, the effective steric energy scale is denoted ϵ'. Lumenal gap thickness θ is represented by the white space inside the discs. This system is in a striped state, as there is modulated vertical ordering.

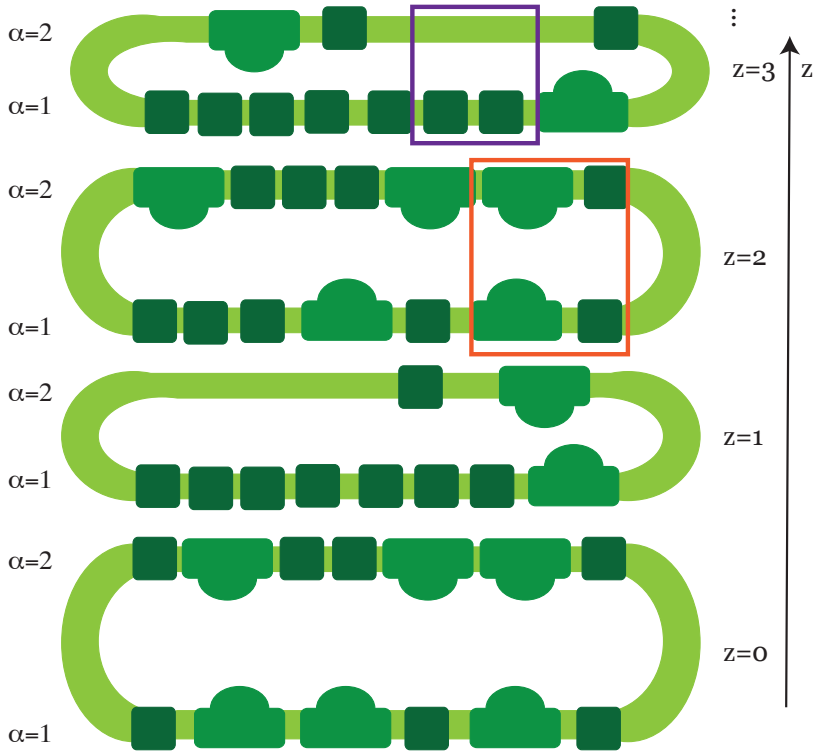

Figure 3.2: Schematic cross-section of a stack of thylakoids discs for high γ. All colors and shapes have the same meaning as in Fig. 3.1. The purple outlined area at $z = 3$ depicts two singly occupied sites, and the orange outlined area at $z = 2$ depicts two doubly occupied sites. At high γ the system may adopt a wider range of lumenal gap thickness values, thereby accommodating more density on both faces of wider thylakoid discs. Consequently, the propensity for purely striped states is diminished.

by fluctuations in θ. Possible physiological consequences of this organization will be discussed in Sec. 3.8.

3.4.2 Mathematical definition

In order to describe quantitatively the energetics and ordering we outlined above, it is useful to index lattice sites according to (a) the thylakoid disc to which they belong, specified by a vertical coordinate z ranging from 1 to L_z, (b) which layer of the disc they inhabit, $\alpha = 1$ (bottom) or $\alpha = 2$ (top), and (c) the lateral position, specified by an integer i ranging from 1 to N_{xy}. We consider variations $\theta^{(z)}$ of the lumenal gap thickness in the vertical direction, but for simplicity assume it is constant in x and y. (See Figs. 2.1, 3.1, and 3.2). The total energy of a configuration is written

$$\begin{aligned} H[\{n_{\alpha,i}^{(z)}\},\{\theta^{(z)}\}] = &-\mu \textstyle\sum_{z,\alpha}\sum_i n_{\alpha,i}^{(z)} + H_{\rm att} \\ &+\tfrac{1}{2}kN_{xy}\textstyle\sum_z(\theta^{(z)}-\theta_0)^2 \\ &+\textstyle\sum_z \epsilon'(\theta^{(z)})\sum_i n_{1,i}^{(z)} n_{2,i}^{(z)} \\ &+N_{xy}f_{\rm ext}\textstyle\sum_z(\theta^{(z)}-\theta_0) \end{aligned} \tag{3.2}$$

where $H_{\rm att}$ includes all contributions from protein-protein attractions,

$$\begin{aligned} H_{\rm att}[\{n_{\alpha,i}^{(z)}\}] = &-J\textstyle\sum_{z,\alpha}{\sum_{ij}}' n_{\alpha,i}^{(z)} n_{\alpha,j}^{(z)} \\ &-\epsilon\textstyle\sum_z\sum_i n_{2,i}^{(z)} n_{1,i}^{(z+1)} \end{aligned} \tag{3.3}$$

The chemical potential (μ) term, $H_{\rm att}$, and the $\epsilon'(\theta^{(z)})$ term were the focus of Chapter 2, except that ϵ' was treated as a constant. All other terms are new to this model. As before, the primed summation in Eq. 3.3 extends over distinct pairs of lateral nearest neighbors. As described above, each occupation variable $n_{\alpha,i}^{(z)}$ adopts values 1 (occupied) or 0 (unoccupied). At temperature T, the equilibrium probability distribution of $\{n_{\alpha,i}^{(z)}\}$ is proportional to the Boltzmann weight $e^{-\beta H}$, where $\beta \equiv 1/k_B T$.

Limits of Eq. 3.2 clarify the meaning of mechanical parameters we have introduced to represent gap thickness fluctuations. In the completely protein-occupied state ($n_{\alpha,i}^{(z)} = 1$ for all α, i, and z), the net force on each thylakoid disc is $-\partial H/\partial\theta^{(z)} = N_{xy}[f - f_{\rm ext} + k(\theta^{(z)} - \theta_0)]$, identifying f as an intrinsic force resulting from double occupation. In the opposite extreme of protein depletion ($n_{\alpha,i}^{(z)} = 0$ for all α, i, and z), the average gap thickness is $\langle\theta^{(z)}\rangle =$

$\theta_0 - f_{\rm ext}/k$, identifying θ_0 as the natural thickness of a protein-free thylakoid disc.

Density and striping order parameters are defined as before,

$$\bar{n} \equiv \frac{1}{N} \sum_{z,i,\alpha} n_{\alpha,i}^{(z)} \tag{3.4}$$

and

$$\Delta n \equiv \frac{1}{N} \sum_{z,i} (-1)^z (n_{1,i}^{(z)} - n_{2,i}^{(z)}), \tag{3.5}$$

where $N = 2L_z N_{xy}$ is the total number of lattice sites. The double occupation order parameter is

$$\bar{\omega} \equiv \frac{2}{N} \sum_{z,i} n_{1,i}^{(z)} n_{2,i}^{(z)}, \tag{3.6}$$

The simple harmonic form of Eq. 3.2, viewed as a function of $\theta^{(z)}$, allows an exact accounting for gap thickness fluctuations at any given protein configuration. The resulting bias on protein occupation variables is obtained from a straightforward Gaussian integration,

$$\beta H_{\rm eff}(\{n_{\alpha,i}^{(z)}\}) = -\ln \left[\int \left(\Pi_z d\theta^{(z)} \right) e^{-\beta H} \right],$$

yielding an effective potential for the remaining $n_{\alpha,i}$ variables,

$$\begin{aligned} H_{\rm eff} = \quad & -\mu \textstyle\sum_{z,\alpha} \sum_i n_{\alpha,i}^{(z)} + H_{\rm att} \\ & + \epsilon'_{\rm eff} \textstyle\sum_z \Omega^{(z)} - \frac{\gamma}{2N_{xy}} \sum_z [\Omega^{(z)}]^2 \end{aligned} \tag{3.7}$$

where we have defined the net double occupation of each disc

$$\Omega^{(z)} \equiv \sum_i n_{1,i}^{(z)} n_{2,i}^{(z)}$$

as well as the parameter combinations

$$\epsilon'_{\rm eff} \equiv \epsilon'(\theta_0) + (f/k) f_{\rm ext}, \quad \text{and} \quad \gamma \equiv f^2/k$$

Note that the effective steric repulsion $\epsilon'_{\rm eff}$ varies linearly with external force. This result, together with the connection between repulsion strength and light conditions discussed in Chapter 2, suggests that imposing force on

grana stacks could induce responses related to changing light conditions. Conversely, a change in light intensity could register substantially in measurements of vertical force.

Focusing on protein occupation statistics, the new feature in Eq. 3.7 resulting from gap fluctuations is an energy proportional to

$$[\Omega^{(z)}]^2 = \sum_i \sum_j n_{1,i}^{(z)} n_{2,i}^{(z)} n_{1,j}^{(z)} n_{2,j}^{(z)}.$$

This interaction directly couples protein fluctuations at four different sites within the same disc. It also extends over arbitrarily large lateral distances, a consequence of assuming the gap thickness to be independent of x and y. A more realistic model would acknowledge lateral variations in gap thickness, limiting the range of these four-site interactions. Provided that lateral variations in membrane shape are spatially gradual, however, the four-site interaction will have considerable range in that case as well. Our model mimics this long-distance coupling in an idealized way.

The four-site interaction is notably attractive, favoring dense protein occupation in contrast to the steric repulsion parameterized by $\epsilon'_{\rm eff}$. The competition stressed in Chapter 2, between forces that favor and disfavor high protein density, is thus enriched. Under the influence of fluctuating lumen thickness, a competition exists even within a single disc. We anticipate an interplay between this local competition and inter-disc stacking interactions that lead to striped ordering.

3.5 Basic consequences of lumenal gap fluctuations

The basic effects of including θ as a fluctuating variable are highlighted by considering a limit in which it provides the sole driving force for protein organization. We explore this limit by discarding protein attractions described by $H_{\rm att}$, *i.e.*, by setting $J = \epsilon = 0$. In the absence of stacking interactions, each disc is statistically independent, so we analyze fluctuations of a single disc (*e.g.*, $z = 1$). The partition function of this tagged disc,

$$Z = \sum_{\{n_{\alpha,i}\}} \exp\left[\beta\mu \sum_i (n_{1,i} + n_{2,i}) - \beta\epsilon'_{\rm eff}\Omega + \frac{\beta\gamma}{2N_{xy}}\Omega^2\right], \tag{3.8}$$

can be computed exactly in the thermodynamic limit $N_{xy} \to \infty$, due to the unbounded spatial range of four-site interactions. (Superscripts "(1)" in Eq. 3.8, indicating the arbitrary index of the tagged disc, have been omitted for simplicity.) We introduce a continuous auxiliary variable ϕ through

$$Z \propto \int d\phi \sum_{\{n_{\alpha,i}\}} \exp\left[\beta\mu \sum_i (n_{1,i} + n_{2,i}) - \beta\epsilon'_{\rm eff}\Omega - \frac{N_{xy}}{2\beta\gamma}\phi^2 + \phi\Omega\right], \tag{3.9}$$

This rewriting amounts to a Hubbard–Stratonovich transformation [67, 68], which casts ϕ as an effective fluctuating variable. Note that a simple Gaussian integration over ϕ returns Eq. 3.8 as a result. The transformation is not unique. As an integration variable, ϕ could be scaled by any constant; the coefficients of ϕ^2 and $\phi\Omega$ terms in Eq. 3.9 would change as a result, changing the natural scale of fluctuations in ϕ. In the form we have chosen, ϕ is intensive in scale, *i.e.*, its mean value is independent of N_{xy} in the thermodynamic limit.

The summation over occupation variables can now be carried out exactly. The result, $Z \propto \int d\phi \exp\left[-N_{xy} I(\phi)\right]$, is an integral dominated by contributions near the peak of a rate function,

$$I(\phi) = -\frac{\phi^2}{2\beta\gamma} + \ln\left(1 + 2a + a^2\delta e^{\phi}\right),$$

where $\delta = e^{-\beta\epsilon'_{\rm eff}}$ and $a = e^{\beta\mu}$. In the limit $N_{xy} \to \infty$, this saddle point dominance is complete, so that $Z \propto \exp\left[-N_{xy} I(\phi^*)\right]$, where ϕ^* locates the maximum of $I(\phi)$. Differentiating $I(\phi)$ to determine this maximum produces a nonlinear self-consistent equation,

$$\frac{\phi^*}{\beta\gamma} = \frac{a^2\delta e^{\phi^*}}{1 + 2a + a^2\delta e^{\phi^*}}, \tag{3.10}$$

with a form familiar from the mean field approximations presented in Chapter 2. Indeed, the approach followed here is tantamount to mean field theory, which is exact in this case of purely long-range interaction.

The self-consistent equation (3.10) can be cast more usefully by exploiting the connection

$$\frac{\partial \ln Z}{\partial \beta\gamma} = \frac{N_{xy}}{2(\beta\gamma)^2}\phi^{*2} = \frac{1}{2N_{xy}}\langle\Omega^2\rangle \tag{3.11}$$

and recognizing that $\bar{\omega} = \sqrt{\langle\Omega^2\rangle}/N_{xy}$ as a consequence of saddle point dominance. We then obtain an expression for the double occupancy order parameter,

$$\bar{\omega} = \frac{a^2\delta e^{\beta\gamma\bar{\omega}}}{1 + 2a + a^2\delta e^{\beta\gamma\bar{\omega}}},$$

or equivalently

$$m = \tanh\left(\frac{\beta\gamma}{4}m + h\right), \tag{3.12}$$

where $m = 2\bar{\omega} - 1$ and $h = (2\beta\mu - \beta\epsilon'_{\text{eff}} + \beta\gamma/2 - \ln(1+2a))/2$. The rewriting in Eq. 3.12 makes underlying symmetries of our model more transparent. In doing so, it also highlights an isomorphism with the classic Curie-Weiss mean field theory of the Ising model.

The phase behavior of our thylakoid model in the limit of vanishing attraction can be determined immediately from Eq. 3.12. For $h = 0$ a symmetry exists between configurations with and without double occupancy, and for $\beta\gamma > 4$ this symmetry is spontaneously broken. In other words, for temperatures below $\gamma/(4k_{\text{B}})$, two distinct phases are possible, distinguished by the degree of double occupation. These phases coexist at $h = 0$, defining a phase boundary $\beta\epsilon'_{\text{eff}} = 2\beta\mu + \beta\gamma/2 - \ln(1 + 2e^{\beta\mu}))$ in the plane of $\beta\epsilon'_{\text{eff}}$ and $\beta\mu$, as plotted in Fig. 3.3. Transitions at this boundary are discontinuous in $\bar{\omega}$. The state with $\beta\gamma = 4$ and $h = 0$ is a critical point in the mean field Ising universality class.

The thylakoid model of Chapter 2 did not feature a phase transition between unstructured phases of different density. From a sparse phase, increasing chemical potential could induce striped ordering, sometimes accompanied by a discontinuous change in density. From this striped phase, further increasing chemical potential destroys ordering upon transition to an unstructured dense phase. Sparse and dense phases are distinguished in that scenario, but under no conditions do they coexist. Fluctuating gap thickness

introduces this possibility, at least at $J = \epsilon = 0k_BT$. Whether that transition survives at nonzero attraction strength is not obvious. The relationship between unstructured phases in these two models is also not immediately clear. To address these questions we have employed Monte Carlo simulations and mean field approximations similar to those presented in Chapter 2.

3.6 Mean field theory

Here we deploy the most straightforward of traditional, analytical approaches for predicting phase behavior, namely MF approximations, to explore and explain the ordering behavior of the fluctuating-gap thylakoid model. Since the four-spin interaction of Eq. (3.7) couples all lattice sites of a disc with the same strength, we expect mean field methods to be more accurate than in the fixed-gap model of Chapter 2.

In order to describe modulated order of the striped phase, a subsystem for mean field analysis should include representatives from both layers of a thylakoid disc. We therefore focus on a pair of tagged occupation variables, $n_{1,1}^{(1)}$ and $n_{2,1}^{(1)}$, describing density fluctuations at vertically neighboring lattice sites that interact directly through steric repulsion.

As in Sec. 2.7 of Chapter 2, the mean field free energy F_{MF} is written most naturally in terms of probabilities $p_{n_1 n_2}$ for the four possible cluster microstates of our two-site cluster

$$\begin{aligned}\frac{2\beta F_{\mathrm{MF}}}{N} &= p_{00}\ln p_{00} + p_{10}\ln p_{10} + p_{01}\ln p_{01} + p_{11}\ln p_{11} \\ &\quad - \frac{K}{2}[(p_{11}+p_{10})^2 + (p_{11}+p_{01})^2] \\ &\quad + \beta\epsilon'_{\mathrm{eff}}p_{11} - \beta\mu(p_{10}+p_{01}+2p_{11}) - \frac{1}{2}\beta\gamma p_{11}^2 \end{aligned} \tag{3.13}$$

where $K = (4J+\epsilon)/k_BT$. Note that the four probabilities in Eq. 3.13 must add to one, $p_{00} = 1 - p_{11} - p_{10} - p_{01}$.

At equilibrium, the order parameters $\bar{\omega} = p_{11}$, $\bar{n} = (p_{10} + p_{01} + 2p_{11})/2$, and $\Delta n = (p_{10} - p_{01})/2$ take on values that minimize the mean field free energy. We locate these minima by differentiating F_{MF} with respect to each of p_{11}, p_{10}, and p_{01}. Requiring these derivatives to vanish generates a set of

three coupled self-consistent equations:

$$\begin{aligned} \Delta n &= p_{00} a e^{K\bar{n}} \sinh(K\Delta n) \\ \bar{n} &= p_{00} a e^{K\bar{n}} \big[\cosh(K\Delta n) + \delta a e^{K\bar{n}} e^{\beta\gamma\bar{\omega}} \big] \\ \bar{\omega} &= p_{00} \delta a^2 e^{2K\bar{n}} e^{\beta\gamma\bar{\omega}} \end{aligned} \tag{3.14}$$

where $p_{00} = (1 + 2ae^{K\bar{n}} \cosh(K\Delta n) + \delta a^2 e^{2K\bar{n}} e^{\beta\gamma\bar{\omega}})^{-1}$. We solve these equations numerically, iterating from an initial guess until convergence. (See Appendix 5.1 for details.)

Solving Eqs. (3.14), we identify several distinct phase transitions from discontinuous or non-analytic dependence of order parameters on control variables like $\beta\mu$ and $\beta\epsilon'_{\text{eff}}$. Some of these transitions follow the pattern discussed in Chapter 2 for a model with fixed lumenal gap thickness. Specifically, for sufficiently large K, increasing chemical potential yields macroscopically ordered stripes of protein density; further increasing $\beta\mu$ restores the symmetry that is spontaneously broken in the striped phase. These order-disorder transitions may be continuous or first-order, depending on the repulsion strength ϵ'_{eff}.

Some other transitions follow the pattern discussed above for a fluctuating gap with no protein attraction. Specifically, for sufficiently large γ, increasing chemical potential yields a discontinuous change in double occupancy at a density determined by ϵ'_{eff}. For $K = 0$ the critical value γ_{c}, above which these double occupancy transitions occur, is exactly $\beta\gamma_{\text{c}} = 4$. With $K > 0$, the double occupancy transitions occur in a different range $\gamma > \gamma_{\text{c}}(K)$. Because the attractions described by K promote dense population of the membrane, a system with higher K should require less potent four-spin interactions to achieve double occupancy. Indeed, according to mean field theory, γ_{c} decreases monotonically with increasing K. Note that for $\gamma = 0$ the onset K value is not infinite, because as described in Chapter 2, first-order transitions in Δn occur for $K = \frac{10}{3} + \frac{2}{3}\delta + \mathcal{O}(\delta^2)$, where $\delta = e^{\beta\epsilon'_{\text{eff}}}$.

For some combinations of K and γ, both of these phase scenarios occur. The top right image of Fig. 3.3 shows a representative mean field phase diagram for this case, in the plane of $\beta\epsilon'_{\text{eff}}$ and $\beta\mu$. Unstructured phases dominate at low and high $\beta\mu$. The route between them involves at least one phase transition. At low $\beta\epsilon'_{\text{eff}}$ the transition is direct and discontinuous. At higher $\beta\epsilon'_{\text{eff}}$, an ordered stripe phase intervenes: As density increases from a sparse unstructured state (upon increasing $\beta\mu$), symmetry in Δn is spontaneously broken, producing stripes with macroscopic coherence. This

order is subsequently destroyed at higher density, producing an unstructured state with intermediate density. At still higher $\beta\mu$, the double occupation transition yields an unstructured state with even higher density. Fig. 3.6 shows how these transitions are marked by changes in the order parameters for double occupancy ($\bar{\omega}$) and striping (Δn).

As K increases, the space between striping and double occupancy transitions narrows, and eventually closes. The two transitions then merge, as represented by the phase diagram in the bottom image of Fig. 3.3. In this case the loss of striped order at high $\beta\mu$ occurs simultaneously with an abrupt change in double occupancy. Unlike the phase behavior discussed in Chapter 2, the order-disorder transitions (at a given K and $\beta\epsilon'_{\text{eff}}$) have different character at low and high density. Here, the low-density transition is continuous, while the high-density transition is starkly discontinuous in both Δn and $\bar{\omega}$. This scenario is depicted in the left column of Fig. 3.6. For still larger values of K, the low-density transition also becomes discontinuous in Δn, while developing a kink in the double occupancy parameter $\bar{\omega}$, as shown in the right column of Fig. 3.6. The low-density transition does not become truly discontinuous in $\bar{\omega}$.

Fig. 3.4 shows the mean field phase diagram for an intermediate membrane stiffness, $\beta\gamma = 3$. Here the striped phase region resembles that of the model in Chapter 2, though now the high-density striping transition becomes discontinuous at lower coupling strength K than in the fixed-gap model. A short line of double occupancy transitions extends from the boundary of the striped phase towards low K, terminating at a critical point. This branch, which does not involve striping, is new to the fluctuating-gap model. As K increases, the corresponding coexistence curve merges with the high-density branch of the striped phase boundary. The low-density striping transition occurs much as in the fixed-gap model: Transitions are second-order up to $K \approx 10/3$, beyond which Δn changes discontinuously. For sufficiently large coupling, $K \approx 4.6$ and $K > 4.6$, the order parameter $\bar{\omega}$ also suffers a discontinuity upon striping.

Fig. 3.5 shows a mean field phase diagram typical of large γ. Here the line of double occupancy transitions extends all the way to $K = 0$, for both values of $\beta\epsilon'_{\text{eff}}$ shown. At this merged phase transition, Δn and $\bar{\omega}$ both experience a pronounced discontinuity. The low-density striping transition, however, remains continuous until $K \approx 3.1 - 3.3$ for $\beta\epsilon'_{\text{eff}} > 2$, and for $\beta\epsilon'_{\text{eff}} = 1$, the low-density striping transition becomes discontinuous within 0.5 K units of the initial $\beta\epsilon'_{\text{eff}} = 1$ low-density transition. Furthermore, the low-density

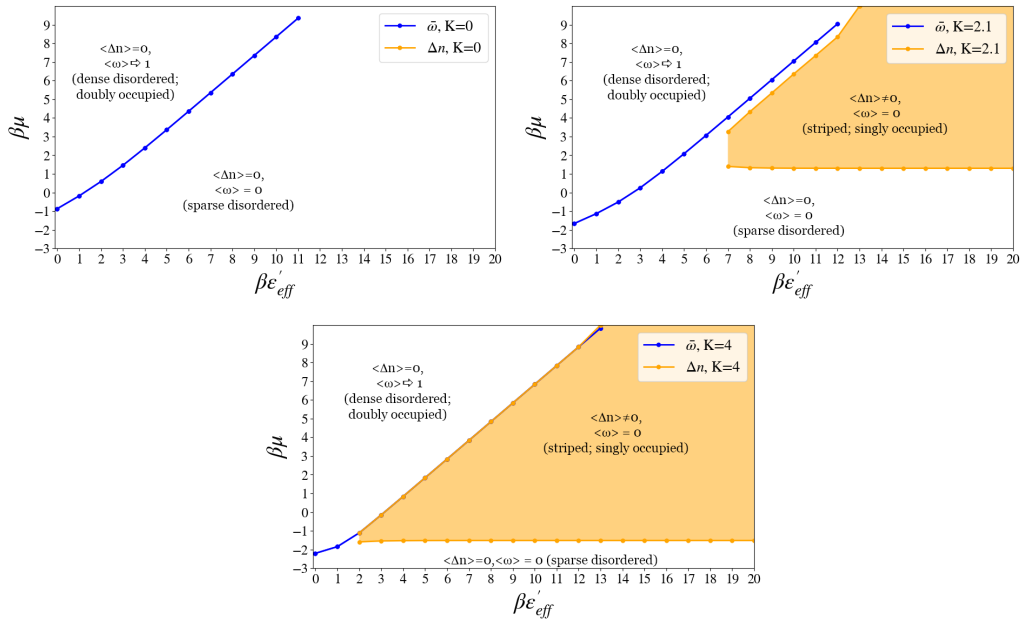

Figure 3.3: Phase diagrams constructed via mean field self-consistency, in the $\beta\mu$ vs. $\beta\epsilon'_{\text{eff}}$ plane for selected K. The top left image corresponds to $K = 0$ and represents the $\bar{\omega}$ transitions-only scenario; top right depicts $K = 2.1$ and the approach of continuous Δn transitions to $\bar{\omega}$ transitions; the bottom image represents $K = 4$, where the upper branch of Δn transitions meet $\bar{\omega}$ transitions and thereby become discontinuous. $\beta\gamma = 5$ for all three sub-figures.

striping transition is accompanied by a weak occupancy discontinuity for K values shortly following the K at which Δn initially varies discontinuously. Additionally, the overall phase diagram is slightly shifted to lower $\beta\mu$ than Fig. 3.4.

Yet another perspective on these mean field results is given in Figs. 3.6. The top two panels show phase diagrams in the $\bar{n}$ vs. $\beta\epsilon'_{\text{eff}}$ plane, for two different values of K. This plane focuses directly on the consequences of changing protein density, and of changing external force. Discontinuous changes in $\bar{\omega}$ are highlighted in this view, since the density undergoes concomitantly sharp change. As a visual consequence, these phase diagrams feature regions of coexistence, where a constraint on total density induces separation into two macroscopic phases separated by an interface. Such coexistence regions appear wherever striping or double occupancy transitions involve discontinuous change in $\bar{n}$, for example at the boundary between the striped phase and the dense disordered phase.

If one were to imagine even larger K at the same γ value, the striped region would continue to shrink in size, though the range over which a macroscopic fraction is striped would grow. Additionally, all Δn transitions – and, therefore, all the transitions for this model – would be discontinuous.

3.7 Monte Carlo simulations

As in Chapter 2, we employ computer simulations to examine the accuracy of mean field approximations underlying the phase diagrams in Figs. 3.3 to 3.5. For the fixed-gap thylakoid model, Monte Carlo simulations demonstrated a qualitative adherence to mean field phase behavior, but a substantial difference in the parameter ranges where phase transitions occur. For the fluctuating-gap model developed in this chapter, we expect a similar comparison, perhaps with improved quantitative agreement due to the long range of gap-induced protein attractions.

Our Monte Carlo methods sample the grand canonical probability distribution $e^{-\beta H}$ for a periodically replicated system with $L_x = L_y = 10$ and $L_z = 6$. This geometry can accommodate $L_z/4 = 3/2$ copies of the striped motif in the central simulation cell. Motivated by results of mean field theory, we limit attention to the case $J = \epsilon$, so that attraction strength is controlled solely by $K = (4J + \epsilon)/k_B T$. We present results for a few values of $\beta\gamma = 5$.

Under many conditions, thoroughly sampling $P(\bar{\omega})$ proved very difficult,

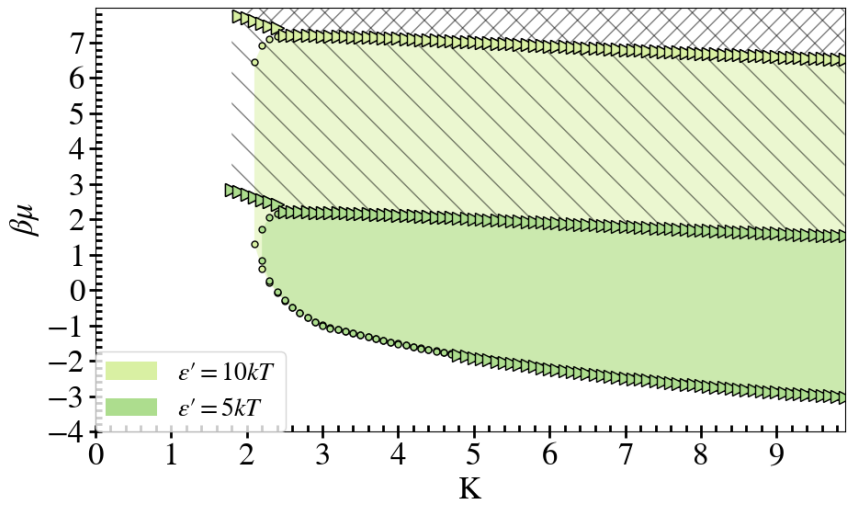

Figure 3.4: Phase diagram constructed via mean field self-consistency, in the $\beta\mu$ vs. K plane. Here $\beta\gamma = 3$. Green shaded regions represent the striped phase. Regions hatched with forward slashes indicate doubly occupied phase for $\epsilon' = 5k_BT$, and regions hatched with a backward slash indicate doubly occupied phase for $\epsilon' = 10k_BT$; cross-hatching occurs when these two regions coincide. White, un-hatched space denotes the sparse disordered phase. Triangular points mark $\bar{\omega}$ transitions, and open circles mark Δn transitions.

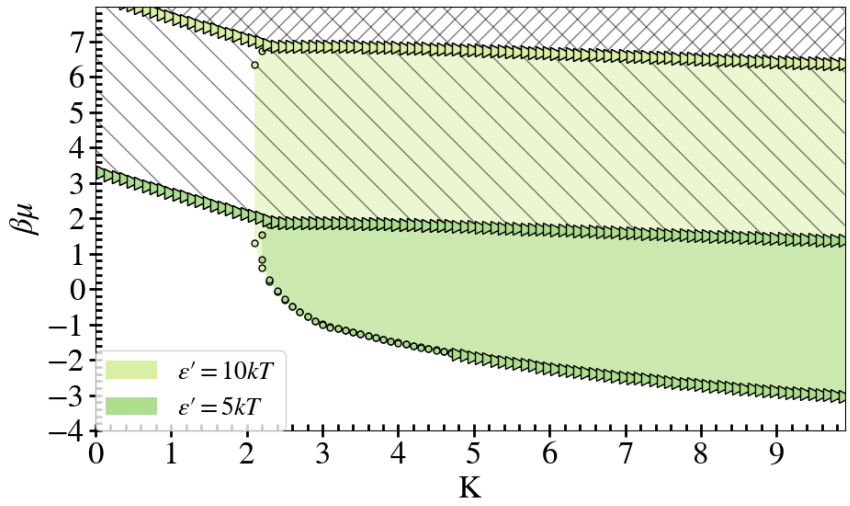

Figure 3.5: Phase diagram constructed via mean field self-consistency, in the $\beta\mu$ vs. K plane. Here $\beta\gamma = 5$. The meanings to symbols and colors in Fig. 3.4 apply here.

even at modest values of K. As such, transitions were primarily located by sudden changes in the average value $\langle\bar{\omega}\rangle$ computed without the bias of umbrella potentials. Transitions were further characterized via $\langle\Delta n\rangle$ and $\langle\bar{n}\rangle$. Striping transitions were also detected by these means.

These simulations generally confirm the phase transition scenarios deduced from mean field theory. Symmetry-breaking transitions, in which $\langle\Delta n\rangle$ becomes nonzero, occur as in the fixed-gap model but at lower values of $\beta\mu$.

Simulations also confirm that low-density and high-density striping transitions can have different character as a result of gap fluctuations. At low density we observe continuous ordering over the range of K where sampling is facile ($K < 6$), as in the fixed-gap model. At the high-density boundary of the striped phase, however, we observe discontinuous transitions, where average values of Δn (striping order parameter), $\bar{n}$ (density), and $\bar{\omega}$ (occupancy order parameter) all change abruptly. Recall that simulations of the fixed-gap model did not exhibit first-order transitions for comparable values of K.

Discontinuous transitions in $\bar{\omega}$ were identified similarly. For low values of K and/or ϵ'_{eff}, the double occupancy transition occurs in simulations without

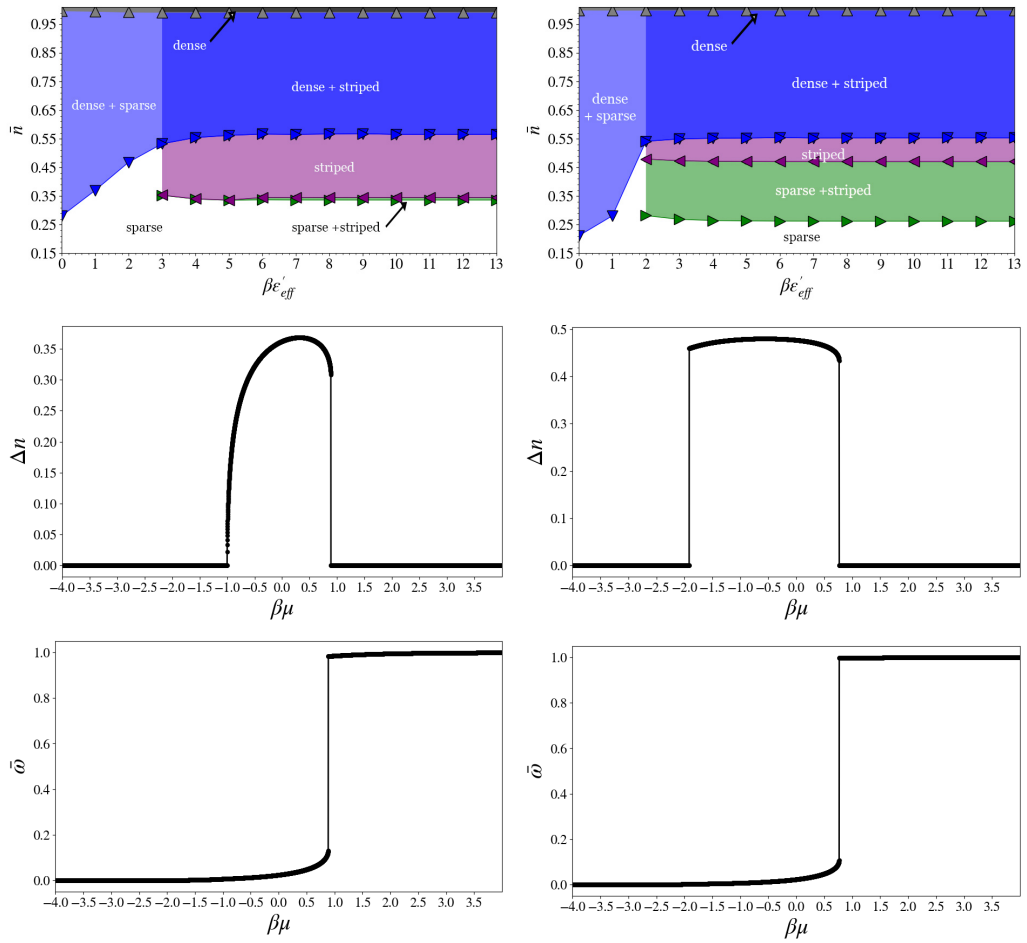

Figure 3.6: Top row: phase diagrams in the $\bar{n}$ vs. $\beta\epsilon'_{\text{eff}}$ plane. Left image corresponds to $K = 3$, right image to $K = 5$. Middle row: cutouts of Δn vs. $\beta\mu$ for $\beta\epsilon'_{\text{eff}} = 4$, with $K = 3$ on the left and $K = 5$ on the right. Bottom row: cutouts of $\bar{\omega}$ vs. $\beta\mu$ for $\beta\epsilon'_{\text{eff}} = 4$, with $K = 3$ on the left and $K = 5$ on the right. For all sub-figures $\beta\gamma = 5$.

the development of striped order. Here, $\bar{\omega}$ changes from near zero to considerable values $\bar{\omega} \gtrsim 0.1$ upon very small changes in $\beta\mu$. Recall that simulations of the fixed-gap model showed exclusively smooth changes in occupancy over a comparable range of conditions.

Simulation results are shown in Figs. 3.7 to 3.9. These heat maps display the three order parameters Δn, $\bar{\omega}$, and $\bar{n}$ values for $K = 4$ and $\gamma = 5$, the same conditions as in the last panel of Fig. 3.3. The phase diagram obtained from simulations strongly resembles that result of mean field theory. Fig. 3.7 exhibits a triangular region of non-zero Δn for similar $\beta\mu$ and ϵ' values. The color changes are gradual on the bottom line, suggesting continuous transitions for low $\beta\mu$. The color progression is starker for more positive $\beta\mu$, suggesting discontinuous transitions there. In Fig. 3.9, $\bar{\omega}$ shows sudden change along a single curve, likely demarcating a first-order double occupancy transition as predicted by mean field theory. The color (value) changes in Fig. 3.8 resemble those of Fig. 3.9 for more positive $\beta\mu$, though the lower half likely reflects the continuous Δn changes in Fig. 3.7 at low $\beta\mu$.

Umbrella sampling provides stronger evidence for the phase behavior predicted by mean field theory. Here we present results of flat histogram sampling for three points in the phase diagrams of Figs. 3.7 to 3.9. This technique in effect removes free energy barriers that hinder transitions between distinct basins of attraction in configuration space. As a result, the relative thermodynamic stabilities of these basins can be quantitatively assessed, and the nature of phase transitions can be carefully evaluated. The three points we examine lie along three distinct phase boundaries in the $(\beta\mu, \beta\epsilon'_{\text{eff}})$ plane.

Fig. 3.10 shows free energy profiles $-\ln P(\bar{\omega})$ at the low-ϵ'_{eff} double occupancy transition. These highly structured profiles shed light on the sampling difficulties faced in straightforward simulations. Due to the long-range nature of interactions mediated by gap fluctuations, each disc acquires or loses double occupancy in a concerted fashion. Interfaces between dense and sparse states therefore run parallel to the discs themselves, and the growth of high-density domains proceeds discretely. The global free energy minima in Fig. 3.10 correspond to uniformly sparse and uniformly dense states. Nearly degenerate local minima at intermediate $\bar{\omega}$ possess an interface between coexisting domains. For isotropic ordering phenomena, the motion of interfaces at coexistence is typically unhindered by barriers, reflecting a great variety of interfacial shapes. Here, however, interfaces between sparse and dense domains can advance only through a barrier-crossing process that interconverts entire discs. These barriers not only slow Monte Carlo sampling; the modu-

lated structure they introduce also complicates the characterization of phase transitions. In this case, it is nonetheless clear from the globally bistable shape of $-\ln P(\bar{\omega})$ that the double occupancy transition is discontinuous.

Continuous striping transitions at low density, which do not centrally involve long-range interactions, need not suffer from such complications. The free energy profile in Fig. 3.12 indeed lacks the discrete structure discussed above. It instead develops a quartically flat shape at the transition, consistent with the predictions of mean field theory at modest K.

High-density striping transitions are most problematic. Because they involve sharp changes in double occupancy, free energy profiles are highly structured. Furthermore, the cost of creating interfaces between striped and doubly occupied domains can be very low. If these patterns lie in register, with the high-density layer of a striped domain adjacent to a doubly occupied domain, the surface tension can very nearly vanish. The free energy profiles in Fig. 3.11 exhibit precisely these features. From these calculations alone, it is very difficult to discern the true thermodynamic ground state. The statistics within individual discs, however, immediately clarify this issue. Thermodynamic bistability of each disc is strongly evident at this transition, strongly implying a discontinuous transition as predicted by mean field theory.

3.8 Discussion

Our calculations suggest mechanical responses of thylakoids present a range of possibilities for protein organization. Recall that the external force f_{ext} in Eq. (3.2) is a means to tune ϵ'_{eff}, the effective steric repulsion. The quantities $\epsilon'(\theta_0)$ (baseline steric repulsion), k (membrane stiffness), and f (proportionality constant in Eq. (3.1)) are fixed, so the only parameter that may modify ϵ'_{eff} is f_{ext}. While in our previous model ϵ'_{eff} was considered constant, the inclusion of this force allows ϵ'_{eff} to change. In changing ϵ'_{eff} we can manipulate lumenal gap thicknesses.

To concretely consider shifts in ϵ'_{eff}, let us revisit the $\beta\mu$ and $\beta\epsilon'_{\text{eff}}$ phase diagrams of Fig. 3.3. (In the previous chapter we discuss at length the physiological inspiration and implications of the parameters K, $\beta\epsilon'_{\text{eff}}$, and $\beta\mu$; here we concern ourselves primarily with the consequences of the sampled choices for $\beta\epsilon'_{\text{eff}}$, $\beta\mu$, and γ.) Changing force at fixed $\beta\mu$ can cause sudden changes in density (top left panel), or induce/disrupt stripe patterns (top right and bottom panels for $\beta\epsilon'_{\text{eff}} > 6$), or in some cases both at the same

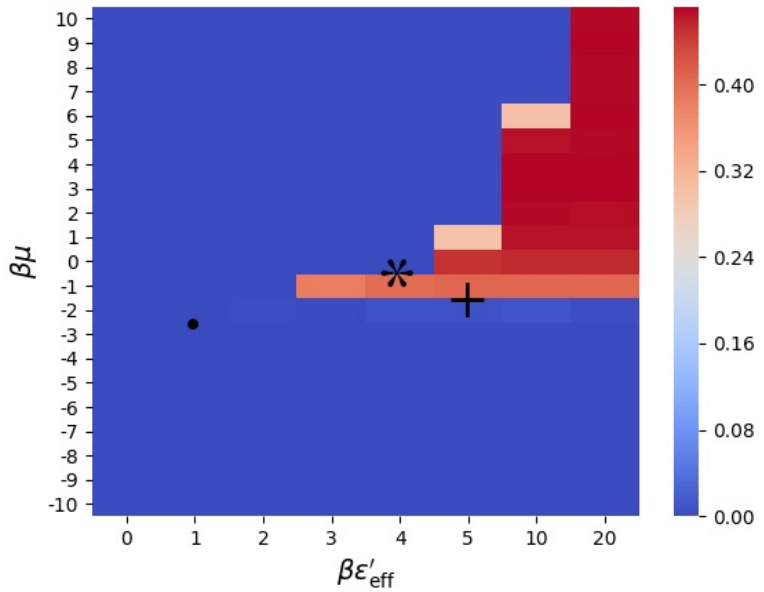

Figure 3.7: Heat map in the $\beta\mu$ vs. $\beta\epsilon'_{\text{eff}}$ plane for average $|\Delta n|$ values. Data obtained for $K = 4$, $\beta\gamma = 5$, via Monte Carlo simulations. Dot, asterisk, and cross indicate points to be discussed in Figs. 3.10 to 3.12.

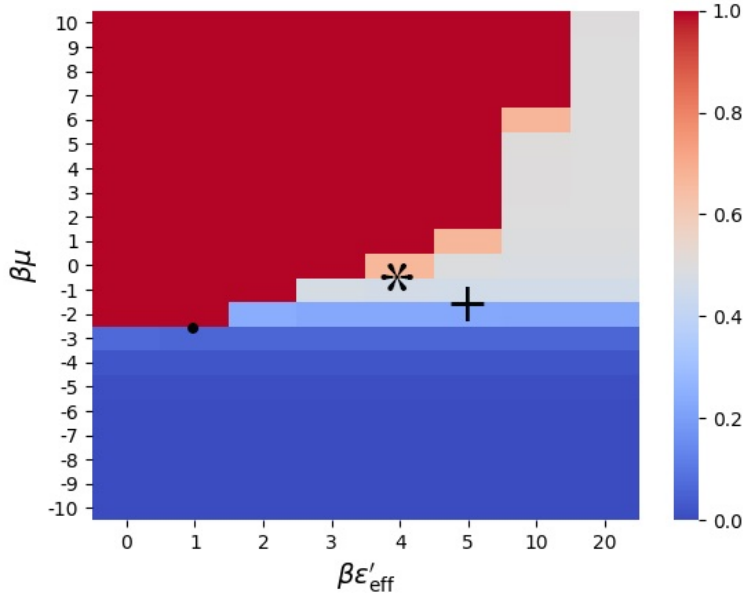

Figure 3.8: Heat map in the $\beta\mu$ vs. $\beta\epsilon'_{\text{eff}}$ plane for $\bar{n}$ values. Data obtained for $K = 4$, $\beta\gamma = 5$, via Monte Carlo simulations. Dot, asterisk, and cross indicate points to be discussed in Figs. 3.10 to 3.12.

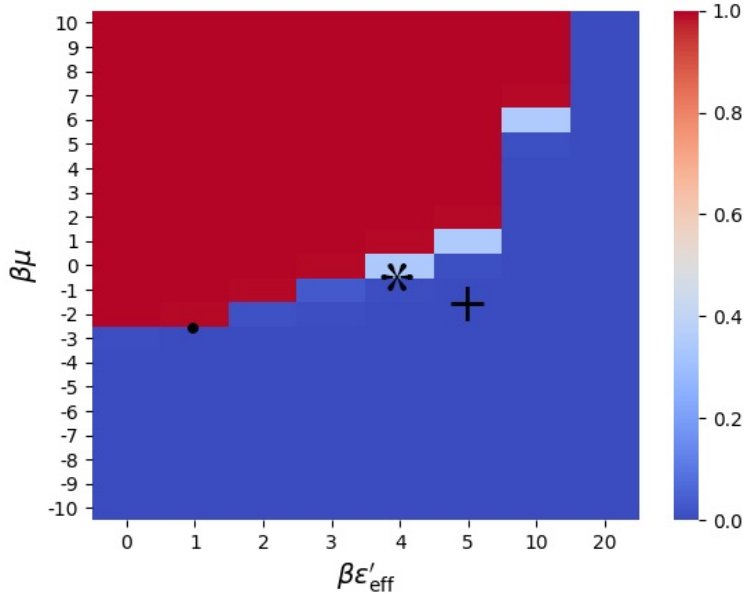

Figure 3.9: Heat map in the $\beta\mu$ vs. $\beta\epsilon'_{\text{eff}}$ plane for $\bar{\omega}$ values. Data obtained for $K = 4$, $\beta\gamma = 5$, via Monte Carlo simulations. Dot, asterisk, and cross indicate points to be discussed in Figs. 3.10 to 3.12.

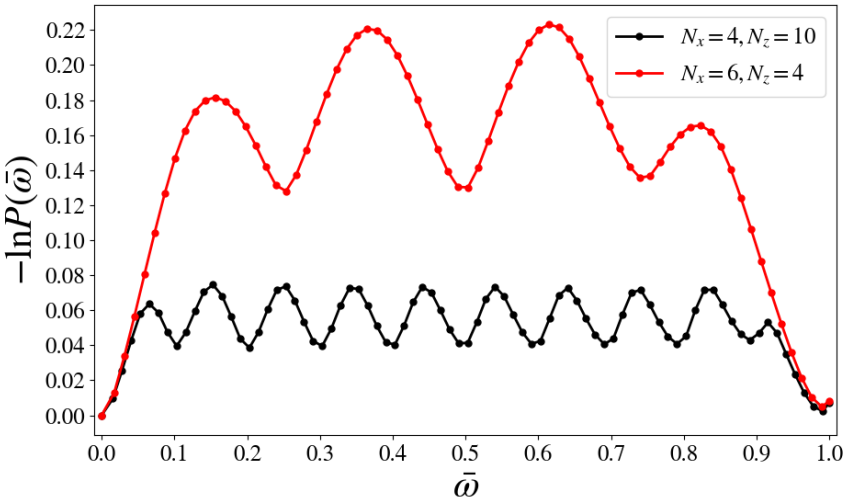

Figure 3.10: Free energy as a function of $\bar{\omega}$ for $\beta\gamma = 5$, $K = 4$, $\beta\epsilon'_{\text{eff}} = 1$, and $\beta\mu = -2.67$ for two different system sizes. Represented by the dot in Figs. 3.7 to 3.9. Data by PLG.

time (bottom panel for $\beta\epsilon'_{\text{eff}} > 3$). These possibilities are similar for most K values. At fixed $\beta\mu$, changing force is unlikely to encounter the low-density stripe phase boundary, which is nearly parallel to the $\beta\epsilon'_{\text{eff}}$ axis. Fixed density, however, corresponds to a curve in this plane that is likely monotonic but need not be straight. Applying force at fixed density could therefore traverse a different set or sequence of phase boundaries.

Considering that larger ϵ'_{eff} corresponds to thinner lumenal gaps, these data suggest the salient feature of thicker lumenal gaps is the density of protein rather than any particular structure. For thinner lumenal gaps (larger ϵ'_{eff}), the competition of stacking attraction (K) and lumenal steric repulsion (ϵ'_{eff}) becomes relevant (*i.e.*, K and $\beta\epsilon'_{\text{eff}}$ have the same order of magnitude), making modulated phases possible and energetically favorable. When $K >> \beta\epsilon'_{\text{eff}}$, dense states form; when $K << \beta\epsilon'_{\text{eff}}$, the system's maximally dense phase is the striped phase. This is loosely consistent with the understanding that large ϵ'_{eff} (thinner gaps) correspond to dark to low light conditions, where stacking is strong, and small ϵ'_{eff} (thicker gaps) to high light conditions, where stacking is disrupted by a number of factors.

The parameter γ represents how much the granum has the capacity to

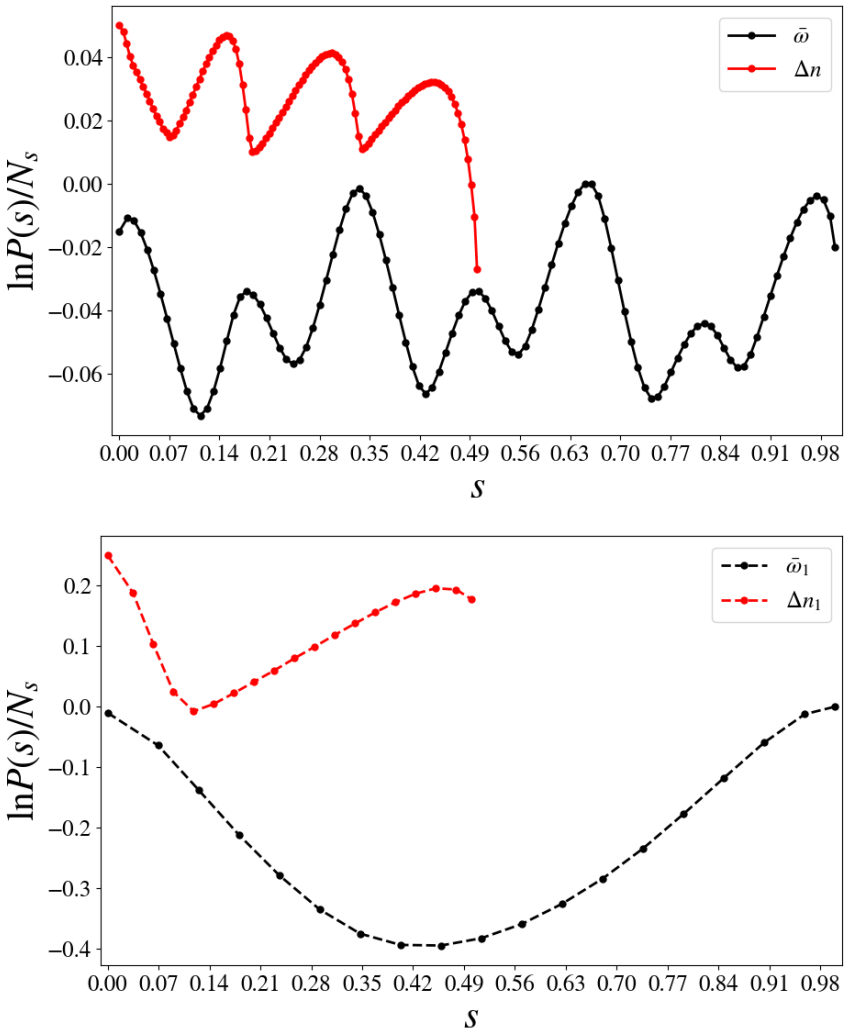

Figure 3.11: Probability distributions for order parameters $\bar{\omega}$ (black curve) and Δn (red curve) at $\beta\gamma = 5$, $K = 4$, $\beta\epsilon'_{\text{eff}} = 4$, and $\beta\mu = -0.44$. Represented by the asterisk in Figs. 3.7 to 3.9. Dashed lines mark distributions in which order parameters were averaged over only one layer, and solid lines indicate distributions for order parameters averaged over the entire system. Data by PLG.

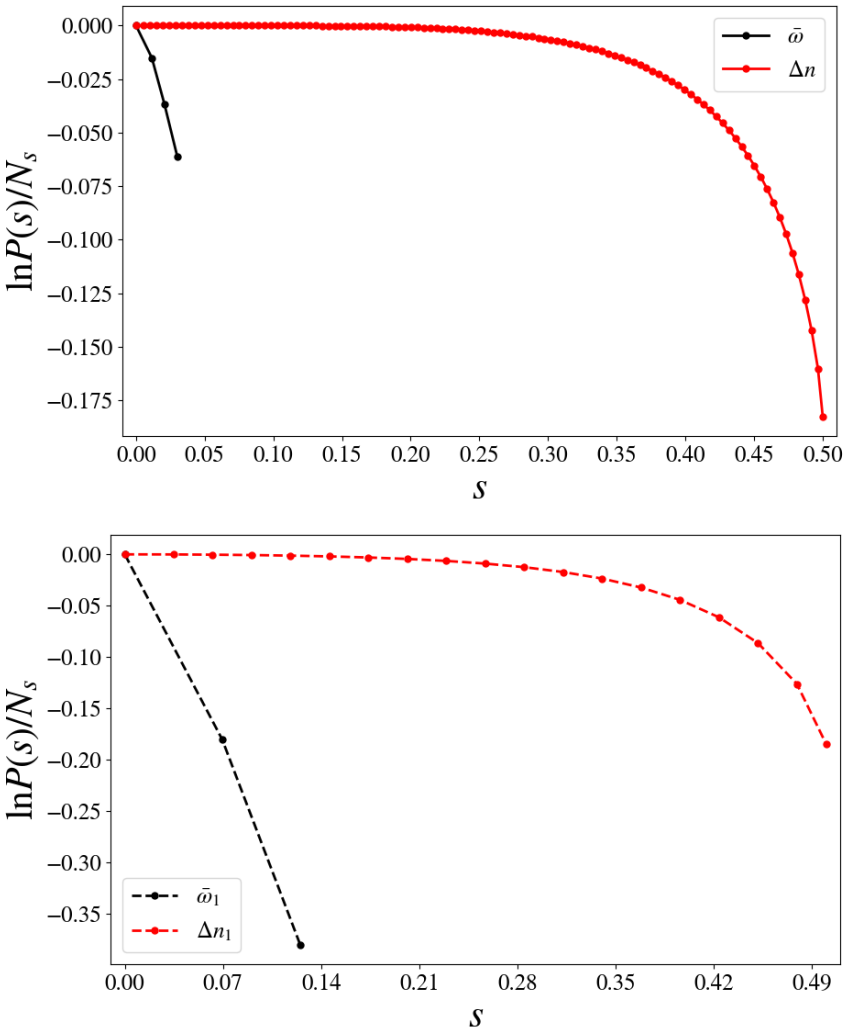

Figure 3.12: Probability distributions for order parameters $\bar{\omega}$ (black curve) and Δn (red curve) at $\beta\gamma = 5$, $K = 4$, $\beta\epsilon'_{\text{eff}} = 5$, and $\beta\mu = -1.65$. Represented by the cross in Figs. 3.7 to 3.9. Dashed lines mark distributions in which order parameters were averaged over only one layer, and solid lines indicate distributions for order parameters averaged over the entire system. Data by PLG.

vary lumenal gap thicknesses across the stack of thylakoids. For larger γ the stack has more variation in thylakoid dimensions, and as such we expect the system to be more pliant to changing conditions.

It is well known that illumination changes beget reorganization of thylakoid membranes. These results suggest that mechanical force application may have similar effects on protein spatial patterning, as external forces allow one to move across the $(\beta\mu, \beta\epsilon'_{\text{eff}})$ plane. How said forces could affect other characteristics (*e.g.*, pH gradients or phosphorylation states) of illumination states is unclear. If we assume that force application can initiate a chain of events that result in granal protein reorganization, then mechanical manipulation of thylakoid membranes would be akin to changing illumination. That said, the discontinuous nature of some of these transitions suggests force application could induce more dramatic changes than gradual light acclimation. The results of this chapter depict equilibrium phase behavior; as such, we discuss static, not dynamic properties, and therefore will refrain from commenting on time scales for protein redistribution.

Stable thermodynamic phases of the fluctuating-gap model have the same symmetries as those of the fixed-gap model, and are distinguished in much the same way. We therefore associate them with physiological states as described in Chapter 2. In particular, the striped ordered phase is characterized by coherent stacking, which is in turn promoted by tightly layered membranes. The most plausible natural conditions in which this state could be stable involve little or no light intensity. Other light conditions more likely favor the dense or sparse unstructured states.

The limitations of this model are largely the same as those of the fixed-gap model. Both models are sparse in microscopic detail. They do not distinguish among the associating protein species in photosynthetic membranes. While this fluctuating-gap model accounts for fluctuations in lumenal gap thickness, the gap thickness only fluctuates on a per-thylakoid basis, and therefore does not account for local shape fluctuations of the lipid bilayers. Given the typically high protein density of photosynthetic membranes, these membranes are largely depleted of lipids and therefore are expected to be mostly rigid in the central region of grana. Unless these unresolved features generate long-range correlations of their own, they are unlikely to alter the basic ordering scenario we have described. Such details are instead important in setting the parameters of a coarse-grained representation like Eq. (3.7). The finite size of actual grana stacks will round off sharp transitions and limit divergences, but natural photosynthetic membranes should be large enough

to exhibit micron-scale cooperativity in protein rearrangements.

Recent progress in tomography and live imaging of plant cells and chloroplasts provide new avenues for direct observation of changing morphology in photosynthetic systems and corroborate findings of mechanics-based experiments. [13] While the resolution is not fine enough to distinguish individual proteins or the details of their clustering, with techniques like three-dimensional structured illumination microscopy (3D-SIM), differences in membrane structure between high light intensity from normal conditions are readily observed. [69, 70, 71] Moreover, due to their application to entire cells or chloroplasts, with improved resolution, entire grana – or even collections of grana – could be visualized. Tomography has already been applied to photosynthetic membranes, though only in two extremes: to capture details relevant for cyclic electron flow, [72] or to document topology of grana. [73] It remains to be seen if tomography could be used to resolve protein complexes while simultaneously probing grana ultra-structure. We hope that, using these techniques or others mentioned earlier in this chapter, photosynthesis research leads to both higher resolution measurements of protein spatial organization and, ideally, responses to mechanical forces.

3.9 Conclusion

The mean field analysis and Monte Carlo sampling results we have presented demonstrates that mechanical forces can dramatically alter conditions favoring striped, modulated order of protein density. In essence, applying mechanical forces in this model corresponds to shifting the steric repulsion strength in the fixed-gap model. Adding fluctuating lumenal gap thickness enriches the phase behavior. By decreasing the stiffness of membranes, the system's lumenal gap thickness can fluctuate more substantially, disrupting ordering and allowing the thylakoid to accommodate proteins at higher density. Conversely, stiffening the membranes leads towards the limit of the fixed-gap model detailed in the previous chapter. In conclusion, compared to the fixed-gap model, the range of stability of modulated order is reduced, but the scenarios for entering and leaving the ordered phase are more complicated. These transitions are more directly connected to experimental control variables.

For weak stacking coupling, abrupt, discontinuous transitions from sparse to dense unstructured phase occur. When striping transitions are possible,

the character of transitions depends greatly on the density of the system. At high density, striping and occupancy transitions occur simultaneously and discontinuously for moderate to large stacking strength. At low density, the striping transition is continuous for weak to moderate stacking strength, and it becomes discontinuous at larger stacking strength. The discontinuous striping transitions are accompanied by weakly discontinuous changes in occupancy.

The various possibilities for transitions suggest applying mechanical forces may have a range of effects on long-ranged protein organization in grana. Compressive or expansive forces may lead to sudden and dramatic changes in protein population and patterning. We suggest that monitoring and modifying lumenal gap thickness may have effects on protein distributions akin to changing illumination.

Chapter 4

Conclusion

4.1 Implications

Minimalistic physics can, at least in an abstract way, illuminate underlying driving forces in light and physiological conditions in plants. A mathematical approach such as those described here could be used to predict possible regimes of order and disorder in higher plants. More importantly, the parameters of our models could be translated into descriptors of high light, low light, dark, state transition, and other conditions, so that we can develop a language of mesoscale organization in photosynthetic membranes. Both sets of models suggest an array of states characterized by protein density, lumenal gap thickness, and protein ordering. The presence of both continuous and discontinuous transitions between ordered and disordered states imply that, under certain circumstances, fluctuations in density or gap thickness may facilitate transitions between states, but that in some cases abrupt changes in state may occur instead.

Given the extreme physiological states suggested by the sparse disordered and striped phases, these phases may not be physically possible in grana. That said, they may represent regimes of alignment in protein distribution across thylakoids within a granum. The striped phase could merely depict a state of strong, consistent stacking throughout a granum; for this reason we suggest it corresponds to dark to low light conditions. Alternatively, vertical alignment of laterally ordered domains throughout a granum may be a possible *in vivo* manifestation of the striped phase. The dense and sparse unstructured phases indicate relative density of protein in the grana core,

as well as imply an inherent lack of order or alignment, regardless of the interpretation chosen here.

Results of the fluctuating-gap model may inspire further mechanical experiments with atomic force microscopy techniques applied to thylakoid membranes; we discuss possibilities for experiments below.

Tuning some parameters could permit these models to be more widely applicable to other organisms, such as algae and cyanobacteria. Broadly speaking, these organisms have less hierarchical architecture than higher plants do, so I would expect the striped phase to be less accessible in these systems. While this is due to their smaller or non-existent grana (thylakoids or prothylakoids are present; the grana structure is not), in the cast of our model this would arise as weaker stacking (smaller K) or more flexible membranes (higher γ).

4.2 Future Directions

On the theoretical side, future directions largely involve making the model more specific and more directly empirically inspired.

Further extension of the fluctuating-gap model could involve explicitly coupling multiple grana in a manner inspired by Ref. [12]. This would remove some of the mystery of the stroma lamellae and lead to a more precise understanding of chemical potential. Similarly, non-periodic boundary conditions could specify how the margins, or edges, of thylakoids affect protein distribution and mass exchange with the stroma lamellae.

Helfrich-type terms [85] could be included in the Hamiltonian to describe membrane plasticity not only as a function of lumenal gap thickness, but also material properties intrinsic to photosynthetic membrane lipids. Some suspect CURT proteins [15] and even carotenoids [74, 75] may influence membrane shape and fluidity, so this very much is an area requiring further experimental study.

The abstracted ideas brought forth in these models could be extended to a particle-based model, such as the Schneider-Geissler coarse-grained particle model. [8, 9] This may be the simplest means of incorporating more protein species-specific detail. Moreover, a model such as theirs could be extended to accommodate more than two membrane layers and to incorporate variable lumenal steric repulsion. This model could be simulated via Metropolis Monte Carlo techniques, as those used here, or possibly Langevin dynamics

so as to capture dynamic behavior of this system. (All the results here are static phenomenology; indeed those of Refs. [8, 9, 10] are, too.)

On the empirical side, as outlined in Chapter 2, we hope this theoretical work inspires mechanical, force-based measurements of thylakoid membranes to stimuli. We envision applying compressing or pulling forces to thylakoids or grana and measuring/imaging subsequent redistribution of protein for a number of time delays after the force application, while holding light intensity and wavelength constant. It would be interesting to see how these reorganizations compare to changing light conditions or altering salt concentration (or pH). More than likely such experiments would involve AFM-based measurements.

We also anticipate advances in live cell imaging and other imaging techniques, so as to observe membranes under changing physiological and illumination states; see Sec. 3.3 and Sec. 3.8 for details on these methods. We hope said advances include not only increased resolution, but also the ability to study larger samples like a granum comprising a few thylakoids.

4.3 Broader Impacts

As mentioned in the introduction to this dissertation, reasons for investigating principles underlying photosynthetic architecture and function range in application. As the effects of climate change become more frequent and dramatic, we continue to be reminded that we humans must not only seek, but also find solutions for how to adapt to a rapidly changing world. Engineering crops will be essential for sustaining nourishing crops for growing populations, new biofuels will need to be tried and tested, and clean energy will need to scale up dramatically. Over time scales much longer than our lifespans, plants will continue to adapt and evolve; perhaps we can learn to harness some of their energy-processing power for ourselves. While the work in this dissertation is quite focused in scope, I hope it contributes to the human knowledge base that may lead to advancements necessary to prolong the existence of humanity and to curtail anthropogenic changes to the planet Earth.

Chapter 5

Appendices

5.1 Chapter 2 Appendix

5.1.1 Methods: Monte Carlo

Simulation specifications

Phase transitions were determined via umbrella sampling, a form of biased MC simulations. The bias added to the Hamiltonian energy was a harmonic potential $\frac{1}{2}k(\langle\Delta n\rangle - \Delta n_{target})^2$ with a spring constant k of 10,000 k_BT. Simulations were run for (2 to) 3 million MC sweeps, saving Δn and $\bar{n}$ data every 100 sweeps. The bias targets ranged from $\Delta n_{target} = -0.5$ to $\Delta n_{target} = 0.5$ for a total of 51 distinct Δn_{target} values. With these data, free energy profiles were constructed via the WHAM method. [76]

5.1.2 Binder cumulants

We computed Binder cumulants for the thylakoid striping transition in order to verify its Ising universality classification. We specifically consider [77, 78]

$$U_4^* = 1 - \frac{\langle(\Delta n)^4\rangle}{3\langle(\Delta n)^2\rangle^2} \tag{5.1}$$

Fig. 5.1 shows U_4^* as a function of $\beta\mu$ for $K = 5.25$ and $\beta\epsilon' = 1$, over a range that spans the ordering transition. The interval in which the free energy $F(\Delta n)$ changes convexity is also marked. Values of U_4^* in this interval lie

near that expected for the three-dimensional cubic Ising model universality class. [79]

Fig. 5.2 shows analogous results for $K = 3.5$ and $\beta\epsilon' = 20$.

Evidence for first-order transitions in simulation

The enhanced sampling methods used to obtain data in Fig. 5.1.2 utilized the flat histogram method. [80] Simulations were performed by PLG.

The plots in Fig. 5.1.2 provide a glimpse into how the order of transitions changes in simulation for increased K. We present the data in terms of three order parameters, $\bar{n}$, Δn, and p_{11}. The first two have been discussed at length in the main text, while p_{11} has not. The latter is the probability of two sites, on either side of the same disc, being occupied; these probabilities are discussed in the derivation of Eq. (2.7).

As K increases (*i.e.*, moving from left to right in the columns of Fig. 5.1.2, the full-system distributions (top row of plots) of all order parameters flatten. These changes are accompanied by emerging bimodality in all order parameter distributions on the individual-disc level (bottom row). While the flattening of system-wide distributions suggests a generic phase transition has begun, the development of bimodal distributions for a subset of the system implies an interface between two phases has formed, creating portions of the system belonging to either (coexisting) phase. Since this character develops prominently in the rightmost column for $K = 7$, we believe the striping transition takes on first-order characteristics between $K = 6$ and $K = 7$.

5.1.3 Methods: Mean field theory

Mean field phase diagrams were obtained by numerically minimizing the free energy in Eq. (2.6) or (2.7) of the main text. We found it most efficient to do so by iterating self-consistent equations that determine local free energy minima. Here we provide these self-consistent equations, which result from differentiating F_{MF}, and detail other aspects of our mean field analysis.

Self-consistent equations for the hard constraint limit

The hard constraint MFT average order parameter is

$$\Delta n = \frac{1}{2} \frac{e^{\beta\mu}(e^{K\bar{n}^{(1)}} - e^{K\bar{n}^{(2)}})}{1 + e^{\beta\mu}e^{K\bar{n}^{(1)}} + e^{\beta\mu}e^{K\bar{n}^{(2)}}} \tag{5.2}$$

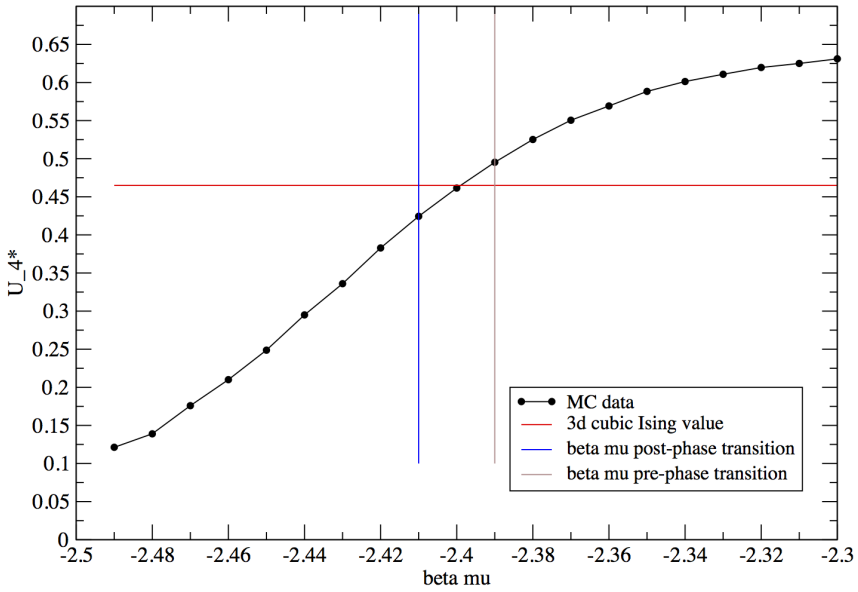

Figure 5.1: Binder cumulant U_4^* as a function $\beta\mu$ for $J = 0.675k_BT$, $\epsilon = 2.55k_BT$, and $\epsilon' = 1k_BT$. The horizontal dashed line represents the three-dimensional cubic Ising universality value of 0.465 The horizontal red line indicates the universal value $U_4^* = 0.465$ corresponding to the three-dimensional Ising model on a cubic lattice. Vertical lines bracket the range of $\beta\mu$ over which $F(\Delta n)$ changes convexity.

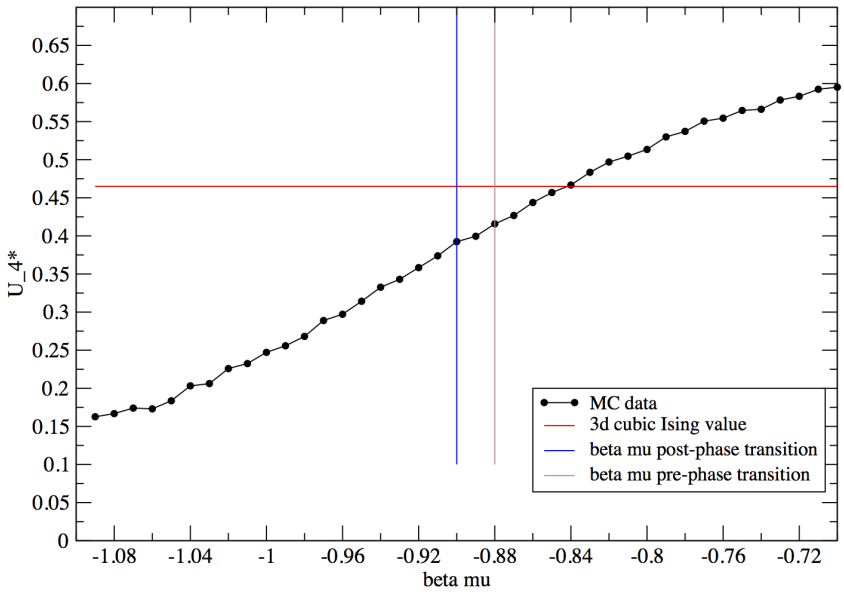

Figure 5.2: Binder cumulants for $\beta\mu$ at and near transition for $J = 0.45k_BT$, $\epsilon = 1.7k_BT$, and $\epsilon' = 20k_BT$. The horizontal dashed line represents the three-dimensional cubic Ising universality value of 0.465. Vertical lines bracket the range of $\beta\mu$ over which $F(\Delta n)$ changes convexity.

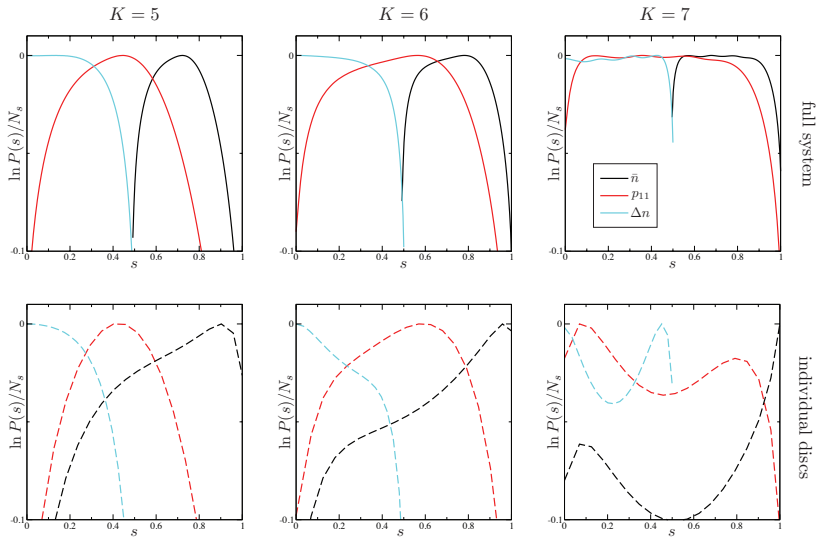

Figure 5.3: Log probability distributions for order parameters $\bar{n}$, Δn, and p_{11}, at both the full system level and the individual disc level. The development of shoulders to full bimodality that occurs as K is increased (moving from left to right in the figure columns) indicates discontinuous transitions occur somewhere between $K = 6$ and $K = 7$.

where $\bar{n}^{(i)}$ refers to the average density in the ith layer. Mutatis mutandis for $\bar{n}^{(2)}$. The average density is

$$\bar{n} = \frac{1}{2}\frac{e^{\beta\mu}(e^{K\bar{n}^{(1)}} + e^{K\bar{n}^{(2)}})}{1 + e^{\beta\mu}e^{K\bar{n}^{(1)}} + e^{\beta\mu}e^{K\bar{n}^{(2)}}} \tag{5.3}$$

Onset of first-order transitions for the hard constraint limit

We identify the onset of discontinuous transitions by posing the question: As the free energy extremum at $\bar{n} = 1/K$ and $\Delta n = 0$ loses local stability, do lower-lying minima of $F_{\rm MF}$ exist? Near the onset we assume that such minima reside at very small Δn and at $\bar{n}$ very close to $1/K$; for a given value of $\bar{n}$, these minima Δn^* satisfy

$$\Delta n^{*2} = 3\bar{n}^3\left(K - \frac{1}{\bar{n}}\right) \tag{5.4}$$

where we have neglected terms of order Δn^4.

Setting $\bar{n} = 1/K + \eta$, Eq. 5.4 gives

$$\Delta n^* = \pm\sqrt{\frac{3}{K}\eta} + O(\eta^{3/2}) \tag{5.5}$$

To lowest order in η, the mean field free energy $F_{\rm MF}(\bar{n}, \Delta n)$ at the putative satellite minima can then be written

$$\begin{aligned}\frac{2\beta}{N}F_{\rm MF}\left(1/K + \eta, \pm\sqrt{\frac{3}{K}\eta}\right) &= \frac{2\beta}{N}F_{\rm MF}\left(1/K, 0\right) \\ &+ \left(-3K + \frac{4K}{K-2}\right)\eta^2\end{aligned} \tag{5.6}$$

For $K > 10/3$, this free energy lies below that of the critical state at $\bar{n} = 1/K$ and $\Delta n = 0$. In other words, symmetry breaking occurs discontinuously, before the symmetric state becomes permissive of macroscopic fluctuations.

Self-consistent equations for soft steric repulsion

Minimizing the free energy Eq. (2.7) with respect to p_{10}, p_{01}, p_{11}, and $p_{00} = 1 - (p_{10} + p_{01} + p_{11})$ gives nonlinear expressions for the mean density in alternating layers,

$$n_1 = p_{10} + p_{11} = \frac{1}{q}(ae^{Kn_1} + \delta a^2 e^{K(n_1+n_2)}), \tag{5.7}$$

and

$$n_2 = p_{01} + p_{11} = \frac{1}{q}(ae^{Kn_2} + \delta a^2 e^{K(n_1+n_2)}), \tag{5.8}$$

where $a = e^{\beta\mu}$, $\delta = e^{-\beta\epsilon'}$, and

$$q = 1 + a(e^{Kn_1} + e^{Kn_2}) + \delta a^2 e^{K(n_1+n_2)}. \tag{5.9}$$

Iteration of these expressions converges rapidly to local minima of $F_{\rm MF}$. From these solutions, our primary order parameters are computed simply from $\bar{n} = (n_1 + n_2)/2$, and $\Delta n = (n_1 - n_2)/2$.

Continuous transitions for soft steric repulsion

For finite ϵ', the extremum of $F_{\rm MF}$ at $\Delta n = 0$ becomes locally unstable when

$$\bar{n} = \frac{1}{2} \pm \frac{1}{2K}\sqrt{(K-2)^2 - 4\delta}, \tag{5.10}$$

defining possible continuous transitions in the $(K, \bar{n})$ plane. Fig. 5.4 shows both lines of solutions in the $(K, \beta\mu)$ plane, for several values of ϵ'. In each case the two lines cross at an attraction strength $K_{\rm cross}(\epsilon')$. For $\beta\epsilon' \geq 2$, $K_{\rm cross}$ lies outside the range of this plot.

Continuous transitions predicted for $K > K_{\rm cross}$ violate a fundamental thermodynamic requirement of stability. Specifically, the solution with higher density $\bar{n}$ occurs at a lower chemical potential than the low-density solution, implying a negative compressibility. Although these solutions represent local free energy minima, they cannot be global minima. Indeed, numerical minimization of $F_{\rm MF}$ identifies lower-lying minima in all cases.

Self-consistent equations for soft steric repulsion

Minimizing the mean field free energy for finite ϵ' yields nonlinear equations for the average layer densities:

$$\langle n_i \rangle = \frac{1}{q}(ae^{Kn_i} + \delta a^2 e^{2Kn}), \tag{5.11}$$

In terms of n and Δn,

$$n = \frac{1}{2q}\left[ae^{Kn}(e^{K\Delta n} + e^{-K\Delta n}) + 2a^2 e^{2Kn}\delta\right] \tag{5.12}$$

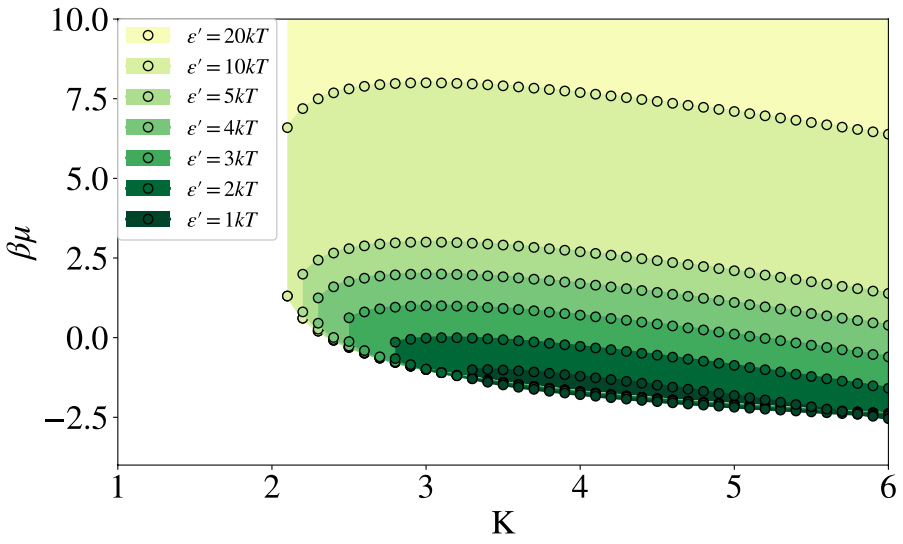

Figure 5.4: Soft constraint model $\beta\mu$ vs. K phase diagram, continuous mean field transitions according to Eq. (2.8). Shaded region indicates the striped phase.

$$\Delta n = \frac{1}{2q}\left[ae^{Kn}(e^{K\Delta n} - e^{-K\Delta n})\right] \tag{5.13}$$

where $a = e^{\beta\mu}$, $\delta = e^{-\beta\epsilon'}$, $n = \frac{1}{2}(n_1 + n_2)$, and $\Delta n = \frac{1}{2}(n_1 - n_2)$.

Solving self-consistent equations

Iterating the self-consistent equations (5.12) and (5.13) converges readily to local extrema of the mean field free energy. After 10^6 steps, additional iteration changes values of n_1 and n_2 by less than 10^{-12}.

Under many conditions, however, this free energy surface exhibits three or more distinct minima. The end result of iteration thus depends on initial values of n_1 and n_2. We considered five different (n_1, n_2) pairs, namely (0.6, 0.4), (0.1, 0.1), (0.9, 0.9), (0.9, 0.1), and (0.2, 0.1). For each set of conditions, we then select the self-consistent solution with lowest free energy.

A resulting value of $|n_1 - n_2|$ greater than 10^{-9} was taken to signify thermodynamic stability of the ordered phase.

5.1.4 Methods: Bethe-Peierls approximation

One-cluster diagram

Our site cluster, depicted in Fig. 5.5, encompasses two thylakoid discs, so as to capture one instance of the striped motif in the striped phase.

One-cluster expressions

The cluster Hamiltonian is

$$\begin{aligned} H = &-\mu(n_{0A} + n_{0B}) - J\sum_{i=1}^{4}(n_{0A}n_{iA} + n_{0B}n_{iB}) \\ &- \epsilon(n_{0A}n_{5A} + n_{0B}n_{5B}) + \epsilon' n_{0A}n_{0B} \\ &- \mu_A\sum_{i=1}^{4} n_{iA} - \mu_B\sum_{i=1}^{4} n_{iB} - \mu'_A n_{5A} - \mu'_B n_{5B} \end{aligned} \tag{5.14}$$

where A and B denote different stripes.

In a BP ansatz, instead of solving for average densities, one solves for effective fields; these are given by μ_A, μ_B, μ'_A, and μ'_B. There are *four*

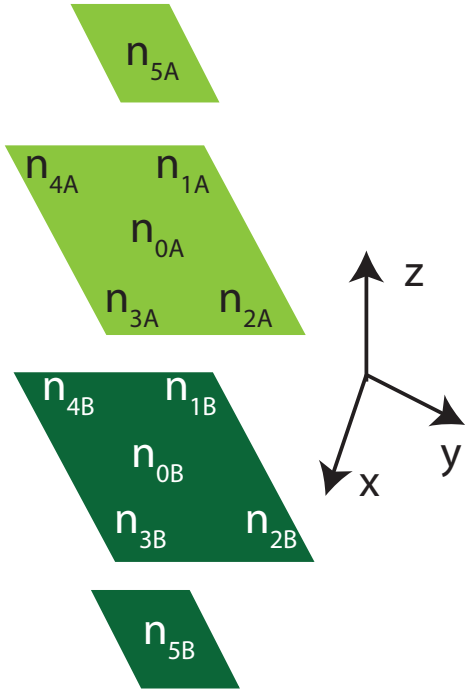

Figure 5.5: Bethe-Peierls cluster schematic. n_{0X} is the central site, and all others are neighboring sites. Dark-colored sites denote sites in a densely populated stripe, and light-colored sites represent sites in a sparsely populated stripe.

fields because sites interfacing with a stripe of the opposite type experience a different field than those surrounded by like sites.

If we take $J = \epsilon$, then $\mu'_k = \mu_k$. With this in mind, we write the partition function. First, below are some important variable assignments:

$$\begin{aligned}
\mu_A = \bar{\mu} + \Delta\mu, \mu_B = \bar{\mu} - \Delta\mu \\
z = e^{\beta\mu}, z_A = e^{\beta\mu_A}, z_B = e^{\beta\mu_B} \\
\bar{z} = e^{\beta\bar{\mu}}, \delta = e^{-\beta\epsilon'}, c = e^{K}
\end{aligned}$$

Taking the standard derivatives of Eq. (5.15), the average densities are

Eqs. (5.16) and (5.16). Note that there are two average densities for each stripe, with n_{0x} as the central sites and the others its neighboring sites.

$$\begin{aligned} Q &= \sum_{n_{0A},n_{0B}} z^{n_{0A}+n_{0B}}\delta^{n_{0A}n_{0B}}\left(1+z_Ae^{Kn_{0A}}\right)^5\left(1+z_Be^{Kn_{0B}}\right)^5 \\ &= \left(1+\bar{z}e^{\beta\Delta\mu}\right)^5\left(1+\bar{z}e^{-\beta\Delta\mu}\right)^5 \\ &+ z\left(1+c\bar{z}e^{\beta\Delta\mu}\right)^5\left(1+\bar{z}e^{-\beta\Delta\mu}\right)^5 \\ &+ z\left(1+\bar{z}e^{\beta\Delta\mu}\right)^5\left(1+c\bar{z}e^{-\beta\Delta\mu}\right)^5 \\ &+ z^2\delta\left(1+c\bar{z}e^{\beta\Delta\mu}\right)^5\left(1+c\bar{z}e^{-\beta\Delta\mu}\right)^5 \end{aligned} \tag{5.15}$$

$$\begin{aligned} \langle n_{0A}\rangle = \frac{1}{Q}\left(1+c\bar{z}e^{\beta\Delta\mu}\right)^5 z\Bigg[&\left(1+\bar{z}e^{-\beta\Delta\mu}\right)^5 \\ &+ z\delta\left(1+c\bar{z}e^{-\beta\Delta\mu}\right)^5\Bigg] \end{aligned} \tag{5.16}$$

$$\begin{aligned} \langle n_A\rangle &= \frac{1}{5Q}\frac{\partial Q}{\partial\beta\mu_A} = \frac{z_A}{5Q}\frac{\partial Q}{\partial z_A} \\ &= \frac{\bar{z}e^{\beta\Delta\mu}}{Q}\Bigg\{\left(1+\bar{z}e^{\beta\Delta\mu}\right)^4\Bigg[\left(1+\bar{z}e^{-\beta\Delta\mu}\right)^5 + z\Big(1 \\ &+ c\bar{z}e^{-\beta\Delta\mu}\Big)^5\Bigg] + cz\left(1+c\bar{z}e^{\beta\Delta\mu}\right)^4\Bigg[\left(1+\bar{z}e^{-\beta\Delta\mu}\right)^5 \\ &+ z\delta\left(1+c\bar{z}e^{-\beta\Delta\mu}\right)^5\Bigg]\Bigg\} \end{aligned} \tag{5.17}$$

Here we have replaced μ_A and μ_B with $\bar{\mu}+\Delta\mu$ and $\bar{\mu}-\Delta\mu$, as this formulation more intuitively allows one to discuss the fields in terms of an average field and fluctuations from it. The astute reader will notice the factor of 5 in Eq. (5.17) – this is the number of nearest neighbors in the

same lattice A. In general, this number would be $2d-1$, where d is the total dimensionality of the system; other factors in Eq. (5.17) may change with different d. The difference between $\langle n_{iA}\rangle$ and $\langle n_{iB}\rangle$ simply involves replacing μ_A with μ_B and vice versa; for this reason, $\langle n_{iB}\rangle$ expressions are not shown here.

Since we have two unknowns, $\bar{\mu}$ and $\Delta\mu$, instead of solving one self-consistency expression as for mean field theory, one must solve a system of equations. The system is Eqs. (5.18) or (5.19). The system was initialized for both small and large $\delta\mu$ and for initial μ_i large and small. The tolerance for self-consistency was 10^{-12}, and the maximum number of iterations was 1 million. The transition was determined by finding Δn differences larger than 10^{-9} between consecutive $\beta\mu$ values for a given K.

$$\begin{aligned} \langle n_{0A}\rangle &= \langle n_A\rangle \\ \langle n_{0B}\rangle &= \langle n_B\rangle \end{aligned} \tag{5.18}$$

$$\begin{aligned} \langle \Delta n_0\rangle - \langle \Delta n\rangle &= 0 \\ \langle \bar{n_0}\rangle + \langle \bar{n}\rangle &= 0 \end{aligned} \tag{5.19}$$

where $\Delta n_i = \frac{1}{2}(n_A - n_B)$ and $\bar{n_i} = \frac{1}{2}(n_A + n_B)$.

Phase diagrams

Here we present Bethe-Peierls phase diagrams, in both the $\beta\mu$ vs. K and $\bar{n}$ vs. K planes. Figs. 5.6 and 5.7 show a larger range of K values than we presented for two-site mean field theories. Only at these larger values of K are signs of discontinuous ordering apparent at the BP level of mean field theory.

Continuous BP transitions can be determined by linearizing the self-consistent equations. The resulting equations, which are polynomial in $\bar{z}$, are amenable to numerical root finding methods. Continuous transitions can also be located by initializing the nonlinear self-consistent iteration appropriately. These continuous transitions, plotted in Figs. 5.7 and 5.9 (on different scales), show the same unphysical crossing behavior found with the two-site approach, though this crossing occurs at a larger K value than in the previous approach.

Self-consistent solutions obtained with a different initialization are plotted in Fig. 5.6 over a wide range of K. At small K they coincide with the continuous transitions described above, as emphasized in Fig. 5.8, which shows only the range of K accessible in simulations. Limited to the domain $1 < K < 6$, this plot is essentially identical to the continuous case Fig. 5.9. For large K, however, this initialization produces different solutions, which do not cross. Instead, these phase boundaries exhibit discontinuous change in both Δn and $\bar{n}$, and widen markedly at high K. All of these features are consistent with results of two-site MF theory, but they set in at higher K. For the range of ϵ' we have studied, the onset of first-order transitions occurs near $K = 6$, as opposed to the two-site result of $K \approx 10/3$. As per the data of Sec. 5.1.2, first-order transitions are observed in simulation between $K = 6$ and $K = 7$, demonstrating that Bethe-Peierls does indeed more accurately estimate the location of discontinuous transitions in this model.

The minimum value of K at which ordering occurs is also shifted upwards in BP theory, to about $K = 2.4$. This prediction compares more favorably with the critical value $K \approx 2.7$ found in simulations than does the two-site prediction $K \approx 2$.

Again, viewed on the same scale as results in the main text, the BP data very strongly resemble the results of two-site mean field theory; see Figs. 5.8 to 5.9. Note that these two figures are essentially identical as the discontinuous transitions begin at $K \approx 6$.

5.1.5 Two-cluster Bethe-Peierls approximation

As mentioned in the main text, another way to account for alternating couplings in a lattice model using BP is to use two clusters instead of one (see Fig. 5.10). One cluster corresponds to a sparsely populated stripe, and the other a densely populated stripe. To start, we write the cluster Hamiltonian for cluster A:

$$\begin{aligned} H_A = & -\mu n_{0A} - \mu_B n_{0B} - J n_{0A}(n_{1A} + n_{2A} + n_{3A} + n_{4A}) \\ & - \mu_A(n_{1A} + n_{2A} + n_{3A} + n_{4A} + n_{0A'}) \\ & + \epsilon^{'} n_{0A} n_{0B} - \epsilon n_{0A} n_{0A'} \end{aligned} \tag{5.20}$$

The cluster Hamiltonian for the B lattice can be obtained similarly. The average densities arise in the traditional way, via derivatives of the partition

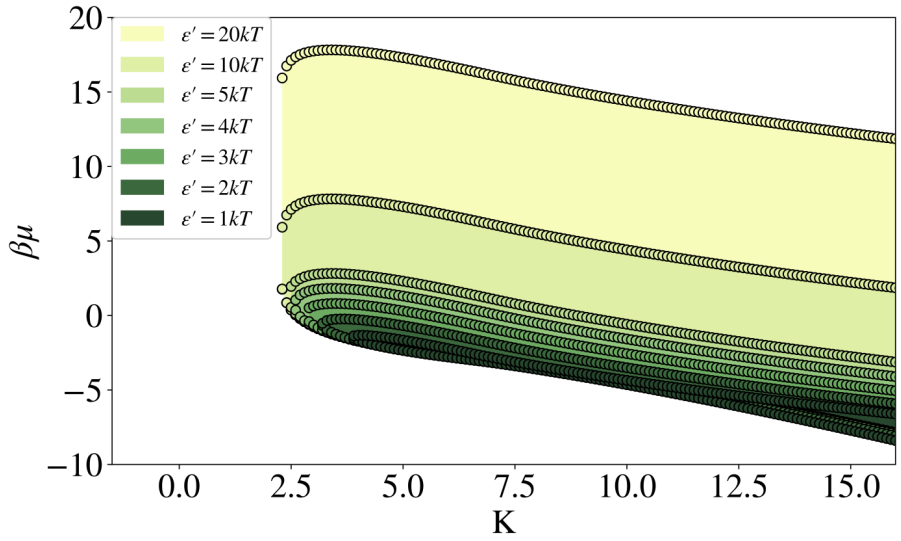

Figure 5.6: BP $\beta\mu$ vs. K phase diagram, with first-order transitions beginning $K \approx 6$. Shaded region indicates the striped phase. The upper branch was calculated via the inversion symmetry relation Eq. (2.4) in the main text.

function:

$$\begin{aligned}\langle n_{0A}\rangle \quad &= \frac{\partial \ln Z_A}{\partial \beta\mu} = \frac{1}{Z_A} e^{\beta\mu}\left(1+e^{\beta(\bar{\mu}+\Delta\mu+J)}\right)^4 \\ &\times\left(1+e^{\beta(\bar{\mu}-\Delta\mu-\epsilon')}\right)\left(1+e^{\beta(\bar{\mu}+\Delta\mu+\epsilon)}\right) \end{aligned} \tag{5.21}$$

$$\begin{aligned}\langle n_A\rangle \quad &= \frac{1}{5}\frac{\partial \ln Z_A}{\partial \beta\mu_A} \\ &= \frac{1}{5Z_A}\Bigg[5\left(1+e^{\beta(\bar{\mu}+\Delta\mu)}\right)^4 e^{\beta(\bar{\mu}+\Delta\mu)}\left(1+e^{\beta(\bar{\mu}-\Delta\mu)}\right) \\ &+4\left(1+e^{\beta(\bar{\mu}+\Delta\mu+J)}\right)^3 e^{\beta(\bar{\mu}+\Delta\mu+J)} e^{\beta\mu}\left(1+e^{\beta(\bar{\mu}-\Delta\mu-\epsilon')}\right)\left(1+e^{\beta(\bar{\mu}+\Delta\mu+\epsilon)}\right) \\ &+e^{\beta\mu}e^{\beta(\bar{\mu}+\Delta\mu+\epsilon)}\left(1+e^{\beta(\bar{\mu}-\Delta\mu-\epsilon')}\right)\left(1+e^{\beta(\bar{\mu}+\Delta\mu+J)}\right)^4\Bigg] \end{aligned} \tag{5.22}$$

Using these expressions, the same systems of equations (5.18) or (5.19)

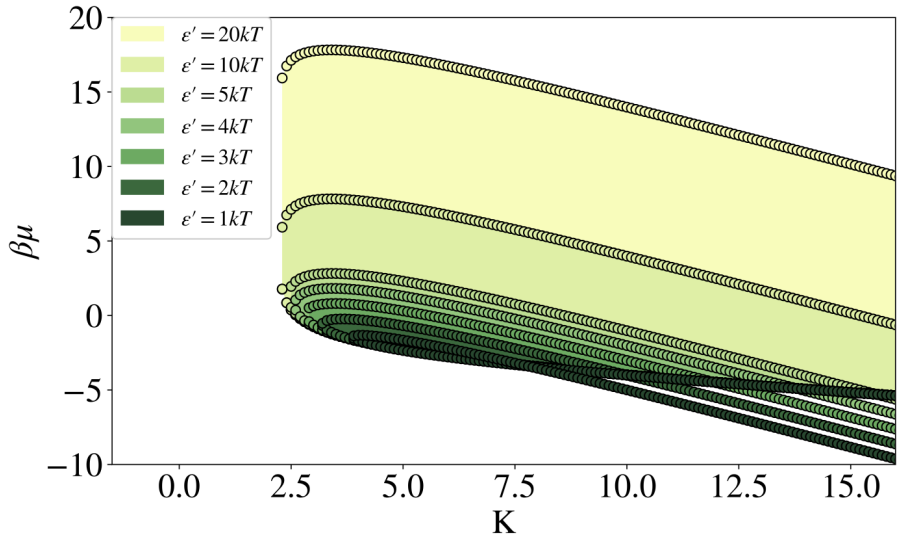

Figure 5.7: BP $\beta\mu$ vs. K phase diagram, continuous transitions throughout. Shaded region indicates the striped phase. The upper branch was calculated via the inversion symmetry relation Eq. (2.4) in the main text.

were solved via gradient descent optimization to find continuous transitions. Please note that no first-order transitions were found for this model, and nor did these equations preserve occupation inversion symmetry.

Momentum-boosted gradient descent

The system of equations, Eq. (5.18), was rephrased as a root-finding problem in Eq. (5.19), such that a gradient descent method could be used to find its roots. Consequently, one can imagine the system of equations as a vector whose components are the equations. Thus, the objective function optimized was the magnitude of this vector – namely, the sum of the squared equations set equal to zero.

A gradient descent approach was used for a number of reasons. Firstly, the ideal initial conditions for this system were unknown, so a method that can handle initial conditions far from the solution was desired; many root-finding and optimization algorithms do not do well when seeded far from the solution. Second, so as to handle potentially multiple solutions for a given set of parameters, we wanted a method that had the ability to find multiple

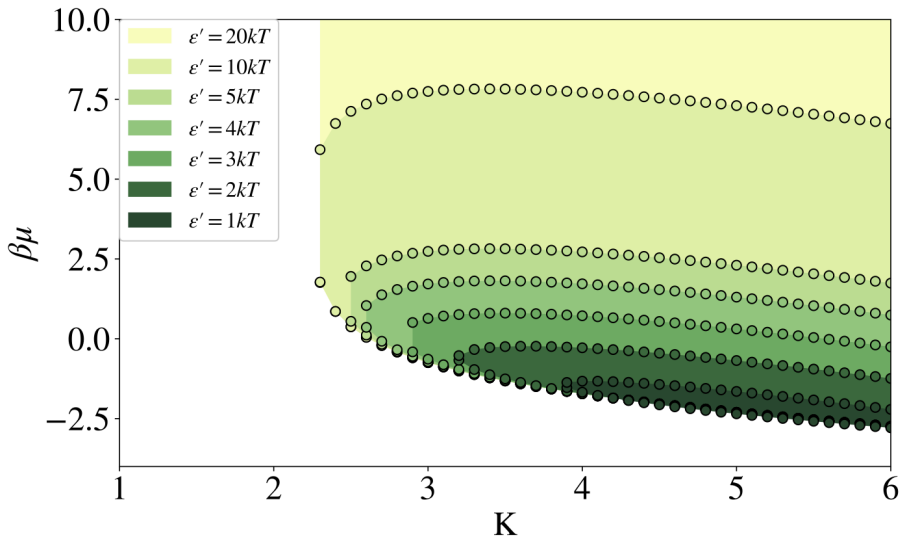

Figure 5.8: BP $\beta\mu$ vs. K phase diagram, with first-order transitions beginning $K \approx 6$ (not visible here). Shaded region indicates the striped phase. The upper branch was calculated via Eq. (2.4) in the main text.

minima – this concern is related to the first, since initial conditions must be given differently so as to explore possible multiple global solutions. Gradient descent is algorithmically simple and has mostly guaranteed convergence, hence it was chosen.

Furthermore, MGD was utilized instead of plain steepest descent as a means of increasing efficiency and preventing traps in local optima. [81] One can write the x component of the update vector at the next step as

$$\begin{aligned} v_{x,t+1} &= \gamma v_{x,t} + s\nabla_x f \\ x &= x - v_{x,t+1} \end{aligned} \tag{5.23}$$

where γ is the momentum scalar that usually is between 0.9 and 1 and encodes the "memory" of the previous step, and s is the step size for the descent. The step size is on the order of 0.1 to 0.0001 usually. Convergence was determined by how close both the objective function and the gradient were to zero. The gradient of Eq. (5.19) was approximated using finite differences.

For each system of BP equations, the initial conditions were generated by

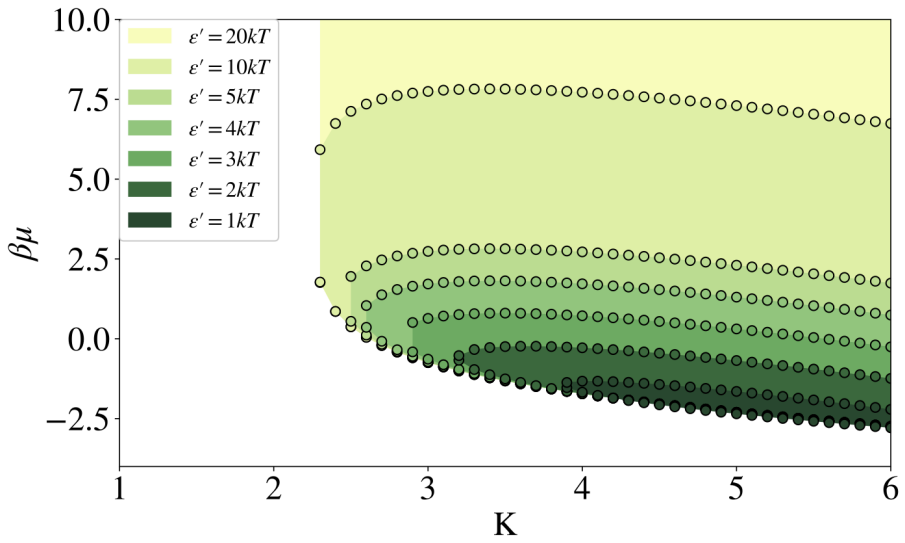

Figure 5.9: BP $\beta\mu$ vs. K phase diagram, continuous transitions throughout. Shaded region indicates the striped phase. The upper branch was calculated via Eq. (2.4) in the main text.

creating a grid of ($\Delta\mu$, $\bar{\mu}$) values. Since $\bar{\mu}$ was expected to remain relatively close to μ, a limited number of $\bar{\mu}$ initial guesses were used. For $\Delta\mu$, a grid ranging from -2 to 2 k_BT measured out by a given increment were used; based on preliminary explorations, solutions obeying the constraints of the problem are only found for relatively small $\Delta\mu$ (that is, $\Delta\mu$ within these bounds).

5.2 Chapter 3 Appendix

5.2.1 Enhanced Monte Carlo sampling specifications

The enhanced sampling methods used to obtain data in Figs. 3.10 to 3.12 in Chapter 3 utilized the flat histogram method. [80] Simulations were performed by PLG.

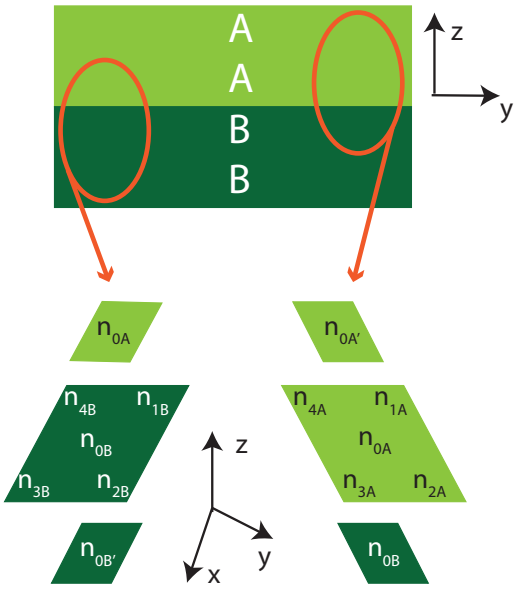

Figure 5.10: Two-cluster schematic. The top bar represents four layers, with two sets of two-layer stripes. The lower half of the diagram represents the clusters used in the BP approximation, with n_{0x} as the centers of the clusters.

5.2.2 Solving mean field theory self-consistent equations

$$\begin{aligned} \Delta n &= p_{00} a e^{K\bar{n}} \sinh(K\Delta n) \\ \bar{n} &= p_{00} a e^{K\bar{n}} \left[\cosh(K\Delta n) + \delta a e^{K\bar{n}} e^{\gamma\bar{\omega}} \right] \\ \bar{\omega} &= p_{00} \delta a^2 e^{2K\bar{n}} e^{\gamma\bar{\omega}} \end{aligned} \tag{5.24}$$

$$\begin{aligned} n_1 &= p_{00}(a e^{Kn_1} + \delta a^2 e^{K(n_1+n_2)} e^{\gamma\bar{\omega}}) \\ n_2 &= p_{00}(a e^{Kn_2} + \delta a^2 e^{K(n_1+n_2)} e^{\gamma\bar{\omega}}) \\ \bar{\omega} &= p_{00} \delta a^2 e^{K(n_1+n_2)} e^{\gamma\bar{\omega}} \end{aligned} \tag{5.25}$$

In order to find transition points in either mean field method, one needs to solve systems of self-consistent equations. The system corresponds to

Eqs. (5.24), written for both layers, or for Eqs. (5.25). We chose the latter option, as it was more numerically stable. The system was initialized for five different (n_1, n_2) pairs – (0.6, 0.4), (0.1, 0.1), (0.9, 0.9), (0.9, 0.1), and (0.2, 0.1), so as to cover a range of density values, as well as capture n values related by inversion symmetry. Initial $\bar{\omega}$ values ranged were 0, 0.01, 0.5, or 1, and each of these values was used with each (n_1, n_2) initial condition. The tolerance for self-consistency was 10^{-12}, and the maximum number of iterations was 1 million. After selecting the converged, minimum free energy solutions for $(K, \beta\mu)$ each point. Δn transitions were determined by finding Δn differences larger than 10^{-8} between consecutive $\beta\mu$ values for a given K. $\bar{\omega}$ transitions were discovered either by identifying $\bar{\omega}$ differences greater than 0.01 or discontinuities in finite differences of $\bar{\omega}$ as a function of $\beta\mu$.

Bibliography

[1] M. Leuenberger, J. M. Morris, A. M. Chan, L. Leonelli, K. K. Niyogi, and G. R. Fleming, "Dissecting and modeling zeaxanthin- and lutein-dependent nonphotochemical quenching in *Arabidopsis thaliana*," *Proc. Nat. Acad. Sci.*, vol. 114, no. 33, pp. 7009–7017, 2017.

[2] J. M. Morris and G. R. Fleming, "Quantitative modeling of energy dissipation in *Arabidopsis thaliana*," *Environ. Exper. Bot.*, vol. 154, pp. 99–109, 2018.

[3] K. Głowacka, J. Kromdijk, K. Kucera, J. Xie, A. P. Cavanagh, L. Leonelli, A. D. B. Leakey, D. R. Ort, K. K. Niyogi, and S. P. Long, "Photosystem II subunit S overexpression increases the efficiency of water use in a field-grown crop," *Nature Comm.*, vol. 9, p. 868, 2018.

[4] R. Noriega, D. T. Finley, J. Haberstroh, P. L. Geissler, M. B. Francis, and N. S. Ginsberg, "Manipulating excited-state dynamics of individual light-harvesting chromophores through restricted motions in a hydrated nanoscale protein cavity," *J. Phys. Chem. B*, vol. 119, pp. 6963–6973, 2015.

[5] M. Delor, J. Dai, T. D. Roberts, J. R. Rogers, S. M. Hamed, J. B. Neaton, P. L. Geissler, M. B. Francis, and N. S. Ginsberg, "Exploiting chromophore-protein interactions through linker engineering to tune photoinduced dynamics in a biomimetic light-harvesting platform," *J. Am. Chem. Soc.*, vol. 140, no. 20, pp. 6278–6287, 2018.

[6] J. P. Dekker and E. J. Boekema, "Supramolecular organization of thylakoid membrane proteins in green plants," *Biochim. Biophys. Acta*, vol. 1706, no. 1-2, pp. 12–39, 2005.

[7] R. Nevo, D. Charuvi, O. Tsabari, and Z. Reich, "Composition, architecture, and dynamics of the photosynthetic apparatus in higher plants," *Plant J.*, vol. 70, no. 1, pp. 157–176, 2012.

[8] A. R. Schneider and P. L. Geissler, "Coexistence of fluid and crystalline phases of proteins in photosynthetic membranes," *Biophys. J*, vol. 105, pp. 1161–1170, 2013.

[9] A. R. Schneider and P. L. Geissler, "Coarse-grained computer simulation of dynamics in thylakoid membranes: methods and opportunities," *Front. Plant Sci.*, vol. 4, 2014.

[10] C. Lee, C. Pao, and B. Smit, "PSII-LHCII supercomplex organizations in photosynthetic membrane by coarse-grained simulation," *J. Phys. Chem. B*, vol. 119, no. 10, pp. 3999–4008, 2015.

[11] K. Amarnath, D. I. G. Bennett, A. R. Schneider, and G. R. Fleming, "Multiscale model of light harvesting by photosystem II in plants," *Proc. Nat. Acad. Sci.*, vol. 113, no. 5, pp. 1156–1161, 2016.

[12] A. Capretti, A. K. Ringsmuth, J. F. van Velzen, A. Rosnik, R. Croce, and T. Gregorkiewicz, "Nanophotonics of higher-plant photosynthetic membranes," *Light: Sci. Appl.*, vol. 8, no. 5, 2019.

[13] H. Kirchhoff, "Chloroplast ultrastructure in plants," *New Phytol.*, vol. 223, pp. 56–574, 2019.

[14] A. M. Rosnik and P. L. Geissler, "Lattice models for protein organization throughout thylakoid membrane stacks," *arXiv*, no. 1907.04977, 2019.

[15] M. Pribil, M. Labs, and D. Leister, "Structure and dynamics of thylakoids in land plants," *J. Exp. Bot.*, vol. 65, no. 8, pp. 1955–1972, 2014.

[16] X. Qin, M. Suga, T. Kuang, and J. Shen, "Structural basis for energy transfer pathways in the plant PSI-LHCI supercomplex," *Science*, vol. 348, no. 6238, pp. 989–995, 2015.

[17] X. Wei, X. Su, P. Cao, X. Liu, W. Chang, M. Li, X. Zhang, and Z. Liu, "Structure of spinach photosystem II-LHCII supercomplex at 3.2 Å resolution," *Nature*, vol. 534, pp. 69–74, 2016.

[18] N. Liguori, X. Periole, S. J. Marrink, and R. Croce, "From light-harvesting to photoprotection: structural basis of the dynamic switch of the major antenna complex of plants (LHCII)," *Sci. Rep.*, vol. 5, 2015.

[19] L. Nosek, D. Semchonok, E. J. Boekema, P. Ilík, and R. Kouřil, "Structural variability of plant photosystem II megacomplexes in thylakoid membranes," *Plant J.*, vol. 89, pp. 104–111, 2017.

[20] W. S. Chow, E. Kim, P. Horton, and J. M. Anderson, "Granal stacking of thylakoid membranes in higher plant chloroplasts: the physicochemical forces at work and the functional consequences that ensue," *Photochem. Photobiol. Sci.*, vol. 4, pp. 1081–1090, 2005.

[21] H. Kirchhoff, W. Haase, S. Haferkamp, T. Schott, M. Borinski, U. Kubitscheck, and M. Rögner, "Structural and functional self-organization of photosystem II in grana thylakoids," *Biochim. Biophys. Acta*, vol. 1767, pp. 1180–1188, 2007.

[22] J. Standfuss, A. C. Terwisscha van Scheltinga, M. Lamborghini, and W. Kuhlbrandt, "Mechanisms of photoprotection and nonphotochemical quenching in pea light-harvesting complex at 2.5 Å resolution," *EMBO J.*, vol. 24, no. 5, pp. 919–928, 2005.

[23] W. Phuthong, Z. Huang, T. M. Wittkopp, K. Sznee, M. L. Heinnickel, J. P. Dekker, R. N. Frese, F. B. Prinz, and A. R. Grossman, "The use of contact mode atomic force microscopy in aqueous medium for structural analysis of spinach photosynthetic complexes," *Plant Physiol.*, vol. 169, pp. 1318–1332, 2015.

[24] B. Onoa, A. R. Schneider, M. D. Brooks, P. Grob, E. Nogales, P. L. Geissler, K. K. Niyogi, and C. Bustamante, "Atomic force microscopy of photosystem II and its unit cell clustering quantitatively delineate the mesoscale variability in *Arabidopsis* thylakoids," *PLOS ONE*, vol. 9, no. 7, 2014.

[25] A. V. Ruban and M. P. Johnson, "Visualizing the dynamic structure of the plant photosynthetic membrane," *Nat. Plants*, vol. 1, 2015.

[26] E. Erickson, S. Wakao, and K. K. Niyogi, "Light stress and photoprotection in *Chlamydomonas reinhardtii*," *Plant J.*, vol. 82, pp. 449–465, 2015.

[27] H. Kirchhoff, C. Halla, M. Wood, M. Herbstová, O. Tsabari, R. Nevo, D. Charuvi, E. Shimonic, and Z. Reich, "Dynamic control of protein diffusion within the granal thylakoid lumen," *Proc. Nat. Acad. Sci.*, vol. 108, no. 50, pp. 20248–20253, 2011.

[28] H. Kirchhoff, "Diffusion of molecules and macromolecules in thylakoid membranes," *Biochim. Biophys. Acta, Bioenerg.*, vol. 1837, no. 4, pp. 495–502, 2014.

[29] P.-r. Albertsson, "Interaction between the lumenal sides of the thylakoid membrane," *FEBS Lett.*, vol. 149, no. 2, pp. 186–190, 1982.

[30] S. Puthiyaveetil, B. van Oort, and H. Kirchhoff, "Surface charge dynamics in photosynthetic membranes and the structural consequences," *Nat. Plants*, vol. 3, p. 17020, 2017.

[31] L. Tayebi, Y. Ma, D. Vashaee, G. Chen, S. K. Sinha, and A. N. Parikh, "Long-range interlayer alignment of intralayer domains in stacked lipid bilayers," *Nat. Mat.*, vol. 11, pp. 1074–1080, 2012.

[32] L. Tayebi, A. N. Parikh, and D. Vashaee, "Long-range interlayer alignment of intralayer domains in stacked lipid bilayers," *Int. J. Mol. Sci.*, vol. 14, pp. 3824–3833, 2013.

[33] R. S. Ellis, P. T. Otto, and H. Touchette, "Analysis of phase transitions in the mean-field Blume-Emery-Griffiths model," *Ann. Appl. Probab.*, vol. 15, no. 3, pp. 2203–2254, 2005.

[34] M. Deserno, "Tricriticality and the Blume-Capel model: A Monte Carlo study within the microcanonical ensemble," *Phys. Rev. E*, vol. 56, no. 5, pp. 5204–5210, 1997.

[35] H. Ez-Zahraouy and A. Kassou-Ou-Ali, "Phase diagrams of the spin-1 Blume-Capel film with an alternating crystal field," *Phys. Rev. B*, vol. 69, 2004.

[36] M. E. Fisher and W. Selke, "Infinitely many commensurate phases in a simple Ising model," *Phys. Rev. Lett.*, vol. 44, no. 23, pp. 1502–1505, 1980.

[37] F. Y. Wu, "The Potts model," *Rev. Mod. Phys.*, vol. 54, no. 2, pp. 235–267, 1982.

[38] T. Speck, E. Reister, and U. Seifert, "Specific adhesion of membranes: Mapping to an effective bond lattice gas," *Phys. Rev. E*, vol. 82, no. 3, p. 021923, 2010.

[39] B. B. Machta, S. L. Veatch, and J. P. Sethna, "Critical Casimir forces in cellular membranes," *Phys. Rev. Lett.*, vol. 109, no. 13, pp. 1–5, 2012.

[40] Y. S. Jho, R. Brewster, S. A. Safran, and P. A. Pincus, "Long-range interaction between heterogeneously charged membranes," *Langmuir*, vol. 27, no. 8, pp. 4439–4446, 2011.

[41] B. West, F. L. H. Brown, and F. Schmid, "Membrane-protein interactions in a generic coarse-grained model for lipid bilayers," *Biophys. J.*, vol. 96, no. 1, pp. 101–115, 2009.

[42] A. Naji and F. L. H. Brown, "Membrane-protein interactions in a generic coarse- grained model for lipid bilayers," *J. Chem. Phys.*, vol. 126, p. 235103, 2007.

[43] N. Meilhac and N. Destainville, "Clusters of proteins in biomembranes: Insights into the roles of interaction potential shapes and of protein diversity," *J. Phys. Chem. B*, vol. 115, no. 22, pp. 7190–7199, 2011.

[44] A. Pasqua, L. Maibaum, G. Oster, D. A. Fletcher, and P. L. Geissler, "Large-scale simulations of fluctuating biological membranes," *J. Chem. Phys.*, vol. 132, no. 15, pp. 1–6, 2010.

[45] J. C. Stachowiak, E. M. Schmid, C. J. Ryan, H. S. Ann, D. Y. Sasaki, M. B. Sherman, P. L. Geissler, D. A. Fletcher, and C. C. Hayden, "Membrane bending by protein-protein crowding," *Nat. Cell Biol.*, vol. 14, no. 9, pp. 944–949, 2012.

[46] E. M. Schmid, M. H. Bakalar, C. Kaushik, J. Weichsel, H. S. Ann, P. L. Geissler, M. L. Dustin, and D. A. Fletcher, "Size-dependent protein segregation at membrane interfaces," *Nat. Phys.*, vol. 12, pp. 704–711, 2016.

[47] M. Schick, "Membrane heterogeneity: Manifestation of a curvature-induced microemulsion," *Phys. Rev. E*, vol. 85, no. 3, p. 031902, 2012.

[48] G. Garbès Putzel and M. Schick, "Phase behavior of a model bilayer membrane with coupled leaves," *Biophys. J.*, vol. 94, no. 3, pp. 869–877, 2012.

[49] T. Hoshino, S. Komura, and D. Andelman, "Correlated lateral phase separations in stacks of lipid membranes," *J. Chem. Phys.*, vol. 143, no. 50, p. 243124, 2015.

[50] T. Hoshino, S. Komura, and D. Andelman, "Permeation through a lamellar stack of lipid mixtures," *EPL*, vol. 120, 2017.

[51] G. Fair, "Bethe-Peierls-Weiss approximation and a model for ferromagnetic thin films," Tech. Rep. D-2979, National Aeronautics and Space Administration, Cleveland, Ohio, September 1965.

[52] M. A. Neto, R. A. dos Anjos, and J. R. de Sousa, "Anisotropic Ising model in a magnetic field: Effective-field theory analysis," *Phys. Rev. E*, vol. 73, 2006.

[53] A. R. Schneider, *Pattern formation in photosynthetic membranes: a physical and statistical approach*. PhD thesis, University of California-Berkeley, 2013.

[54] S. Puthiyaveetil, O. Tsabari, T. Lowry, S. Lenhert, R. R. Lewis, Z. Reich, and H. Kirchhoff, "Compartmentalization of the protein repair machinery in photosynthetic membranes," *Proc. Nat. Acad. Sci.*, vol. 111, no. 44, pp. 15839–15844, 2014.

[55] H. Kirchhoff, R. M. Sharpe, M. Herbstová, R. Yarbrough, and G. E. Edwards, "Differential mobility of pigment-protein complexes in granal and agranal thylakoid membranes of C3 and C4 plants," *Plant Physiol.*, vol. 161, no. 1, pp. 497–507, 2012.

[56] C. H. Clausen, M. D. Brooks, T. Li, P. Grob, G. Kemalyan, E. Nogales, K. K. Niyogi, and D. A. Fletcher, "Dynamic mechanical responses of *Arabidopsis* thylakoid membranes during PSII-specific illumination," *Biophys. J.*, vol. 106, no. 9, pp. 1864–1870, 2014.

[57] M. Iwai, C. Pack, Y. Takenaka, Y. Sako, and A. Nakano, "Photosystem II antenna phosphorylation-dependent protein diffusion determined by fluorescence correlation spectroscopy," *Sci. Rep.*, vol. 3, no. 2833, pp. 1–7, 2013.

[58] M. Herbstová, S. Tietz, C. Kinzel, M. V. Turkina, and H. Kirchhoff, "Architectural switch in plant photosynthetic membranes induced by light stress," *Proc. Nat. Acad. Sci.*, vol. 109, no. 49, pp. 20130–20135, 2012.

[59] H. Koochak, S. Puthiyaveetil, D. L. Mullendore, M. Li, and H. Kirchhoff, "The structural and functional domains of plant thylakoid membranes," *Plant J.*, vol. 97, pp. 412–429, 2019.

[60] J. Minagawa, "State transitions: the molecular remodeling of photosynthetic supercomplexes that controls energy flow in the chloroplast," *Biochim. Biophys. Acta, Bioenerg.*, vol. 1807, no. 8, pp. 897–905, 2011.

[61] S. Lemeille and J. Rochaix, "State transitions at the crossroad of thylakoid signalling pathways," *Photosynth. Res.*, vol. 106, no. 1–2, pp. 33–46, 2010.

[62] L. M. Wlodarczyk, E. Dinc, R. Croce, and J. P. Dekker, "Excitation energy transfer in *Chlamydomonas reinhardtii* deficient in the PSI core or the PSII core under conditions mimicking state transitions," *Biochim. Biophys. Acta, Bioenerg.*, vol. 1857, no. 6, pp. 625–633, 2016.

[63] A. Crepin and S. Caffarri, "The specific localizations of phosphorylated Lhcb1 and Lhcb2 isoforms reveal the role of Lhcb2 in the formation of the PSI-LHCII supercomplex in *Arabidopsis* during state transitions," *Biochim. Biophys. Acta*, vol. 1847, no. 12, pp. 1539–1548, 2015.

[64] W. J. Nawrocki, S. Santabarbara, L. Mosebach, F. Wollman, and F. Rappaport, "State transitions redistribute rather than dissipate energy between the two photosystems in *Chlamydomonas*," *Nat. Plants*, vol. 2, p. 16031, 2016.

[65] Y. Shan and H. Wang, "The structure and function of cell membranes examined by atomic force microscopy and single-molecule force spectroscopy," *Chem. Soc. Rev.*, vol. 44, p. 3617, 2015.

[66] S. Tietz, S. Sujith Puthiyaveetil, H. M. Enlow, R. Yarbrough, M. Wood, D. A. Semchonok, T. Lowry, Z. Li, P. Jahns, E. J. Boekema, S. Lenhert, K. K. Niyogi, and H. Kirchhoff, "Functional implications of photosystem II crystal formation in photosynthetic membranes," *J. Biol. Chem.*, vol. 290, no. 22, pp. 14091–14106, 2015.

[67] J. Hubbard, "Calculation of partition functions," *Phys. Rev. Lett.*, vol. 3, p. 77, 1959.

[68] R. L. Stratonovich, "A method for the computation of quantum distribution functions," *Dokl. Akad. Nauk SSSR*, vol. 115, no. 6, pp. 1097–1100, 1957.

[69] M. Iwai, M. Yokono, and A. Nakano, "Visualizing structural dynamics of thylakoid membranes," *Sci. Rep.*, vol. 4, p. 3768, 2014.

[70] M. Iwai, M. Yokono, K. Kurokawa, A. Ichihara, and A. Nakano, "Live-cell visualization of excitation energy dynamics in chloroplast thylakoid structures," *Sci. Rep.*, vol. 6, p. 29940, 2016.

[71] M. Iwai, M. S. Roth, and K. K. Niyogi, "Subdiffraction-resolution live-cell imaging for visualizing thylakoid membranes," *Plant J.*, vol. 96, no. 1, pp. 233–243, 2019.

[72] T. G. Laughlin, A. N. Bayne, J. Trempe, D. F. Savage, and K. M. Davies, "Structure of the complex I-like molecule NDH of oxygenic photosynthesis," *Nat. Lett.*, vol. 566, p. 411, 2019.

[73] E. Shimoni, O. Rav-Hon, I. Ohad, V. Brumfeld, and Z. Reich, "Three-dimensional organization of higher-plant chloroplast thylakoid membranes revealed by electron tomography," *Plant Cell*, vol. 17, pp. 2580–2586, 2005.

[74] W. I. Gruszecki and K. Strzałka, "Carotenoids as modulators of lipid membrane physical properties," *Biochim. Biophys. Acta*, vol. 1740, pp. 108–115, 2005.

[75] T. N. Tóth, V. Chukhutsina, I. Domonkos, J. Knoppová, J. Komenda, M. Kis, Z. Lénárt, G. Garab, L. Kovács, Z. Gombos, and H. van Amerongen, "Carotenoids are essential for the assembly of cyanobacterial photosynthetic complexes," *Biochim. Biophys. Acta*, vol. 1847, pp. 1153–1165, 2015.

[76] S. Kumar, D. Bouzida, R. H. Swendsen, P. A. Kollman, and J. M. Rosenberg, "The weighted histogram analysis method for free-energy calculations on biomolecules. I. the method," *J. Comp. Chem.*, vol. 13, no. 8, pp. 1011–1021, 1992.

[77] K. Binder, "Critical properties from Monte Carlo coarse graining and renormalization," *Phys. Rev. Lett.*, vol. 47, p. 693, 1981.

[78] K. Binder, "Finite size scaling analysis of Ising model block distribution functions," *Z. Phys. B*, vol. 43, no. 2, pp. 119–140, 1981.

[79] A. M. Ferrenberg, J. Xu, and D. P. Landau, "Pushing the limits of Monte Carlo simulations for the 3d Ising model," *Phys. Rev. E*, vol. 97, p. 043301, 2018.

[80] J. Wang, "Flat histogram Monte Carlo method," *Physica A*, vol. 281, pp. 147–150, 2000.

[81] S. Ruder, "An overview of gradient descent optimization algorithms," *arXiv*, no. 1609.04747v2, 2017.

[82] G. Garab, "Hierarchical organization and structural flexibility of thylakoid membranes," *Biochim. Biophys. Acta*, vol. 1837, no. 4, pp. 481–494, 2014.

[83] A. P. Vieira, J. X. de Carvalho, and S. R. Salinas, "Phase diagram of a random-anisotropy mixed-spin Ising model," *Phys. Rev. B*, vol. 63, no. 18, 2001.

[84] U. Armbruster, M. Labs, M. Pribil, S. Viola, W. Xu, M. Scharfenberg, A. Hertle, U. Rojahn, P. Jensen, F. Rappaport, P. Joliot, P. Dörmann, G. Wanner, and D. Leistera, "*Arabidopsis* CURVATURE THYLAKOID1 proteins modify thylakoid architecture by inducing membrane curvature," *Plant Cell*, vol. 25, no. 7, pp. 2661–2678, 2013.

[85] W. Helfrich, "Elastic properties of lipid bilayers: theory and possible experiments," *Z. Naturforsch. C*, vol. 28, no. 11, pp. 693–703, 1973.